Calibration and Commissioning of the Helium And Lead Observatory

by

Colin Bruulsema

Thesis submitted in partial fulfillment
of the requirements for the degree of
Master of Science (MSc) in Physics

The Faculty of Graduate Studies
Laurentian University
Sudbury, Ontario, Canada

THESIS DEFENCE COMMITTEE/COMITÉ DE SOUTENANCE DE THÈSE
Laurentian Université/Université Laurentienne
Faculty of Graduate Studies/Faculté des études supérieures

Title of Thesis Titre de la thèse	Calibration and Commissioning of the Helium And Lead Observatory
Name of Candidate Nom du candidat	Bruulsema, Colin James
Degree Diplôme	Master of Science
Department/Program Département/Programme	Physics
Date of Defence Date de la soutenance	January 25, 2017

APPROVED/APPROUVÉ

Thesis Examiners/Examinateurs de thèse:

Dr. Clarence Virtue
(Supervisor/Directeur(trice) de thèse)

Dr. Christine Kraus
(Committee member/Membre du comité)

Dr. Chris Jillings
(Committee member/Membre du comité)

Dr. David Hanna
(External Examiner/Examinateur externe)

Approved for the Faculty of Graduate Studies
Approuvé pour la Faculté des études supérieures
Dr. David Lesbarrères
Monsieur David Lesbarrères
Dean, Faculty of Graduate Studies
Doyen intérimaire, Faculté des études supérieures

ACCESSIBILITY CLAUSE AND PERMISSION TO USE

Abstract

The Helium And Lead Observatory (HALO) is a dedicated supernova detector at SNOLAB consisting of 79 tonnes of lead instrumented with 128 ^{3}He-filled neutron counters. A burst of neutrinos from a supernova will interact with the lead and result in a burst of neutrons, detectable by the counters. This burst can be identified as a supernova signal.

The previously existing HALO Monte Carlo simulation was revised to better represent the detector and evaluate its supernova response. The composition of the paint used on the lead blocks was estimated using new and previous measurements. Other geometry updates were checked with neutron capture simulations to verify their implementation.

To verify the detection efficiencies of the Monte Carlo simulation, a ^{252}Cf neutron source was deployed in the 40 copper calibration tubes in the detector. The high neutron multiplicity in Cf fissions allowed for the source strength to be determined along with the neutron capture efficiency by an analysis of the relative population of the detected multiplicities. This verified the Monte Carlo simulation's results and gave an overall efficiency for the detection of supernova-induced neutrons of $(27.61 \pm 0.17)\%$.

Backgrounds to the detection of supernovae include neutrons leaking into the detector from the lab, the spontaneous fission of uranium inside the detector, and muon-induced spallation events in and around the detector. These factors along with the false positive rates specified by the Supernova Early Warning System (SNEWS) limit the trigger threshold to 4 neutrons detected in two seconds, giving a detection range of about 13.7 kpc for supernovae with an average neutrino energy of 18 MeV and a pinching parameter of 2.

Acknowledgements

Throughout my MSc at Laurentian University, I have received help and advice from many talented people both at Laurentian and SNOLAB. I would like to thank them for their influence and help.

First of all, I would like to thank my supervisor Clarence Virtue for his help and advice over the course of my time at Laurentian. He was always available for discussion and guidance about my projects and other physics topics.

I am grateful for the input given by my committee members Christine Kraus and Chris Jillings about my studies, and for their helpful questions about my research.

I would also like to thank the HALO Collaboration for their help and support. Micheal Schumaker's introduction and advice on the Monte Carlo simulation was essential for the success of the calibration, as was Stan Yen's help with the source encapsulation and his advice and mentorship in experimental physics. I would also like to thank Mark Howe for his help working with ORCA to set up the burst monitor, as well as Alec Habig and Kate Scholberg who gave assistance with the testing of the SNEWS alarm system, and Danielle Riggin, Justin Muller and Stephane Venne who gave me advice pertaining to simulation, data processing, timing and detector performance.

Contents

List of Figures

List of Tables

Chapter 1

Supernovae

1.1 Supernova Explosions

The atomic matter of the universe was originally composed entirely of the lighter elements of H, He, and Li. All heavier elements were formed by nuclear fusion in the hot and high pressure environment inside of stars. These elements escape into space mostly through the death of very massive stars in violent supernova explosions. These explosions have luminosities comparable to entire galaxies, and seem to be associated with the powerful gamma ray bursts seen throughout the universe [1].

Supernova explosions occur in large stars when the heat from fusion can no longer sustain the structure of the star under gravity. The inability of electrons to occupy the same state then provides the pressure to maintain the star's shape. This effect is known as electron degeneracy pressure and can be shown to be insufficient for high mass configurations. The highest mass that can be held by electron degeneracy pressure is known as the Chandrasekhar Limit.

1.1.1 Chandrasekhar Limit

The mass limit that triggers a supernova explosion can be determined by the static equations of a spherically symmetric star. Pressure in the star caused by degenerate electrons can be calculated with the momentum flux:

$$P \propto \int_0^{p_f} pvn(p)\, dp \tag{1.1}$$

Where $n(p)$ is the number of momentum states at momentum p, and p_f is the Fermi momentum. $n(p)$ is proportional to the area of a sphere in momentum space [2] up to the Fermi momentum, giving $n(p) \propto p^2$ and $p_f \propto \rho^{\frac{1}{3}}$, where ρ is the electron density of the star.

For relativistic electrons, $pv \approx pc$, and for non-relativistic electrons $pv \approx \frac{p^2}{m}$. The above integral then evaluates to

$$P_{\frac{v}{c}\to 1} \propto \int_0^{p_f} p^3\, dp \propto {p_f}^4 \propto \rho^{\frac{4}{3}} \tag{1.2}$$

$$P_{\frac{v}{c}\to 0} \propto \int_0^{p_f} p^4\, dp \propto {p_f}^5 \propto \rho^{\frac{5}{3}} \tag{1.3}$$

The electron degeneracy pressure's relation to density is expressed by an index n, with $P = C_1\rho^{\frac{n+1}{n}}$ with $n = 3$ in the relativistic limit and $n = 3/2$ in the non-relativistic limit [3].

A shell of thickness dr can be found to have a total gravitational force towards its center due to its mass $4\pi r^2\rho dr$ as well as all contained mass $m(r)$. To remain stationary the shell must then have a pressure difference dP which, across the area of the shell, matches the force of gravity. This can be simplified to

$$\frac{G\rho m(r)}{r^2} = -\frac{dP}{dr} \tag{1.4}$$

Using the relativistic or non-relativistic electron degeneracy pressure relation $P = C_1\rho^{\frac{n+1}{n}}$ and the continuity equation $\frac{dm(r)}{dr} = 4\pi r^2\rho$, a differential equation can be found for ρ as a function of r:

$$-4\pi r^2\rho = (n+1)\frac{C_1}{G}\frac{d}{dr}(r^2\frac{d\rho^{\frac{1}{n}}}{dr}) \tag{1.5}$$

It is convenient to make a dimensionless equation using $\rho = \rho_c\chi^n$ and $r = a\zeta$, where ρ_c is the central density, a is the radius of the star. This converts the differential equation to

$$-\chi^n = \frac{1}{\zeta^2}\frac{d}{d\zeta}(\zeta^2\frac{d\chi}{d\zeta}) \tag{1.6}$$

$$a = \rho_c^{\frac{1-n}{2n}} \sqrt{\frac{(n+1)C_1}{4\pi G}} \tag{1.7}$$

This differential equation can be solved with $\chi(0) = 1$ and $\frac{d\chi}{d\zeta}\Big|_{\zeta=0} = 0$ to find a solution $\chi(\zeta)$. ζ_1 is defined with $\chi(\zeta_1) = 0$, so $a\zeta_1$ is the radius of the degenerate star.

The mass of this star can be found using the original differential equation to integrate its density:

$$M = \int_0^{\zeta_1} 4\pi\rho r^2 \, dr = 4\pi\rho_c a^3 \int_0^{\zeta_1} \zeta^2 \chi^n \, d\zeta = -4\pi\rho_c a^3 \int_0^{\zeta_1} \frac{d}{d\zeta}(\zeta^2 \frac{d\chi}{d\zeta}) \, d\zeta \tag{1.8}$$

$$M = -4\pi\rho_c a^3 {\zeta_1}^2 \frac{d\chi}{d\zeta}\Big|_{\zeta=\zeta_1} \propto a^3 \rho_c \tag{1.9}$$

For degenerate non-relativistic particles with $n = \frac{3}{2}$, this gives $a \propto \rho_c^{-\frac{1}{6}}$ and $M \propto \sqrt{\rho_c}$, showing that the volume decreases with added mass. For the relativistic case with $n = 3$, $a \propto \rho_c^{-\frac{1}{3}}$, resulting in no ρ_c dependence for M. This shows that above a certain mass the relativistic degeneracy pressure cannot solve the static equation for a star, suggesting a collapse above a certain mass. This mass has been found to be around 1.4 solar masses, and is known as the Chandrasekhar limit [2].

1.1.2 Types of Supernovae

Supernovae can be classified into thermonuclear or core-collapse supernovae. The Chandrasekhar mass limit applies to stars which are no longer producing their own heat from fusion. This occurs in the carbon and oxygen-rich white dwarf stellar remnants which lack the pressure and temperature to fuse heavier elements, resulting in a thermonuclear supernova, and in the iron cores of very massive stars, causing a core-collapse supernova.

Thermonuclear Supernovae

Thermonuclear supernovae, or Type 1a supernovae as they are classified by their absorption lines, are optically more luminous than core-collapse supernovae, but do not emit a

significant neutrino burst. These supernovae occur when white dwarf stars, mainly composed of hot but inert carbon and oxygen, accumulate matter from nearby objects. When enough matter is accumulated, the start of the star's collapse releases enough energy that carbon and oxygen fusion is suddenly allowed and the star explodes from the energy released in fusion, expelling its matter into space [1].

Although Type 1a supernovae in the Milky Way are less common than core-collapse supernovae by roughly a factor of 10 [1], their predictable luminosity curves make them useful for extragalactic astronomy. Type 1a supernova were used to determine the large scale geometry of the universe by relating redshift to distance as determined by the apparent luminosity of the supernovae.

Core-Collapse Supernovae

Core-collapse supernovae are initiated in an entirely different manner, in the cores of massive stars. If a star's mass exceeds 8 solar masses, it will continue to fuse nuclei all the way up to iron, giving the star an outer shell mainly composed of hydrogen followed by consecutive shells of primarily helium, carbon, neon, oxygen, and silicon [4]. Shortly before the supernova, fusion begins to create an iron core within the silicon core. Because the binding energy per nucleon peaks around iron, nuclear reactions stop, and thus cannot sustain the core temperature at this stage. Instead the core must be held against gravity by electron degeneracy pressure, the eventual failure of which causes the core to suddenly collapse.

Because the nuclei of the core have energies close to the peak binding energy per nucleon, there is no immediate explosion fueled by fusion. Instead the core falls from a sphere with a radius of 3000 km to a radius of around 10 km in about a tenth of a second [4]. At this size the collapsed core reaches nuclear density, causing it to bounce outwards.

The shock wave created by the core bounce is initially traveling with an extremely high speed of around $(3 \text{ to } 6) * 10^7 \ \mathrm{m/s}$ [1]. However, the nuclei of the falling stellar matter that the shock encounters drain this energy quickly, as they are endothermically fissioned by the impact of the bounce shock. The resulting separated protons are more susceptible

to electron capture than their parent nuclei, speeding electron capture and dissipating even more of the bounce shock energy in the form of a shock breakout neutrino burst [4]. Simulations indicate that in only a few hundred kilometers, the unaided bounce shock will stall and become a stationary accretion front [1].

This model is incomplete, as supernovae are observed to explode into space. The solution is expected to lie in the immense neutrino flux coming from the collapsed core. As the core compresses, electrons are captured on protons, leading to the creation of a neutron star at the center of the supernova. The extreme temperatures caused by the collapse and the extent to which the proto-neutron star traps all charged particles and photons inside it causes it to cool by neutrino emission, releasing 99% of its energy from the gravitational collapse not as kinetic energy in the bounce shock, but as neutrinos [1]. The proto-neutron star has an extremely short mean free path for neutrinos of only a few meters [1], so instead of immediately streaming out of the star, the neutrinos leave in the order of a few seconds. A fraction of these neutrinos are suggested to interact with the star in a gain region behind the shock, causing net heating and empowering the shock to lift the outer layers of the star into space [4].

Because this type of supernova creates such a huge neutrino pulse carrying energy on the order of 0.1 solar masses [5], the burst of neutrinos from supernovae throughout the Milky Way can be observed in detectors on Earth, as seen during the SN1987A explosion [6]. Since the majority of these neutrinos stream through the outer layers of the star without interacting, they can be used to see conditions within the collapsing core directly. Neutrino detection can also give a warning to astronomers to watch for a supernova optically, as the shock takes time to make its way to the previously undisturbed surface of a star and allow the release of light from the supernova. The Supernova Early Warning System (SNEWS, [7]) exists to coordinate this announcement worldwide.

1.1.3 Supernova Questions

There are multiple models attempting to explain how supernovae occur. Neutrino data from the core of the supernova could help to refine these models, and lend information

about the phenomena created by supernova explosions.

Although it is not specifically known how the highly energetic gamma-ray bursts observed throughout the universe are created, their detection has been associated with supernovae, and their characteristic high power over a short duration suggests a high energy source such as a supernova [1]. A better understanding of supernovae could explain the conditions necessary for these events.

The observed abundances of heavy nuclei suggest that there is a process in which neutrons are rapidly captured on large nuclei, known as the rapid neutron capture process or r-process. Supernovae are also the expected location of the r-process [8]. A better model of the supernova explosion could help nuclear physicists understand this process.

Free neutron stars are observed to have large velocities in excess of the local galactic speed by 450 $\mathrm{km/s}$, suggesting a large asymmetry developed during their supernova explosions, the cause of which has not yet been discovered [1].

1.2 Neutrino Physics

The Standard Model of particle physics contains two distinct groups of particles: bosons, with integer spins, and fermions, with half-integer spins. The bosons act as carriers of the forces between fermions (Figure 1.1), with photons (γ) carrying the electromagnetic force, W and Z bosons carrying the weak force, and gluons (g) carrying the strong force.

Fermions are divided into quarks, which interact via the strong force, and leptons, which do not. The neutral leptons are referred to as neutrinos. Because they have no charge, they also cannot interact via the electromagnetic force and are left with only the weak force and gravity. This gives neutrinos very small interaction cross sections with normal matter.

Fermions have three generations, represented in the neutrino sector by three flavours of neutrinos: electron neutrinos ν_e, muon neutrinos ν_μ, and tau neutrinos ν_τ.

Neutrinos produced in core-collapse supernovae have distinct energy spectra across flavours. ν_e and $\overline{\nu_e}$ can undergo charged-current reactions with neutrons and protons respectively, increasing their interaction cross sections compared to those of ν_μ and ν_τ

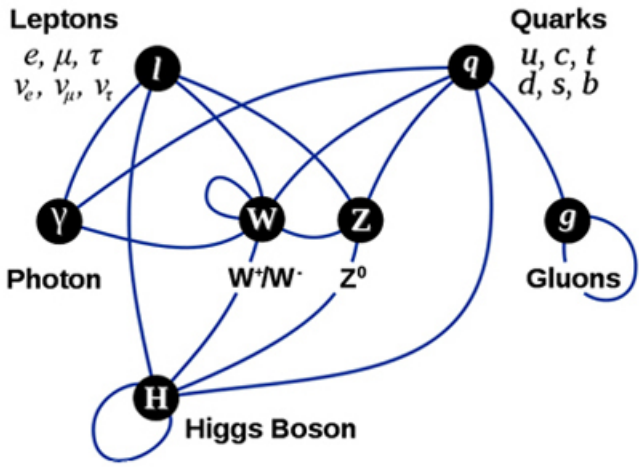

FIGURE 1.1: Standard model interactions [9]

(together denoted as ν_x) which have corresponding charged leptons which are too massive to be produced at supernova temperatures, prohibiting their charge current interactions. A higher cross section causes detected ν_e and $\overline{\nu_e}$ to scatter from shallower and hence cooler depths in the proto-neutron star, causing them to have lower average energies than the ν_x. The higher abundance of neutrons relative to protons similarly causes a higher interaction rate for ν_e compared to $\overline{\nu_e}$, resulting in three separate spectra with $E(\nu_e) < E(\overline{\nu_e}) < E(\nu_x)$ (Figure 1.2) from 3 separate 'neutrinospheres', or surfaces of last scattering, with $R(\nu_e) > R(\overline{\nu_e}) > R(\nu_x)$ [10].

The energy spectra of neutrinos are expected to be 'pinched' at high and low energies compared to thermal spectra, due to lower neutrino production at low energies and to higher neutrino interaction cross sections proportional to E^2 for high energy neutrinos leaving the neutron star [12].

Neutrinos produced in a supernova undergo some flavour changes before they reach Earth. These changes are caused by their time in flight (§1.2.1), their interaction with matter (§1.2.2), and their interaction with other neutrinos (§1.2.3).

The flavour dependence of the energy spectra of core-collapse supernova neutrinos and of interaction cross sections in detectors allows these changes to have potentially large effects on the number of neutrinos seen in different neutrino detectors.

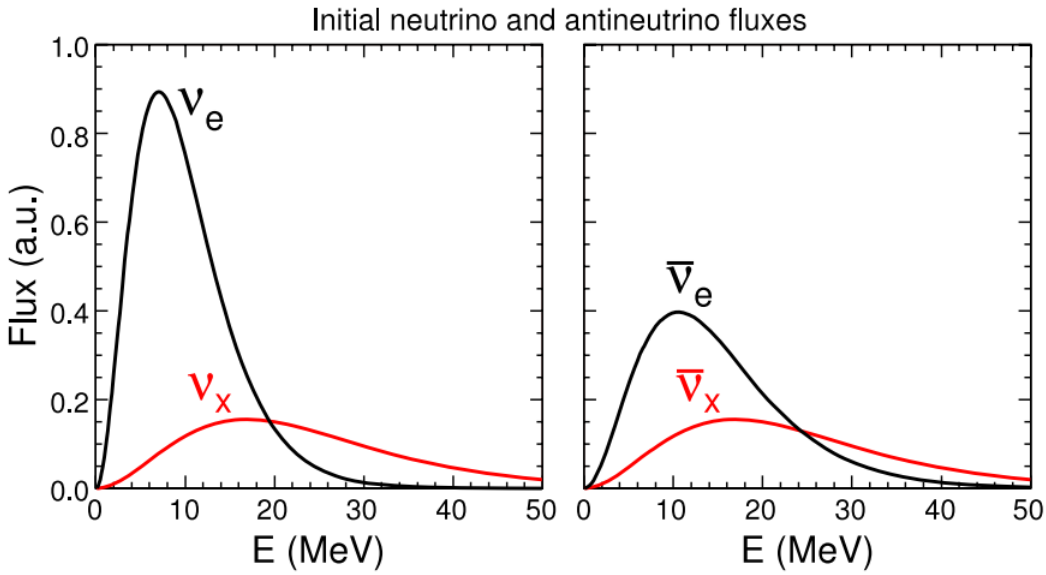

FIGURE 1.2: Energy spectrum of supernova neutrinos at $r = 10\,\mathrm{km}$ [11].

1.2.1 Vacuum Oscillations

All particles evolve in time in accordance with the Schroedinger equation:

$$i\hbar\frac{d}{dt}\left|a\right\rangle = H\left|a\right\rangle \tag{1.10}$$

For a neutrino mass eigenstate in its rest frame, Equation 1.10 has the solution $|a(t)\rangle = e^{\frac{-i}{\hbar}(m\tau)}\,|a(0)\rangle$, where τ is the time in the neutrino mass state rest frame. In the lab frame, this is seen as $\tau = \gamma(t - \frac{\vec{v}\cdot\vec{x}}{c^2})$. This makes the state vector in the lab frame $|a(t)\rangle = e^{\frac{-i}{\hbar c^2}(Et-\vec{p}\cdot\vec{x})}\,|a(0)\rangle$. This solution can be simplified for high energies in natural units with $t \approx L$, $E = \sqrt{p^2+m^2} \approx p + \frac{m^2}{2E}$ to

$$|a(t)\rangle = e^{-i\frac{m^2}{2E}L}\,|a(0)\rangle \tag{1.11}$$

The three flavour states of neutrinos do not directly correspond to the three mass states. Instead they are related by the unitary Pontecorvo Maki Nakagawa Sakata (PMNS) matrix U. This can be combined with Equation 1.11 to show the propagation of the flavour

states:

$$|\nu_\alpha\rangle = \sum_{i=1}^{3} U^*_{\alpha i} |\nu_i\rangle \tag{1.12}$$

$$|\nu_\alpha(L)\rangle = \sum_{i=1}^{3} U^*_{\alpha i} e^{-i\frac{{m_i}^2}{2E}L} |\nu_i\rangle \tag{1.13}$$

$$|\nu_\alpha(L)\rangle = \sum_{\beta=e}^{\tau} \sum_{i=1}^{3} U^*_{\alpha i} e^{-i\frac{{m_i}^2}{2E}L} U_{\beta i} |\nu_\beta\rangle \tag{1.14}$$

The probability of observing a ν_β after an initial ν_α after distance L is then $P(\nu_\alpha \to \nu_\beta) = |\langle \nu_\beta | \nu_\alpha(L) \rangle|^2$. The different values of m_i as well as the non-diagonal components of U allow this probability to be non-zero for different neutrino flavours. Due to the unitarity of the matrix U, the transition probability with the flavour propagation from Equation 1.14 can be simplified to

$$\begin{aligned} P(\nu_\alpha \to \nu_\beta) =& \delta_{\alpha\beta} - 4\sum_{i>j} Re(U^*_{\alpha i} U_{\beta i} U_{\alpha j} U^*_{\beta j}) \sin^2\left(\frac{{\Delta m_{ij}}^2}{4E} L\right) \\ &+ 2\sum_{i>j} Im(U^*_{\alpha i} U_{\beta i} U_{\alpha j} U^*_{\beta j}) \sin\left(\frac{{\Delta m_{ij}}^2}{2E} L\right) \end{aligned} \tag{1.15}$$

where ${\Delta m_{ij}}^2 = {m_i}^2 - {m_j}^2$. The matrix U can be factored into three mixing angles θ_{12}, θ_{13}, and θ_{23} as well as a complex phase δ:

$$U = \begin{bmatrix} 1 & 0 & 0 \\ 0 & \cos\theta_{23} & \sin\theta_{23} \\ 0 & -\sin\theta_{23} & \cos\theta_{23} \end{bmatrix} \begin{bmatrix} \cos\theta_{13} & 0 & e^{-i\delta}\sin\theta_{13} \\ 0 & 1 & 0 \\ -e^{i\delta}\sin\theta_{13} & 0 & \cos\theta_{13} \end{bmatrix} \begin{bmatrix} \cos\theta_{12} & \sin\theta_{12} & 0 \\ -\sin\theta_{12} & \cos\theta_{12} & 0 \\ 0 & 0 & 1 \end{bmatrix} \tag{1.16}$$

The current values of these parameters can be seen in Table 1.1.

Swapping the values α and β in $P(\nu_\alpha \to \nu_\beta)$ (Equation 1.15) has the same effect as replacing U with U^* and CPT invariance specifies that $P(\nu_\alpha \to \nu_\beta) = P(\overline{\nu_\beta} \to \overline{\nu_\alpha})$. Together, this implies that

$$P(\overline{\nu_\alpha} \to \overline{\nu_\beta}; U = A) = P(\nu_\alpha \to \nu_\beta; U = A^*) \tag{1.17}$$

The product $(U^*_{\alpha i} U_{\beta i} U_{\alpha j} U^*_{\beta j})$ in Equation 1.15 will pick up a phase of 0, δ or $-\delta$ depending

Parameter	Values
$\sin^2(\theta_{12})$	0.308 ± 0.017
$\sin^2(\theta_{23})$	$0.437^{+0.033}_{-0.023}(NH), 0.455^{+0.039}_{-0.031}(IH)$
$\sin^2(\theta_{13})$	$0.0234^{+0.0020}_{-0.0019}(NH), 0.0240^{+0.0019}_{-0.0022}(IH)$
Δm^2	$2.43 \pm 0.06 * 10^{-3} eV^2(NH), -2.38 \pm 0.06 * 10^{-3} eV^2(IH)$
Δm^2_{21}	$7.54^{+0.26}_{-0.22} * 10^{-5} eV^2$
δ/π	$1.39^{+0.38}_{-0.27}(NH), 1.31^{+0.29}_{-0.33}(IH)$

TABLE 1.1: Values of PMNS matrix parameters and mass differences as of 2014 [13]. Δm^2=$m^2_3 - 0.5(m^2_1 + m^2_2)$

on the α, β, i, and j. The conjugation of U multiplies this phase by -1, so a non-zero value of δ would change the sign in the last term of Equation 1.15, demonstrating a difference between $P(\nu_\alpha \rightarrow \nu_\beta)$ and $P(\overline{\nu_\alpha} \rightarrow \overline{\nu_\beta})$. This means that the PMNS matrix violates CP symmetry for any $\delta \neq 0$.

The absolute scale of the neutrino masses cannot be determined by oscillation measurements, since the oscillations depend only on the mass differences between the mass states. Because the measured mass differences Δm^2_{31} and Δm^2_{23} are not statistically significantly different (Table 1.1), it is also as yet unknown whether these mass states follow the "normal hierarchy" ($m_1 < m_2 < m_3$) or the "inverted hierarchy" ($m_3 < m_1 < m_2$) (Figure 1.3).

For cases where only two neutrino flavours are relevant, and only one mass difference can be seen at the distance and energy in question, the transition probability can be simplified to use one mixing angle θ. This is typically done with ν_e and $\nu_x = \nu_\mu + \nu_\tau$ since the electron neutrinos can be much more easily detected in charged-current interactions.

In this case, the neutrino flavour and mass states are related by a rotation matrix in θ:

$$\begin{bmatrix} \nu_\alpha \\ \nu_\beta \end{bmatrix} = \begin{bmatrix} \cos\theta & \sin\theta \\ -\sin\theta & \cos\theta \end{bmatrix} \begin{bmatrix} \nu_1 \\ \nu_2 \end{bmatrix} \tag{1.18}$$

The transition probability then becomes

$$P(\nu_\alpha \rightarrow \nu_\beta) = \delta_{\alpha\beta} + (1 - 2\delta_{\alpha\beta}) \sin^2(2\theta) \sin^2\left(\frac{\Delta m^2}{4E} L\right) \tag{1.19}$$

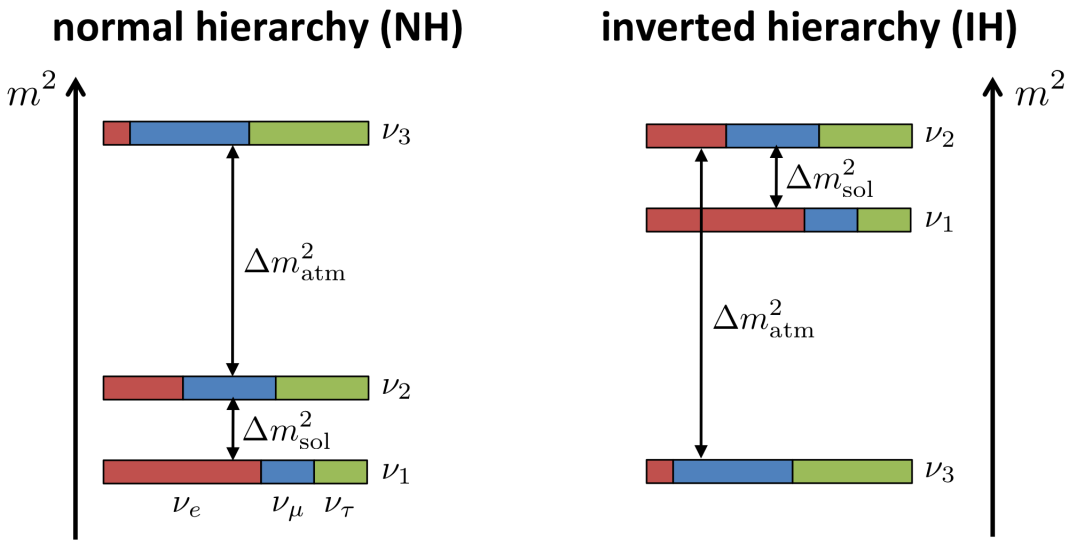

FIGURE 1.3: The possible neutrino hierarchies. [14]

This approximation can be useful for examining additional neutrino effects.

1.2.2 Matter Effects

Matter present along a neutrino's path can change the flavour distribution of the neutrinos. When neutrinos travel though high densities of matter, their Hamiltonians must be changed from the vacuum Hamiltonian based on the coherent interactions they undergo. The neutral current interactions with protons, neutrons, and electrons are the same for all flavours and hence have no effect on flavour changes. However, electron neutrinos and electron anti-neutrinos can undergo charged-current coherent scattering (Figure 1.4).

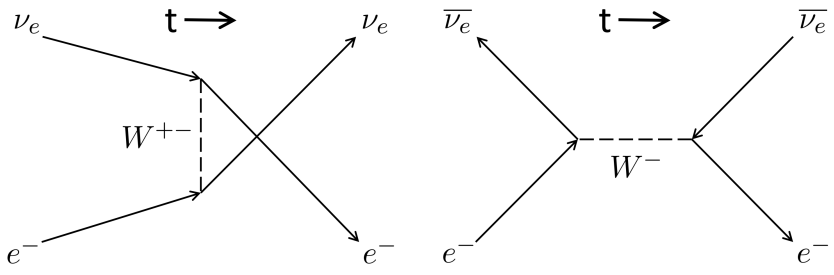

FIGURE 1.4: Scattering diagrams possible for ν_e ($\overline{\nu_e}$) but not for ν_μ or ν_τ ($\overline{\nu_\mu}$ $\overline{\nu_\tau}$)

These interactions create a change in potential for the electron neutrino and anti-neutrino of $\Delta V = \sqrt{2} G_F n_e$, where n_e is the electron density and G_F is the Fermi Constant, $2.22 \times 10^{-41} \mathrm{eVm}^3$. This change in the Hamiltonian causes the mass eigenstates to be modified, causing neutrino flavour transitions known as the Mikheyev Smirnov Wolfenstein (MSW) effect.

These transitions can be approximated with the two-neutrino Hamiltonian, relating ν_e and $\nu_x = \nu_\mu + \nu_\tau$. The neutral-current interactions contribute only a diagonal component and so have no effect on flavour change, but charged-current effects enhance the energy of only the H_{ee} term. This can be seen as a modification of the diagonal components of the vacuum Hamiltonian,

$$H = I(p + \frac{{m_1}^2 + \frac{1}{2}\Delta m^2}{2E} + V_Z + \frac{1}{2}V_W) + \frac{\Delta m^2}{4E} \begin{bmatrix} -\cos(2\theta) & \sin(2\theta) \\ \sin(2\theta) & \cos(2\theta) \end{bmatrix} + \begin{bmatrix} \frac{V_W}{2} & 0 \\ 0 & -\frac{V_W}{2} \end{bmatrix} \quad (1.20)$$

Where V_Z is the potential from the neutral current interaction, $V_W = \sqrt{2} G_F n_e$ is the potential from charged-current interactions, and θ is the mixing angle of the two mass states for the two neutrino categories in question.

Ignoring the multiples of the identity matrix, this gives a Schroedinger equation for the two states of

$$i\frac{d}{dt}\begin{bmatrix} \nu_e \\ \nu_x \end{bmatrix} = \begin{bmatrix} \frac{V_W}{2} - \frac{\Delta m^2}{4E}\cos(2\theta) & \frac{\Delta m^2}{4E}\sin(2\theta) \\ \frac{\Delta m^2}{4E}\sin(2\theta) & \frac{\Delta m^2}{4E}\cos(2\theta) - \frac{V_W}{2} \end{bmatrix} \begin{bmatrix} \nu_e \\ \nu_x \end{bmatrix} \quad (1.21)$$

For $V_W \approx \frac{\Delta m^2}{2E} cos(2\theta)$, the relevant Hamiltonian has very small diagonal components, causing the neutrino flavours to transfer towards the eigenstates of equal e and x flavour composition.

For much larger values of V_W, the Hamiltonian can become much more diagonal than the vacuum Hamiltonian. If an electron neutrino is created in a region where this is the case, it is nearly in an eigenstate of the matter Hamiltonian already, causing it to be in a single mass state. If the matter density falls off adiabatically, this neutrino will remain in an eigenstate of the changing Hamiltonian. As the potential falls off with density, a

neutrino exiting a star will fall to the highest mass state below the potential it was created at.

Both of these explanations of electron neutrino disappearance cannot work to convert large numbers of neutrinos if the hierarchy is arranged such that the electron neutrino is primarily composed of the heavier mass state. If $\Delta m^2 < 0$ (or equivalently if $\theta > \frac{\pi}{4}$) then the diagonal terms of the Hamiltonian in Equation 1.21 grow in magnitude instead of vanishing with increasing V_W. This prevents the transition-dominated Hamiltonian from forming, or transforms the initial electron-flavoured neutrino into its own most plentiful mass state.

This is not the case for the mass states ν_1 and ν_2, but may be true for the transition of ν_1, ν_2 to ν_3 in the case of the inverted mass hierarchy (Figure 1.3). This would eliminate the resonance effect for neutrinos and instead create the effect for anti-neutrinos, as their propagation is affected by the opposite sign of V_W [15].

Neutrinos in the sun are created with a few MeV of energy, making the order of energy for resonance to the ν_2 state $V_W \approx \frac{\Delta m^2}{E} \approx 10^{-5} \frac{eV^2}{MeV}$. The density at the center of the sun provides $V_W = 8 \times 10^{-6} \frac{\mathrm{eV}^2}{\mathrm{MeV}}$ [16], allowing a resonance to ν_2 but prohibiting a resonance to ν_3 regardless of the hierarchy.

In supernovae however, the densities are immensely higher. A density before any shock effects of $\rho(r) \approx 10^{14}(\frac{r}{\mathrm{km}})^{-2.4}\mathrm{g/cm}^3$ [17] results in matter effects dwarfing Δm^2_{31} up to a radius of 10,000 km. The resulting effects on neutrino flavour may be complicated by the deviation from an adiabatic change in electron density, either from the initial distribution of matter or from the propagation of the shock front [18].

Because of the MSW effect, the state of the supernova neutrinos may also be changed by earth matter effects [5]. These effects would be dependent on the location of the detector.

1.2.3 Collective Oscillations

Neutrinos in a supernova can also be subject to extensive collective effects from the presence of other neutrinos. Because the interaction strength between neutrinos is proportional to $(1 - \cos(\theta)) \propto \theta^2$, the effective neutrino density falls off with r^{-4}. Because of this, collective effects are expected to end after the neutrinos have traveled only around $100\ \mathrm{km}$. This suggests that the neutrino collective effects may end well before the MSW resonance, allowing the effects on the spectrum to be separated.

Because neutrinos can scatter to a different neutrino flavour when mixed with anti-neutrinos, the neutrino collective effects modify all terms of the two-neutrino flavour Hamiltonian:

$$i\frac{d}{dt}\begin{bmatrix}\nu_e\\ \nu_x\end{bmatrix} = \begin{bmatrix}\frac{V_W}{2} + B - \frac{\Delta m^2}{4E}\cos(2\theta) & \frac{\Delta m^2}{4E}\sin(2\theta) + B_{er}\\ \frac{\Delta m^2}{4E}\sin(2\theta) + {B_{er}}^* & \frac{\Delta m^2}{4E}\cos(2\theta) - \frac{V_W}{2} - B\end{bmatrix}\begin{bmatrix}\nu_e\\ \nu_x\end{bmatrix} \tag{1.22}$$

These effects are nonlinear as the oscillation parameters B and B_{er} depend on the neutrino flavour composition. Collective oscillations do conserve lepton number and energy, resulting in transitions of the type $\nu_e + \overline{\nu_e} \longleftrightarrow \nu_x + \overline{\nu_x}$, with the neutrino pair energy being conserved [19]. This leads to a swap in the flavour's energy spectrum. In the inverted hierarchy the high end of the energy spectrum is almost completely swapped between ν_e and ν_x.

1.2.4 Neutrino Physics From Supernova

The relative energy spectra and fluxes of neutrinos and anti-neutrinos are relevant to many processes in a supernova explosion. If multiple types of detectors are running at the time of the next supernova, insight could be gained into these processes.

The r-process requires a neutron-rich environment for the development of heavy nuclei [8]. For this environment to be found in a supernova, constraints are placed on the energy and flux of the ν_e flux relative to the $\overline{\nu_e}$ flux [20], as the reaction $\nu_e + n \rightarrow p + e^-$

reduces the neutron concentration and the reaction $\overline{\nu_e} + p \rightarrow n + e^+$ enhances it. Measurements of these fluxes can determine if the r-process can occur in supernovae in the manner it is currently envisioned.

Neutrinos of different hierarchies undergo vastly different transformations from both the MSW effect and coherent oscillations in supernovae [21]. The measurement of the flavour composition of supernova neutrinos could constrain the order of the neutrino mass states.

The detection of a neutrino burst could display the existence of a core-collapse with a stalled bounce shock, which would not result in any optical explosion. A short neutrino burst with a sharp cut-off could show the properties of the proto-neutron star as it collapses into a black hole.

Chapter 2

HALO

The Helium And Lead Observatory (HALO) is a detector built to measure the neutrino burst of a core-collapse supernova. The target mass consists of 79 tonnes of lead, which is instrumented with ^{3}He proportional counters to detect neutrons released by neutrino interactions with lead.

2.1 Goals of HALO

HALO was built to be a low-maintenance lead-based supernova detector. Since the rate of supernovae the Milky Way is expected to be about 2.5 per century [22], it is important that HALO can be operated for decades to detect the next galactic supernova.

HALO provides a unique flavour sensitivity in charged-current interactions for supernova neutrinos. Liquid scintillator detectors and water Cerenkov detectors are primarily sensitive to electron anti-neutrinos interacting with hydrogen nuclei. Lead is strongly Pauli-blocked against charged-current anti-neutrino interactions due to its large neutron excess: no states are available for neutrons with quantum numbers similar to those of the protons in the lead nucleus. This makes lead primarily sensitive to electron neutrino interactions (Figure 2.1). HALO is currently the only operating lead-based supernova detector. SNOLAB will also have anti-neutrino sensitivity from the liquid scintillator based SNO+ experiment [23].

Because other detectors sensitive to supernova neutrino bursts are focused on other physics goals, they are often turned off for maintenance, upgrades, or calibrations. HALO is aimed at minimizing such down times to provide reliable supernova monitoring. To

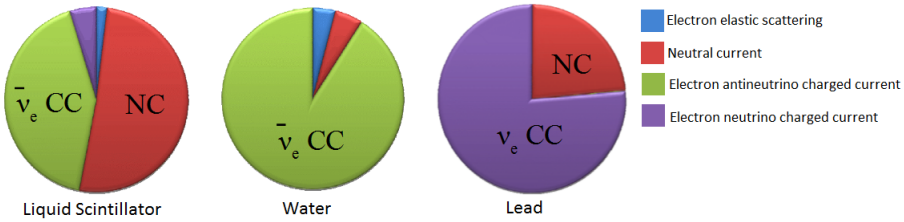

FIGURE 2.1: Neutrino flavour sensitivities of the currently deployed target materials [24]. HALO is currently the only detector in SNEWS with a lead target.

this end the detector has many redundant systems, such as two data acquisition computers, and separate sets of high voltage supplies and data processing electronics.

2.1.1 Low Maintenance Data Acquisition

HALO has a monitoring web-page containing live updates of the detector status (Figure 2.2). This page will soon be available to regularly confirm that the detector is still running with little effort. Longer term metrics are also recorded in an SQL database and displayed on the monitoring page, allowing experimenters to scan the recent detector performance for stability.

The electronics are duplicated up the point of the connection to the data acquisition computers, and the mapping of hardware in the detector places each half of the ^{3}He counter array under the control of a separate set of electronics. This allows continued supernova monitoring if a single piece of hardware is compromised.

Although only one data acquisition computer is running the detector at a time, both are on and running ORCA [25], the data acquisition software. The control and readout of the detector is automatically taken over by the inactive data acquisition computer if the running one stops responding, and is regularly toggled between the computers during normal running.

One common threat to the live time of the detector are power outages. The HALO UPS provides for 3 hours of running after a power outage and allows the detector to automatically shut itself down properly when the batteries are close to discharged. This

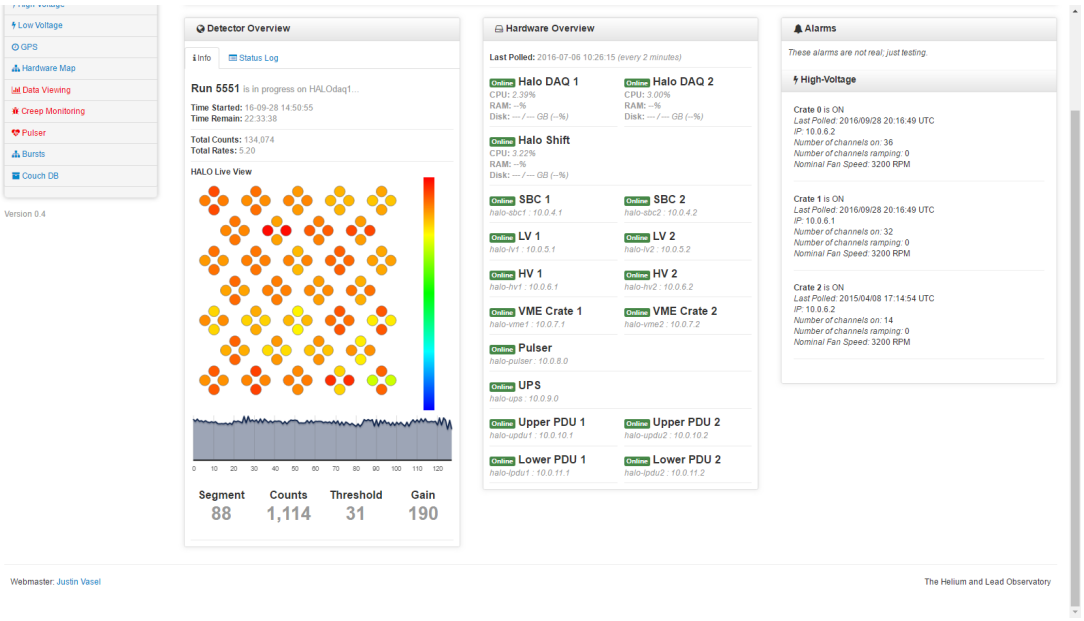

FIGURE 2.2: Monitoring page for the HALO detector, designed by Justin Vasel. The left panel shows the neutron counter array with colours corresponding to the number of counts read in the current run. The electronic hardware status can be seen in the center.

was implemented in October 2016. A clean shutdown allows the detector to automatically turn on and start running as soon as power is restored.

From September 1, 2012 to February 20, 2017, HALO had an uptime of 96% (Figure 2.3). The above methods are expected to improve this further in the future.

2.2 Components

The lead matrix of the HALO detector is 206 cm tall, 243 cm wide and 308 cm deep (Figure 2.4). This is supported by a steel structure in addition to iron rings throughout the detector to prevent the lead from undergoing creep. The lead is surrounded by neutron shielding in the form of water boxes and plastic boards. These water boxes consist of a cardboard box frame containing a bag with about 20kg of water. The corners of the boxes are filled with plastic beads.

The lead matrix is outfitted with 32 groups of 4 ^{3}He counters. Each individual counter is surrounded with a high density polyethylene (HDPE) tube to moderate neutrons. The counters are paired off with another counter in their group, resulting in 64 channels 2.5.

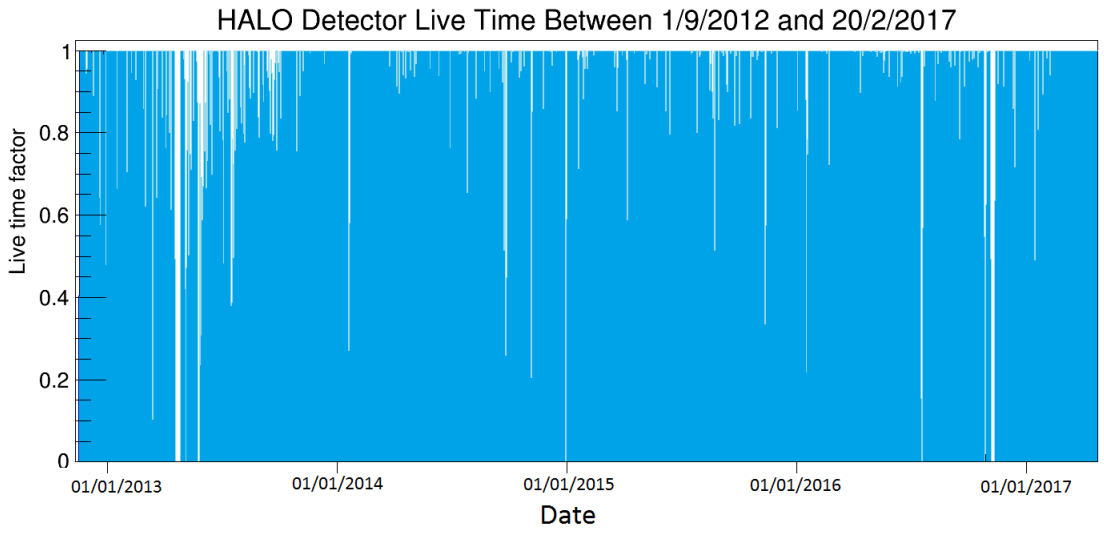

FIGURE 2.3: Live-time history of the HALO detector.

2.2.1 Lead Matrix

HALO uses 79 tonnes of lead as the target material for neutrinos, in the form of 864 lead blocks from the decommissioned AECL Cosmic Ray Laboratory [27]. Each block consists of an annulus with two rectangular "ears", and is painted to prevent the formation of toxic lead carbonate. Each block weighs 91 kg [28]. These blocks are arranged to form 32 "bores" each 27 blocks deep. The bottom 5 rows of bores contain the iron rings to support them [26]. There are 28 rings per bore, each weighing 3.7 kg [29].

2.2.2 Neutron Counters

HALO contains 128 neutron counters composed of cylinders with a 5 cm diameter and lengths from 2.5 meters to 3 meters. As these counters were previously used in the SNO experiment, they were filled to a high pressure of 2.5 atm to withstand external water pressure. 85% of this pressure is made up by ^{3}He gas, with the remainder made with CF_4 gas. The ^{3}He neutron counters are proportional counters, meaning that the size of the voltage pulse they produce is proportional to the energy deposition in the counter gas. The counters are made of low background materials [30] and are highly sensitive to

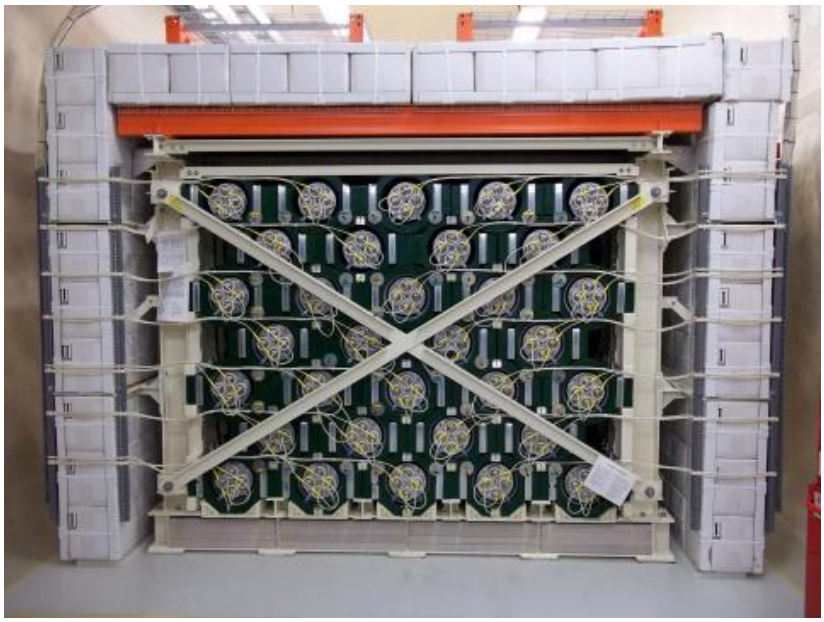

FIGURE 2.4: HALO, front face open. The lead matrix is painted dark green [26], with the steel support structure painted white. Water boxes can be seen around the sides and top, with plastic lumber across the bottom.

neutrons. ^{3}He has a non-elastic cross-section for thermal neutrons of 5300 barns, giving thermal neutrons within the counters an absorption length of $3.5\ \mathrm{cm}$ [31].

2.2.3 Calibration Tubes

The calibration of HALO was carried out with a ^{252}Cf neutron source (§4), which releases neutrons by spontaneous fission (SF). As of April 2016 the source had a SF rate of 21.5 Hz (§4.4.3). This source was doubly encapsulated in a cylindrical enclosure to meet SNOLAB's cleanliness requirements (Figure 2.6).

To allow this source to be used in the detector, 40 straight copper tubes were installed, which run from the front to the back of the lead matrix. With the front shielding in place, 24 of these tubes are extended through the shielding to make them accessible with the detector closed (Figure 2.7). The calibration source can be positioned anywhere inside a calibration tube using a rod screwed to the back of the source (Figure 2.8).

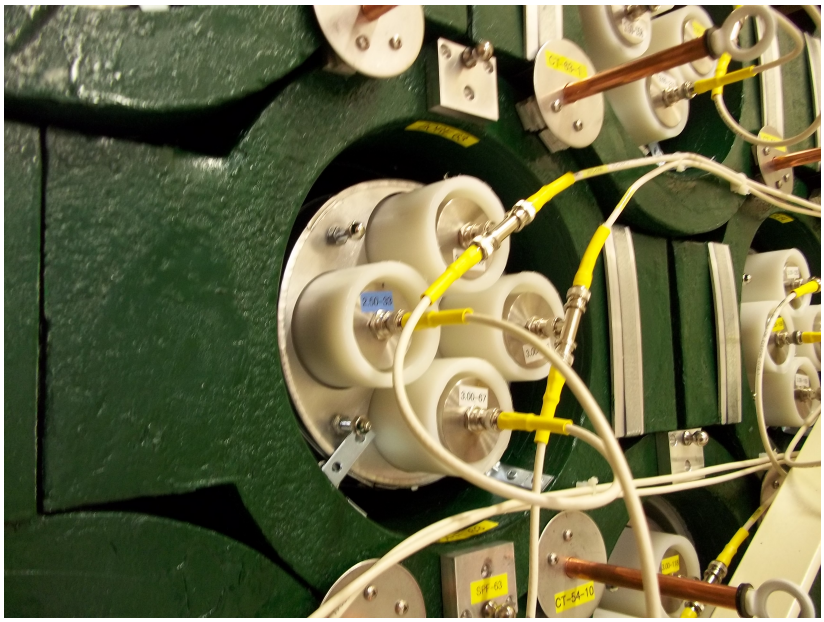

FIGURE 2.5: A bore in the HALO detector. Four ^{3}He counters can be seen in the bore, paired in groups of two. Copper calibration tubes can be seen above and below the bore.

2.2.4 Shielding

The most relevant type of background radiation for HALO is neutrons. These are produced in the rock from nuclear decays as well as from muon interactions. Water and plastic lumber were installed to shield the detector from these neutrons.

The sides, top, and back of the detector are shielded with roughly cubic foot boxes containing a bag of 21.4 liters of water as well as plastic beads to fill in the corners of the boxes. This creates a shield with 27 $\mathrm{g/cm^2}$ of water and plastic [32]. The bottom of the detector is shielded with a 22 cm layer of plastic lumber, providing 20 $\mathrm{g/cm^2}$ of shielding. This is comparable the shielding from the water boxes in hydrogen content, but there are some gaps in the shielding at the bottom of the detector due to the support structure [33].

To shield the front of HALO, 88 water boxes were added, between which a 27.6 cm thick layer of plastic lumber was placed in the area around the calibration tubes (Figure 2.8). Adding this layer of shielding to the front of HALO reduced the neutron background rate to 1294 ± 8 neutrons per day from the previous rate of roughly 9000 per day with the Cf source storage barrel in front of the detector, or 6423 ± 13 neutrons per day before the

FIGURE 2.6: The doubly encapsulated ^{252}Cf source

arrival of the source.

The neutron detection efficiencies through the water walls were tested with the ^{252}Cf source, after the source strength had been well determined by internal calibrations. Efficiency is determined as $\epsilon = \frac{(detected\ neutrons)-(expected\ background)}{neutrons\ produced\ by\ source}$. The results are shown in Table 2.1. The sizes of gaps between the shielding and the detector as well as the amount of lead on the outside of the core detector matrix are different on the sides, top, and back, so some variation in the efficiencies is expected.

Location	Detection Efficiency
Center of top	(0.399±0.013)%
Center of back	(0.152±0.013)%
Center of left side	(0.210±0.014)%
Center of right side	(0.233±0.015)%

TABLE 2.1: Detection efficiencies for neutrons produced outside the shielding by the ^{252}Cf source. Left and right sides are for someone facing the detector from the drift.

SNOLAB has a neutron flux of $8000\,\mathrm{m}^{-2}\mathrm{day}^{-1}$ [34], roughly half of which are thermal neutrons. Comparing this flux to the shielded count rate of 1294±8 neutrons per day suggests there is an average detection efficiency of about 0.3% for neutrons at the surface of the water boxes. This would suggest a higher efficiency in the center of each face than most of the measured efficiencies from Table 2.1, but the differences between the Californium and background neutron spectrum may well be able to account for detection efficiency differences of this size.

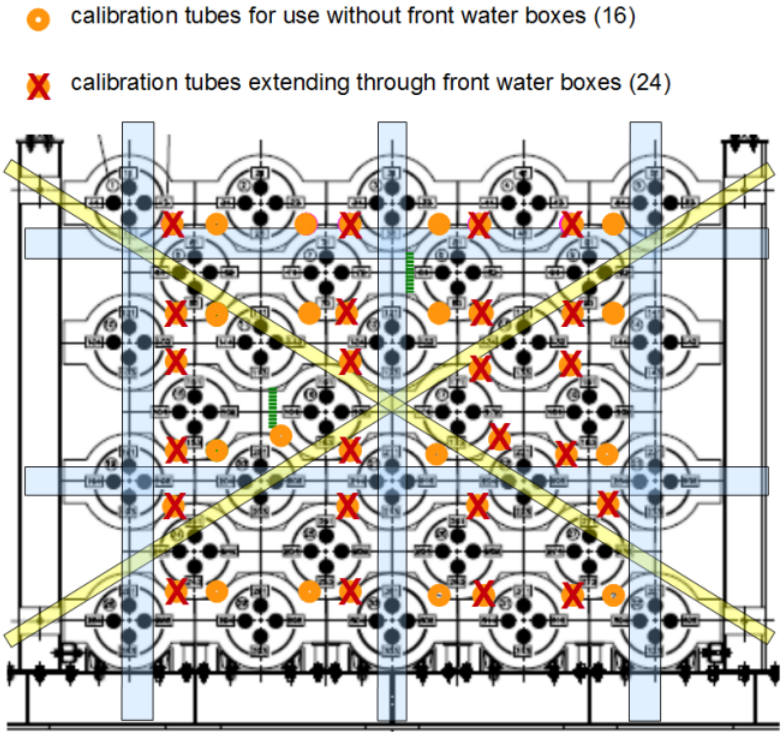

FIGURE 2.7: Locations of calibration tubes in HALO. Tubes are named by the row and distance right of the bore beneath them and the clock position relative to that bore. For example, the tube in the top right would be CT-64-1.

2.3 Neutrino Detection

2.3.1 Flavour Sensitivity

Neutrinos can interact with matter through electron scattering or through charged or neutral current interactions with atomic nuclei. HALO aims to detect neutrinos through their interaction with the lead nucleus.

2.3.2 Detection Method

Most of the neutrino detections in HALO in the event of a supernova will come from the electron neutrino charged-current interaction.

$$\nu_e + {}^{k}\text{Pb} \rightarrow e^{-} + {}^{k}\text{Bi}^{*} \tag{2.1}$$

FIGURE 2.8: Calibration of HALO with the front shielding in place.

$$^{k}\text{Bi}^{*} \rightarrow^{k-1} \text{Bi} + \gamma + n \tag{2.2}$$

Other neutrinos can still be detected by the neutral current interaction.

$$\nu_x +^{k} \text{Pb} \rightarrow \nu_x +^{k} \text{Pb}^{*} \tag{2.3}$$

$$^{k}\text{Pb}^{*} \rightarrow^{k-1} \text{Pb} + \gamma + n \tag{2.4}$$

The resulting neutron then travels throughout the detector. Because of high mass and low absorption cross section of the lead nuclei, the neutron will likely be thermalized in the plastic surrounding the ^{3}He counters. ^{3}He has a thermal non-elastic neutron cross section of 5334 barns, much larger than hydrogen's 0.333 barns [31], so thermal neutron entering a counter will be captured on a ^{3}He nucleus. This creates an excited state of ^{4}He, which then decays:

$$^{4}\text{He}^{*} \rightarrow {}^{3}\text{H} + p + 764\,\text{keV} \tag{2.5}$$

The decay energy in the proton and triton is deposited in the counter gas by ionization.

These free electrons then accelerate towards the anode wire running down the center of the counters, which is held at a high voltage of roughly 1700 V. Near the anode wire, the electrons have sufficient energy for additional ionization, creating an avalanche which results in a measurable charge deposition on the axial wire when the electrons arrive. This signal is enhanced by pre-amps and digitized by shaper cards, also refereed to as Analog to Digital Converters, or ADCs.

Because there are only two bodies in the decay, energy is split consistently between the triton and proton, with the proton taking 573 keV and the triton taking 191 keV. This results in three scenarios for energy deposition: if a neutron capture occurs deep in the counter or if the line connecting the ejected particles is approximately parallel to the axis of the counter, all of the energy will be deposited in the gas, and the subsequent electrons collected on the anode wire.

The proton with 573 keV of energy has a range of 5 mm in the counter gas. If the neutron is captured close to the wall of the detector, the emitted proton could leave the gas volume before depositing all of its energy. This results in an energy distribution from 191 keV to 764 keV.

The triton with 191 keV of energy has a range of only 1 mm. with If the capture occurs extremely close to the wall, the triton could escape the gas volume. This results in energies from 573 to 764 keV These features can be seen in the neutron energy deposition spectrum (Figure 2.9).

2.3.3 Neutrino Energy Resolution

Neutrinos from supernovae are often assumed to follow a Fermi-Dirac distribution [10] (Equation 2.6), where ϵ is the neutrino energy, T is the neutrino temperature, η_α is the pinching parameter, and $f_{\eta_\alpha}(\epsilon)$ is the neutrino flux.

$$f_{\eta_\alpha}(\epsilon) \propto \frac{\epsilon^2}{1 + e^{(\epsilon/T - \eta_\alpha)}} \tag{2.6}$$

Neutrino interactions with lead can cause the emission of one or two neutrons. The number of neutrons that can possibly be emitted is a function of the neutrino energy

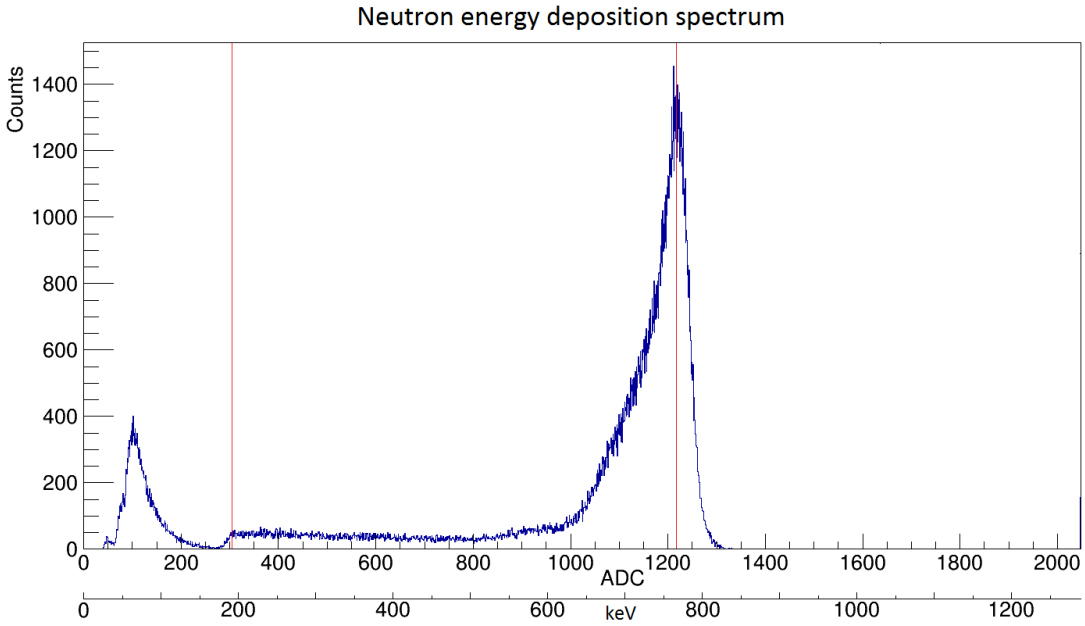

FIGURE 2.9: Spectrum of energy deposition from neutron capture with the Cf source. The neutron full energy peak is marked with a red line at 764 keV (1223 raw ADC), and the minimum possible energy deposition from a neutron capture is marked with a red line at 191 keV, which is deposited when a proton fully escapes the counter. A small feature caused by neutron capture with triton escape can also be seen from 573 keV to 764 keV. Data is from run 5384 with the source in CT-33-10 at Z=0 for 80 minutes.

(Table 2.2).

Isotope	1n (CC)	1n (NC)	2n (CC)	2n (NC)
^{206}Pb	11.31	8.09	19.77	14.82
^{207}Pb	11.01	6.74	18.03	14.82
^{208}Pb	10.28	7.37	18.37	14.11
Weighted Mean	10.69	7.40	18.64	14.44

TABLE 2.2: Thresholds for neutrino induced neutron emission in lead in units of MeV, calculated from the difference in initial and final energy with masses from [35]. Relative cross section will still vary above the threshold energies [5].

Because the average neutrino energy in proposed supernova models is of the order of 20 MeV [36], the ratio of two neutron to one neutron events from a supernova is correlated with the average neutrino energy, allowing a measurement to be made of the neutrino temperature and pinching parameter.

Some neutrons will escape HALO without detection, so the neutrino efficiency will

affect the ratio of 1n and 2n events observed. Because neutrino interactions can occur anywhere in the lead, the conservation of 2n events must be tested over random locations in the lead. To do this, an accurate simulation of the detector is necessary.

Chapter 3

Monte Carlo Studies

A Monte Carlo model of HALO exists for simulations related to supernova measurements. This model was built in Geant4 [37]. Revisions were made to the geometry of many detector components to improve the model upon review of the documentation of the components [38]. These components included the lead blocks that make up the target mass of HALO, the steel support structure and support rings, the water and plastic neutron shielding, and the ^{3}He counters, as well as some minor components such as the adhesive and paint used on the detector.

The paint layer on the lead blocks had no accurate documentation, so measurements of the paint layer were required for a valid simulation of the detector.

Revision numbers of the Monte Carlo geometry were included for reference. These are incremented with each geometry modification submitted, as well as with updates to documents kept in the same repository.

3.1 Paint Composition

The paint covering the lead blocks was previously (revision 69) represented in the Monte Carlo geometry by a $1\ \mathrm{mm}$ coating over all the lead, with a density of $1.198\,\mathrm{g/cm^3}$. This amounts to 378 kg of paint on HALO.

This was thought to be too much, given that on the order of 40 liters of paint were used to paint the detector. [26]

The removal of this paint layer from the simulation caused an absolute neutron capture efficiency change of 1.91 ± 0.33 percent between simulation runs with and without

paint, making it an important component of the detector for neutron propagation. This entailed verification of the composition and quantity of paint in HALO.

3.1.1 Determining Paint Mass

To measure paint thickness on the lead blocks, paint was measured directly by cutting along the surface of spare painted lead blocks and pulling paint off with tape. The paint did not come off easily and resulted in many jagged shapes.

The resulting shapes were photographed, uploaded to a computer, and blown up for the area to be counted. The linear density of the tape was measured and the completed tape lifts were weighed to find the mass of paint they acquired.

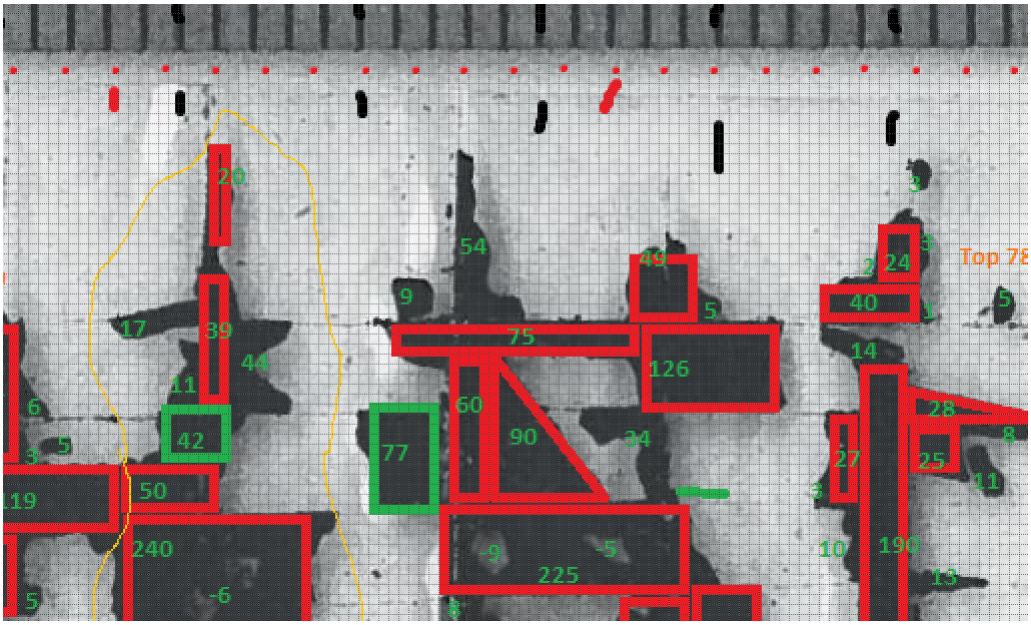

FIGURE 3.1: Counting the area of tape lift A of paint pulled from a lead block. The tape strips were then weighed to find the surface density of the paint.

Using the listed paint density, the masses and areas measured corresponded to a paint thickness of (0.14 ± 0.07) mm. Although this ruled out the 1 mm thickness that had been used in the simulation, the error was much larger than the 3 percent relative error found in recounting areas in the pictures of the tape. This suggests that the tape lifts likely pulled off extra material in some places, or did not pull off the entire paint layer in some locations.

For a more precise measurement of the paint thickness as well as density, a piece of foil was painted and left to dry while standing up.

FIGURE 3.2: Drying green paint on foil to more precisely measure the paint thickness and density

Four 22 cm by 30 cm sheets of foil were measured to determine the unpainted density of the foil. The sample average was $(3.886 \pm 0.071)\ \mathrm{mg/cm^2}$

A 9 cm by 23 cm foil piece painted on both sides was similarly measured to have a density of 19.47 $\mathrm{mg/cm^2}$. If this measurement is taken to have the same relative error as the sample standard deviation of the unpainted foil sheets, the paint density is $(7.791 \pm 0.180)\ \mathrm{mg/cm^2}$.

To measure the thickness of the paint, ten squares were cut from the sides of the painted foil, with the height of the squares in the original standing position roughly evenly distributed. Ten squares were also cut from clean aluminum foil. Both sets of ten squares were piled up and then measures at 10 locations around the pile. This found a paint thickness of $(0.0716 \pm 0.00084)\ \mathrm{mm}$.

The above thickness and surface density results in a dry paint density of 1.087 $\mathrm{g/cm^3}$, slightly less than the density of 1.198 $\mathrm{g/cm^3}$ which was previously used. This density and thickness was implemented in the simulation at revision 82.

3.1.2 Determining Paint Composition

The arrangement of painted foil went from a total mass of paint and foil of 20.31 g to 14.23 g over the drying process. The foil that was painted together with the foil tray attached to catch the paint had a mass of 4.61 g, so 61.3% of the paint's mass remained after drying.

Elemental compositions of the paints had been determined with an Inductively Coupled Plasma Mass Spectroscopy (ICP-MS) study [26]. However, the elements found in this study only summed to 33% of the total mass sampled. As the ICP-MS study cannot detect non-metal, non metals were chosen based on the colour of the paint, as follows (Table 3.1).

All paint contains white paint, commonly composed of TiO_2. Because of this, two moles of oxygen were added for every mole of titanium that was found. A common green dye is phthalocyanine green [39], which has a chemical formula similar to $C_{32}H_2Cl_{13}CuN_8$ [40]. These non-metals were added similarly in proportion to the detected Cu concentration. This resulted in a mass of 100.03% of the sample mass.

As previously found in the ICP-MS study, cobalt, titanium, copper, gadolinium and hafnium have large neutron capture cross sections and hence were included in the simulation. Zirconium and all the non-metals are present in large quantities, and were also included in the simulation. These elements result in a total mass of 99.7 % of the sample mass. This difference is smaller than the error found measuring the paint's density of 2.3 %.

3.1.3 Neutron Detection Effects

Previously, the paint was simulated with only hydrogen, carbon, oxygen, and Titanium (Table 3.1).

The previous paint had a thickness of 1 mm and a density of 1.198 $\mathrm{g/cm^3}$. This means the mass of paint in the detector was reduced by a factor of 0.065. The new paint has more heavy elements, making the quantity of moles per gram of paint lower by a factor of 0.341. The number of neutron absorption barns per mole, however, increased by a factor of 31.6.

Element	Symbol	Mass Fraction	Mol Fraction	Thermal n Absorption (b)
Gadolinium	Gd	2.30E-6	3.26E-7	4.90E+4
Cadmium	Cd	1.90E-6	1.06E-6	2.45E+3
Halfnium	Hf	7.30E-4	9.11E-5	1.04E+2
Cobalt	Co	2.80E-2	1.06E-2	3.72E+1
Titainium	Ti	2.30E-1	1.07E-1	6.09E+0
Oxygen	O	1.54E-1	2.14E-1	1.90E-4
Copper	Cu	3.30E-2	1.16E-2	3.78E+0
Carbon	C	2.00E-1	3.70E-1	3.50E-3
Hydrogen	H	1.05E-3	2.31E-2	3.33E-1
Chlorine	Cl	2.58E-1	1.62E-1	3.55E+1
Nitrogen	N	5.82E-2	9.25E-2	1.91E+0
Samarium	Sm	2.50E-6	3.70E-7	Not in simulation
Europium	Eu	1.30E-7	1.91E-8	Not in simulation
Dysprosium	Dy	2.10E-6	2.88E-7	Not in simulation
Indium	In	6.90E-8	1.34E-8	Not in simulation
Erbium	Er	1.10E-6	1.47E-7	Not in simulation
Thulium	Tm	1.60E-7	2.11E-8	Not in simulation
Lutetium	Lu	1.40E-7	1.78E-8	Not in simulation
Barium	Ba	1.30E-4	2.11E-5	Not in simulation
Zinc	Zn	2.90E-4	9.88E-5	Not in simulation
Tin	Sn	2.90E-3	5.44E-4	Not in simulation
Zirconium	Zr	3.50E-2	8.55E-3	1.84E-1
Element	Symbol	Mass Fraction	Mol Fraction	Thermal n Absorption (b)
Carbon	C	0.65	0.41	3.50E-3
Hydrogen	H	0.06	0.47	3.33E-1
Oxygen	O	0.22	0.11	1.90E-4
Titanium	Ti	0.07	0.01	6.09E+0

TABLE 3.1: Quantities of elements included in simulation of the paint based on ICP-MS results and on common green and white dyes (top) and quantities of elements previously included in the paint (bottom). Average atomic mass is 22.28 (bottom: 7.6), with an average neutron capture cross section of 7.05 barns (bottom: 0.22). After disregarding some elements due to their small concentrations and cross sections, all elements included in the new simulation make up 99.7% of the total mass, down from 100.03% for all elements listed.

Altogether, this results in a factor of 0.7 change in the neutron absorption barns in the paint.

Assuming that the paint's only contribution to the detector behavior is the absorption of neutrons, the removal of the new paint layer from the simulation could be expected to add 1.34 ± 0.23 percent (absolute) to the neutron detector efficiency, based on the number

of capture barns removed relative to the old paint. However, when the detector was simulated with and without the new paint, the efficiency increase with the paint removal was only 0.29 ± 0.21 percentage points. This suggests that capturing neutrons was only a minor component of the effects that the old paint had on the detection efficiency.

A possible cause of the large efficiency cost with the previously simulated paint could be its thermalization of neutrons. With 47% of the old paint being composed of hydrogen, it would have a much greater ability to thermalize neutrons than the new paint composition. Neutrons thermalized in paint would have farther to travel before reaching the neutron counters than they would have if they had been thermalized in the plastic tubes surrounding the counters. This longer path would involve a higher chance of a neutron being capture on lead or steel, as they would be thermalized outside of the steel rings and sometimes on the outside of the lead blocks.

3.2 Effects of Geometry Modifications

With neutrons simulated with starting energies of 434 keV (total energy 940 MeV) at random locations in the lead matrix, the detector efficiency (at revision 76) was found to be (32.55 ± 0.15) %. Subsequent revisions were compared to this efficiency for 434 keV neutrons.

3.2.1 Counter Length Adjustment

When the geometries in the simulation were reviewed, the neutron counter lengths were found to be too long. At revision 80, the counter lengths were reduced by $1\,\mathrm{cm}$ for all of the neutron detectors. As most the neutron detectors are 3 meters long, this is only slightly more than a 0.33% reduction in ^{3}He volume.

Spallation events (§5.2.2) in the detector have indicated a position RMS of detected neutrons in a point neutron burst is about 50 cm (Table 5.3). This is much smaller than the bulk of the detector, so the front and back of the detector could expect neutron fluxes at levels around half of the flux found in the central plane where neutrons can come from both sides. This weights the length at the end of the counters less than the centers for

determining detection efficiency for neutrons from the lead, giving an expected efficiency reduction of just over 0.05 percentage points. For revision 80, an efficiency of ϵ = $(32.227 \pm 0.148)\%$ ($\Delta\epsilon$ from 76: $(-0.327 \pm 0.210)\%$) was found. This is not strongly inconsistent with the small reduction in efficiency that was expected.

3.2.2 Lead Mass Adjustment

In revision 82, the size of the lead blocks was increased by almost 1 mm on all surfaces to fill in the space left by the shrinking of the paint layer. This change in volume was allowed because the previous lead dimensions in the simulations were unverified, and would later be checked and fixed [38]. This increased the volume of lead by 4.9%.

Lead has about 12.3% of the total neutron absorption mole barns in the detector [41]. Adding 4.9% more lead will decrease the share of the absorption mole barns held by ^{3}He by 0.6%, suggesting an efficiency drop of 0.19 percentage points. This number could be deviated from significantly, however, due to self-shielding in the ^{3}He counters or higher fluxes of thermal neutrons near the plastic moderator surrounding the tubes.

For revision 82 an efficiency of ϵ = $(32.335 \pm 0.148)\%$ ($\Delta\epsilon$ from 80: $(0.108 \pm 0.210)\%$) was found. This is slightly different from the expected drop in efficiency but not significantly so.

3.2.3 Removal of Graphite Reflector

The optional component of a graphite neutron reflector around HALO which is not currently included in the physical detector was found to be included in the previous versions of the simulation. In revision 91, this was removed. In this same set of updates an extra steel structure on the side of the detector was also removed.

Revision 91 had an efficiency of ϵ = $(29.06 \pm 0.454)\%$ ($\Delta\epsilon$ from 82: $(-3.05 \pm 0.447)\%$) was found. A large efficiency drop was expected with the removal of the reflector. With a central efficiency close to 45% and an average efficiency close to 30%, the walls of the detector were responsible for the losses of about a third of the created neutrons. This

suggests that the graphite was about 20 percent (absolute) more likely than the water and steel frame to reflect neutrons back to the detector.

3.2.4 ^{252}Cf Neutron Capture Efficiency

The energy of simulated neutrons has a small effect on their detection efficiency, since the neutrons must be thermalized before detection.

The ^{252}Cf neutron energy distribution has a mean close to 2.2 MeV, but extends past 10 MeV, including some neutrons with sufficient energy to undergo (n,2n) reactions in lead. While measuring the efficiency gradient (§3.2.6) it was found that $(0.108 \pm 0.005)\%$ of simulated neutrons produce an additional neutron.

Neutrons with energies from the ^{252}Cf Spontaneous Fission (SF) energy distribution were also simulated throughout the detector in revision 91. This resulted in an efficiency of ϵ = $(25.89 \pm 0.438)\%$ ($\Delta\epsilon$ from 434 keV: $(-3.17 \pm 0.631)\%$). Higher energy neutrons need more collisions to get to a thermal energy range, giving them a longer drift distance and hence a higher probability of exiting the detector, so an efficiency drop was expected.

3.2.5 List of Geometry Changes

A summary of the efficiency changes from the above geometry modifications can be found in Table 3.2.

Rev#	Geometry change	Efficiency change
76	Paint composition and mass changed	$(1.62 \pm 0.39)\%$
80	Neutron counters shortened by 1 cm	$(-0.327 \pm 0.210)\%$
82	Lead mass increased 4.9%	$(0.108 \pm 0.210)\%$
91	Removal of graphite reflector	$(-3.05 \pm 0.45)\%$
91	Average Neutron energy changed from 434 keV to 2.2 MeV	$(-3.71 \pm 0.63)\%$

TABLE 3.2: Efficiency changes from simulation modifications for neutrons simulated uniformly throughout the lead volume. The final efficiency with the ^{252}Cf SF spectrum in revision 91 was $(25.89 \pm 0.44)\%$.

3.2.6 Efficiency Gradient

Calibration tubes in HALO are placed into gaps noticeably larger than the size required for the tubes, and the lead structure has small irregularities in the lining up of the blocks, on the order of 1 cm. This makes it difficult to pinpoint the location of a calibration source with more than 1 cm precision. To see if better precision is necessary, efficiency gradients were examined around a calibration tube position.

Neutrons were simulated at the center of calibration tube 33-10, at (x,y,z) = (-16.81,-17.47,0.00) cm, with (0,0,0) defined as the center of the detector. Three more points were simulated, with a 3 cm increment in x, y, and z directions respectively. Neutrons were given energies from the ^{252}Cf SF neutron energy distribution.

The resulting efficiency was 47.57 ± 0.16 %, with a gradient of (-0.037 ± 0.074 , 0.150 ± 0.074 , 0.011 ± 0.074) %/cm. The only indication of a non-zero component is the y direction, and is still slightly smaller than expected statistical errors if displacements are confined to 1 cm. The detector is mostly symmetric in the y direction around this tube, and the gradient over all is not inconsistent with the zero vector. Position errors do not seem to present a significant problem and are neglected in the calibration.

Chapter 4

Neutron Detection Calibration

The accuracy of the simulation's results required verification. This was done with a neutron source primarily composed of ^{252}Cf at 192 locations throughout the detector. The observed neutron multiplicities at each of these points was compared to the known neutron multiplicity [42] to determine the detection efficiency for neutrons.

4.1 Voltage Adjustments

Before calibrating for neutron detection efficiency, the voltages applied to the ^{3}He counters were adjusted to make the neutron detection regions of interest line up [43].

Neutron captures on ^{3}He have a peak at 764 keV. The peak bin for each channel was measured by placing the calibration source at the center of each bore for 9 minutes. The energy spectrum was then fit with a function which mimics the shape of the neutron energy deposition distribution:

$$f(x) = \begin{cases} a + b * e^{-\frac{1}{2}(\frac{x-c}{d})^2} + je^{gx}, & \text{if } x \leq c \\ h + (a + b + je^{gc})e^{-\frac{1}{2}(\frac{x-c}{k})^2}, & \text{if } x > c \end{cases} \tag{4.1}$$

Where c is the peak position. This was applied one channel at a time to data collected in the 9 minute run with the source in the bore corresponding to the counted channel. For 9 minutes of source data this method was found to have an error of about 2.9 bins by observing results of the fit on a series of runs with an AmBe source.

Adjusting the voltages in the test stand channels from $1700\,\mathrm{V}$ to $1670\,\mathrm{V}$ and observing the resting change in peak position gave a value of $\frac{d}{dV}\ln(P) = 0.0054 \pm 0.0001$, where P is the peak channel. Each channel was then adjusted in voltage by a value of $\frac{\overline{\ln(P)} - \ln(P)}{\frac{d}{dV}\ln(P)}$. Over all channels this value was $0 \pm 5.2\,\mathrm{V}$. The central ADC value the peaks were adjusted to was 1223 for neutrons from the ^{252}Cf source.

4.2 Calibration Runs

The front face of HALO is fitted with 40 calibration tubes, but only 24 of these can be accessed with the detector 'closed' (front shielding wall in place). These 24 tubes are roughly arranged in rows of 4 tubes, as can be seen in Figure 2.7.

4.2.1 Tube Locations

The depth of the lead is 307.5 cm. The tubes extend to the back of the lead where they are capped by steel plates flush with the back of the lead blocks. The source capsule has 5.4 cm of length ahead of the engraved line used to mark the location of the source. With the center of the lead assigned the position $z = 0$, the furthest back position attainable is $z = -148.4\,\mathrm{cm}$. A fiberglass rod was attached to the source and inserted into a tube until it stopped, and marks were drawn on the rod at the point where it emerged from the calibration tube. These marks were found to have less than 1 cm in deviation between tubes for all 40 tubes. The center of these spots was marked, and the other locations in z were marked by measuring from the back location along the rod.

The locations of the calibration tubes accessible with the detector closed nearly form a four by six grid in x and y (Figure 4.1). Five distances in z were chosen for each tube to have a comparable resolution. These were the center ($z = 0$), $z = \pm 60\,\mathrm{cm}$, and $z = \pm 120\,\mathrm{cm}$.

To see the effects of the shielding more clearly and examine discrepancies near the center of the detector, 9 tubes were chosen to have measurements taken in 13 locations. These were chosen to be tubes on the corners, sides, and one in the center, specifically CT-61-11, CT-62-1, CT-64-11, CT-44-11, CT-31-2, CT-33-10, CT-11-2, CT-13-10, and CT-14-2

(Figure 4.1). The locations in z for these tubes were $z = 0$, $z = \pm 30\,\text{cm}$, $z = \pm 60\,\text{cm}$, $z = \pm 90\,\text{cm}$, $z = \pm 120\,\text{cm}$, $z = \pm 135\,\text{cm}$ and $z = \pm 148.4\,\text{cm}$ (Figure 4.2).

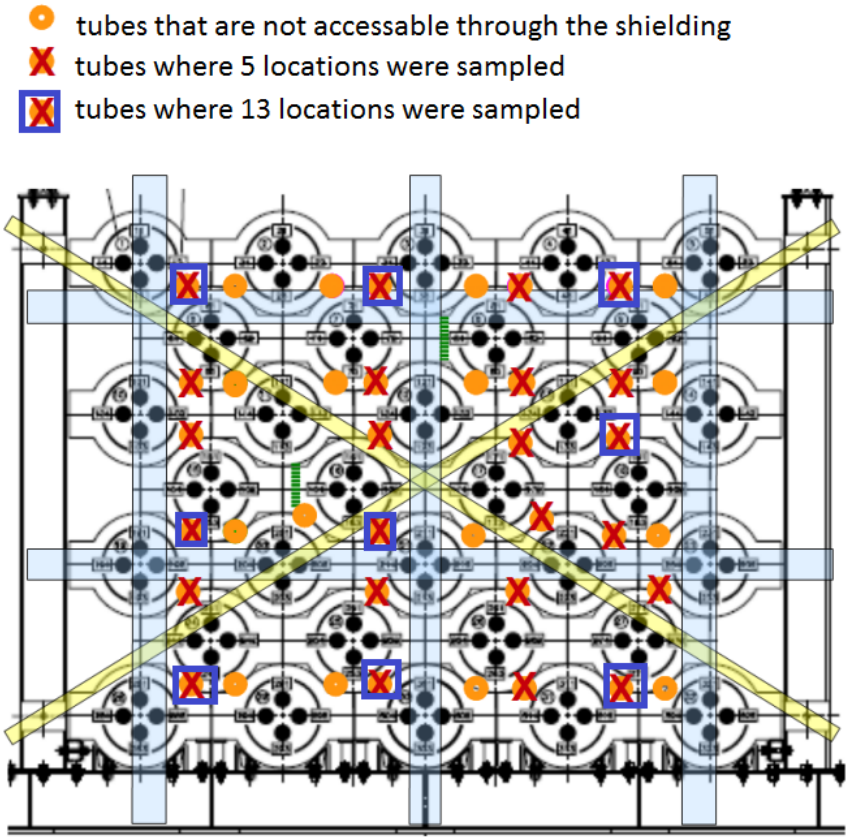

FIGURE 4.1: Sampling of calibration points in the detector

4.2.2 Run Times

To plan the required run times, simulations were run with different efficiencies and numbers of fissions (Table 4.1). These simulated runs used the ^{252}Cf multiplicity distribution from Table 4.2, and each run was analyzed for efficiency and number of fissions with no constraints. This resulted in an error of $\frac{0.39}{\sqrt{n_f}}$ for all efficiencies, where n_f is the number of fissions in the run.

At each point, the calibration source is placed for 11 minutes to achieve an error in ϵ close to 0.003. This time would have allowed for the 192 runs to fit nicely in 5 underground shifts, but completing the installation of the front shielding took up part of the

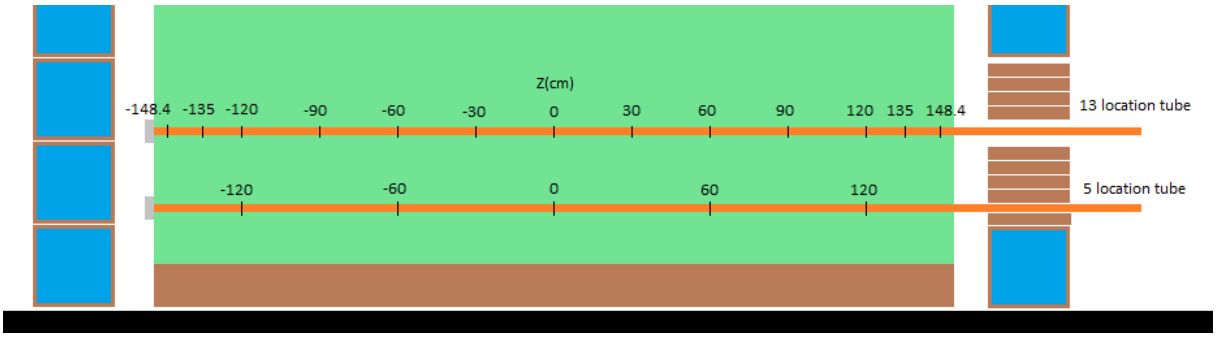

FIGURE 4.2: Depths sampled in Z in the detector

Configuration	ϵ	n_f	$\Delta\epsilon$
1	0.1370	1000	0.01165
1	0.1353	3000	0.00702
1	0.1421	9000	0.00432
2	0.3627	3000	0.00715
3	0.4858	3000	0.00739
3	0.4800	9000	0.00414

TABLE 4.1: Simulations to determine precision of parameters from neutron fit. Configuration 1 is fissions in the center of bore 21 with neutron counter only in bore 21. Configuration 2 is fissions in the center of bore 21 with neutron counters in the whole detector. Configuration 3 is fissions in the center of the detector with neutron counters in the whole detector. Error in capture efficiency from the multiplicity fit with no fission rate information seems to be about $\frac{0.39}{\sqrt{n_f}}$.

first shift, extending the calibration runs to 6 shifts. These runs were performed in 2016 on April 19, 20, 21, 22, 25, and 26.

4.3 Neutron Multiplicity Metric

^{252}Cf has a known multiplicity distribution, shown in Table 4.2. Knowledge of this distribution is necessary to accurately calculate the efficiency and fission rate of the source simultaneously, and can also be used to reduce statistical errors.

With a very high neutron multiplicity, it would be possible to count the number of bursts that occur during a calibration run. If this high multiplicity was fixed, it would allow for the number of neutrons produced in the run to be known and not assumed

Multiplicity	Probability	Error
0	0.0021	0.0001
1	0.0260	0.0003
2	0.1267	0.0005
3	0.2734	0.0008
4	0.3039	0.0010
5	0.1848	0.0007
6	0.0657	0.0006
7	0.0154	0.0003
8	0.0020	0.0002

TABLE 4.2: Neutron Multiplicity of ^{252}Cf SF. Average multiplicity: 3.75718 [42]

from the run time and source strength, resulting in an improvement factor in measuring detection efficiency ϵ of $\sqrt{1-\epsilon}$ as statistics are switched from Poisson to Binomial.

In reality spontaneous fission results in a distribution of produced neutrons, so the total number of neutrons produced in a calibration run is not perfectly known. However, if the standard deviation of the neutron multiplicity is less than the square root of that multiplicity, then a fission count still provides better precision on the number of neutrons produced than any prior measurement of the source strength could. This is the case for ^{252}Cf, with a multiplicity for a single fission of 3.75718 with an RMS of 1.27 (Table 4.2).

Simulations had placed the lead volume-averaged neutron capture efficiency around 30%, with the central neutron capture efficiency close to 50%. This suggests that almost all of the detector locations will see a majority of the fissions produced there, putting some constraint on the statistical error of the efficiency calibration. For these reasons a multiplicity fit will be used to determine the neutron capture efficiency.

4.3.1 Multiplicity Fit Method

To first order, a sum of binomials for each possible SF multiplicity produced would accurately model the data. However, some corrections need to be made for various effects that further modify the multiplicity distribution. Fits with the following corrections are shown in Figure 4.4.

Pileup

A time window of 1.5 ms was used to look for coincidences (this was later increased to 2 ms (§4.4.3)). If two fissions occurred within this time window, their multiplicity would be combined, modifying the distribution. When scanning for neutron multiplicity, any neutron less than 1.5 ms after another will be added to the same burst as the previous neutron even if the initial neutron in that burst was counted more than 1.5 ms ago. This prevents the neutrons from one fission from being split between two events, as the neutrons created in a fission will always be within the 1.5 ms time window of each other, causing them to be fully separated from or fully combined with other fissions.

With n_f fissions in a run, there are $n_f - 1 \approx n_f$ time gaps between fissions. The duration of these time gaps will follow the exponential distribution with $pdf = \frac{n_f}{T} \times exp(-\frac{n_f t}{T})$. With n_f fissions in time T, the probability that any given gap is less than time window W in duration is then $P_{pile} = 1 - exp(-\frac{n_f W}{T})$. To first order this results in $n_f(1 - 2P_{pile})$ single fissions and $n_f P_{pile}$ double fissions.

To add the next order of pileup, the distribution of the short time gaps is considered. After any short time gap, there is a probability of P_{pile} that the next time gap is also short. This results in $n_f(P_{pile})^2$ triple fissions. Moving two short time windows together removes two double fissions, so double fission events are then reduced to $n_f(P_{pile} - 2(P_{pile})^2)$, and single events increased to $n_f(1 - 2P_{pile} + P_{pile}^2)$.

This results in a detected number of multiplicity i bursts $N(i)$ that uses a neutron multiplicity distribution $M(j)$, the probability of an event having real neutron multiplicity j:

$$N(i) = n_f \sum_{j=0}^{24} \frac{j!}{(j-i)!i!} \epsilon^i (1-\epsilon)^{j-i} M(j) \tag{4.2}$$

where $M(j)$ is defined with

$$M(j) = e^{-2\frac{n_f W}{T}} p(j) + (-1 + 3e^{-\frac{n_f W}{T}} - 2e^{-2\frac{n_f W}{T}}) pp(j) + (1 - e^{-\frac{n_f W}{T}})^2 ppp(j) \tag{4.3}$$

Where $p(j)$ is line j from Table 4.2, $pp(j) = \sum_{k=0}^{8} p(k) * p(j-k)$ and $ppp(j) = \sum_{k=0}^{16} pp(k) * p(j-k)$.

Busy Channels

When a count is detected in HALO, its energy is recorded in a channel on a shaper card. It is not read and assigned a time stamp until the single board computer (SBC) in its crate polls the card, not more than 73 μs later, as seen in Figure 4.3. Until this time, the channel that detected a count is busy and cannot detect more counts [44]. This delay during which the channel is inactive is similar to the neutron capture time, and effectively reduces the capture efficiency for all neutrons after the first in a fission to a new efficiency ϵ'.

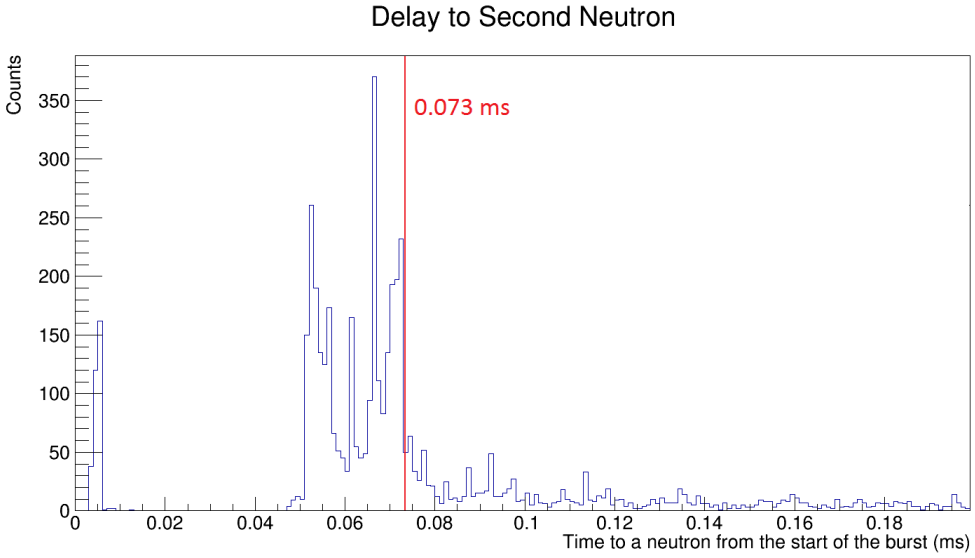

FIGURE 4.3: Delay between the first and second neutrons from a calibration run in the center of the detector, when both neutrons were processed in the same crate. The peak around 5μs is caused by counts from a second neutron in the same card as the first neutron that arrived before the first card was finished polling. The peaks around 70 μs are caused by a second neutron captured in a different card than the first neutron. After the peaks a periodic effect can be seen due to the 20μs polling cycle when all channels are empty.

For a group of $k+1$ neutrons, the probability that there are k undetected neutrons before a detected neutron is $(1-\epsilon)^k\epsilon$. The remaining neutrons from the fission follow a binomial distribution with capture efficiency ϵ'. These can be combined as follows, replacing Equation 4.2:

$$N(i) = n_f \sum_{j=0}^{24} \sum_{k=0}^{j-i} \binom{j-k-1}{i-1} \epsilon \epsilon'^{i-1} (1-\epsilon)^k (1-\epsilon')^{j-k-1} M(j) \tag{4.4}$$

The value of ϵ' can be calculated from metrics other than the neutron multiplicity. If the probability that two otherwise detected neutrons from a fission arrive at the same channel is L_r and the probability that the delay between detected neutrons is less than the readout time is L_t, then

$$\frac{\epsilon'}{\epsilon} = (1 - L_t L_r). \tag{4.5}$$

To determine L_r, the first neutron detected in each burst is selected as it cannot be missed due to a busy channel. If a_i neutrons detected first in their fission are detected in channel i and a neutrons that are first in their fission are seen in total, then the probability of a neutron landing in channel i is $\frac{a_i}{a}$. When a neutron has landed in channel i, there is again a probability of $\frac{a_i}{a}$ of the next neutron also landing in channel i. L_r is then the probability weighted average of the probability of a second neutron landing in the same channel:

$$L_r = \sum_i (\frac{a_i}{a})^2 \tag{4.6}$$

$$\Delta L_r = 2\sqrt{\sum_i \frac{a_i^3}{a^4}} \tag{4.7}$$

L_t can be independently determined with the subsequent count in each fission. The two crates have separate clocks, so only subsequent neutron counts from the same crate as the primary neutron are included in the calculation so as to avoid time-stamp errors. If k is the number of second counts in all bursts that occur within the busy channel time of the first count and n is the number of second counts that occur in total, then L_t and $\frac{\epsilon'}{\epsilon}$ can be calculated as follows. Here, k and $n-k$ are the independent parameters.

$$L_t = \frac{k}{k + (n-k)(1-L_r)} \tag{4.8}$$

$$\Delta\frac{\epsilon'}{\epsilon} = \Delta(1 - L_t L_r) = \frac{\sqrt{L_r^2(1-L_r)^2 nk(n-k) + n^2k^2(\delta L_r)^2}}{(k + (n-k)(1-L_r))^2} \tag{4.9}$$

Background

When lowering the ADC threshold to channel 280 (177 keV) to see all neutrons in the calibration, HALO has a background rate of 0.0329 Hz with all shielding in place. This count rate is included in the multiplicity one bin only, as this rate is too low to have notable pileup effects.

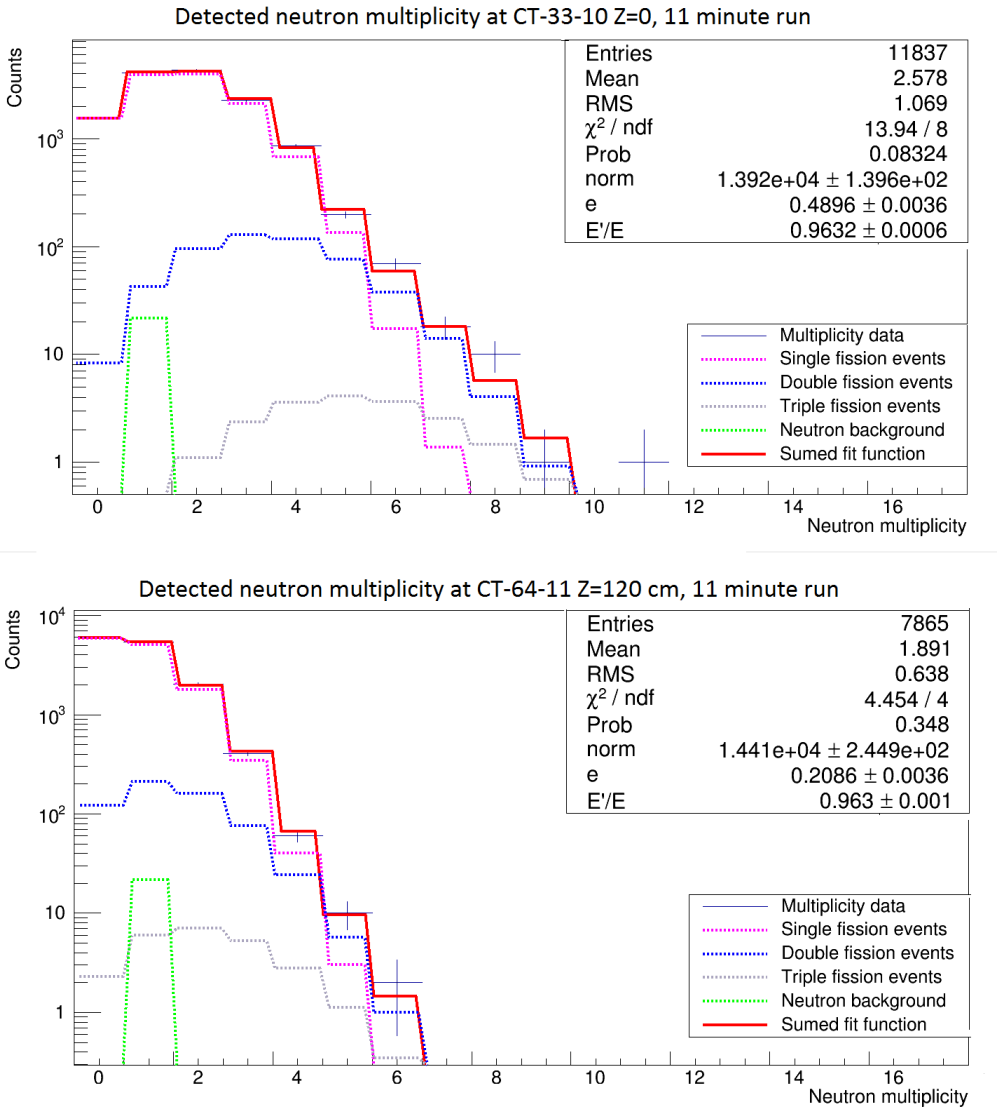

FIGURE 4.4: Neutron multiplicity fits with Equation 4.4 for CT-33-10 z=0 (top), and CT-64-11 z=120cm (bottom). 'e' is the neutron detection efficiency found in the multiplicity fit, 'norm' is the number of fissions found in the multiplicity fit, E'/E is the relative reduction in efficiency for late neutrons, controlled to $(1 - L_r L_t)$ (Equation 4.5).

4.3.2 Source Strength Decay

The half-life of ^{252}Cf has been measured to be 2.645 years. However, the neutron rate from Californium neutron sources does not exactly follow this decay curve (Figure 4.5). Other contributions to SF rate can come from traces of ^{250}Cf created during the production of the source and from ^{248}Cm created by alpha decay of ^{252}Cf [45].

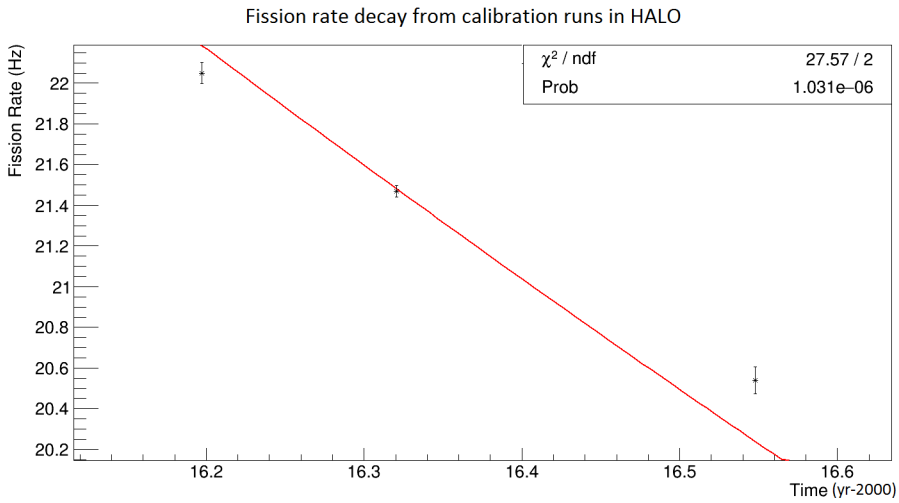

FIGURE 4.5: Measured fission rates do not appear to follow the ^{252}Cf decay curve (fit on graph). This can be explained by the presence of other isotopes (§4.4.3).

The total neutron rate Q then scales with time like

$$Q = Re^{-\lambda_{252}t} + Se^{-\lambda_{250}t} + T(1 - e^{-\lambda_{252}t}) \tag{4.10}$$

Where R is the initial neutron rate from ^{252}Cf, S is the initial rate from ^{250}Cf, and T is the neutron rate from ^{248}Cm that would be present if all the ^{252}Cf decayed. The half life of ^{248}Cm is long so it assumed to not deplete over the time scale of the HALO experiment.

Because the ^{248}Cm fissions depend on ^{252}Cf decay, T can be found as a function of R, as well as the decay rates (λ), the SF branching ratios B_{SF}, and the mean neutron multiplicity $\bar{\nu}$:

$$T = \frac{\lambda_{248} B_{SF248} \bar{\nu}_{248}}{\lambda_{252} B_{SF252} \bar{\nu}_{252}} (1 - B_{SF252}) R = CR \tag{4.11}$$

From Table 4.3 it can be found that $C = 1.654 * 10^{-5}$. This leaves two parameters, R and S, to describe the neutron emission rate at any time.

Parameter	^{252}Cf	^{250}Cf	^{248}Cm
$\lambda(yr^{-1})$	0.262	0.0530	$1.99 * 10^{-6}$
B_{SF}	0.0309	0.00077	0.0839
$\bar{\nu}$	3.75718	3.53	3.11

TABLE 4.3: Decay parameters of neutron emitting isotopes in the neutron source

To examine the effect of the lower multiplicities of the trace isotopes in the Cf source, a multiplicity distribution was made for ^{250}Cf by scaling all multiplicities from ^{252}Cf by the ratios in average multiplicity, and then splitting the probabilities between their floor and ceiling of the multiplicity by the multiplicity modulo 1. This created a distribution similar to the distribution for ^{250}Cf when measured directly [46]. This multiplicity distribution was used to generate simulated ^{250}Cf fissions, which were compared to ^{252}Cf fission with a fit using the ^{252}Cf multiplicity distribution.

100000 ^{252}Cf fissions and 92615 ^{250}Cf fissions were simulated. They were analyzed separately as well as mixed together (Table 4.4).

^{250}Cf fissions per fission	Fit efficiency	Fit n_f - fissions (σ)
0	0.4717 ± 0.0012	0.22
0.48	0.4585 ± 0.0009	1.16
1	0.4432 ± 0.0013	0.57

TABLE 4.4: Response of fit assuming ^{252}Cf neutron multiplicity to simulated ^{250}Cf fission fraction. The fit efficiency seems to scale linearly with average multiplicity, with no effect on the fit number of fissions. The response was fit to get the line $\epsilon = (0.4583 \pm 0.0006) - (0.0285 \pm 0.0017)(f - 0.48)$, where $f = ^{250}$Cf fissions per fission

Because the fit fission rate does not change significantly with the change in multiplicity, the calibration runs used only to analyze fission rate are still used with the fit using only the ^{252}Cf neutron multiplicity. In the 192 runs used to determine the efficiency of the detector, the multiplicity used is a combination of the ^{252}Cf, ^{250}Cf, and ^{248}Cm neutron multiplicities based on their concentrations found by fitting for the decay parameters (Table 4.8).

4.3.3 Advantages

The multiplicity fit method of neutron calibration allows fission rate data and efficiency data to be simultaneously extracted from the same detector. In HALO's case, this is essential, as the source strength measurement was too long ago to accurately predict the source strength without another data point to determine the initial ^{250}Cf content.

After the source strength is well determined by calibration, the multiplicity fit can still be useful in determining the neutron detection efficiency. With no multiplicity fit, the counting errors from ^{252}Cf SF can be calculated as follows:

$$\Delta\epsilon_{count} = \frac{\sqrt{\sum_{k=0}^{24} k^2 \sum_{j=k}^{24} \binom{j}{k} E^k (1-E)^{j-k} M(j)}}{3.75718\sqrt{n_f}} \tag{4.12}$$

As shown in Figure 4.6, when given a fixed fission rate, the neutron detection efficiency error from the fit traces the counting error for ^{252}Cf for low efficiencies, and creates smaller errors in locations with efficiencies greater than 20%.

These errors are calculated using fits with shared fission rate information and fits with no shared information. First the fission rate and fission rate error as a function of time are found with unconstrained multiplicity fits on the 192 points in the closed detector calibration as well as three other days of calibration. Then the 192 points of the closed calibration are run again with the previously detected fission rate fixed in each fit to attain the inherent error $\Delta\epsilon_1$.

The correlation from the original unconstrained fit ρ_{ϵ,n_f} (Figure 4.7) is used to find the coefficient of determination $R^2 = (\rho_{\epsilon,n_f})^2$. This value as well as the original errors from the unconstrained fit, $\Delta\epsilon_0$ and Δn_{f_0}, are used to propagate the finalized error in n_f to an error in ϵ (Figure 4.6):

$$\Delta{\epsilon_0}^2 = \Delta{\epsilon_1}^2 + (\frac{d\epsilon}{dn_f})^2 \Delta n_{f_0}^2 \tag{4.13}$$

$$(\frac{d\epsilon}{dn_f})^2 \Delta n_{f_0}^2 = R^2 \Delta{\epsilon_0}^2 \tag{4.14}$$

$$\Delta\epsilon = \sqrt{\Delta{\epsilon_1}^2 + R^2 \frac{\Delta{\epsilon_0}^2}{\Delta n_{f_0}^2} \Delta{n_f}^2} \tag{4.15}$$

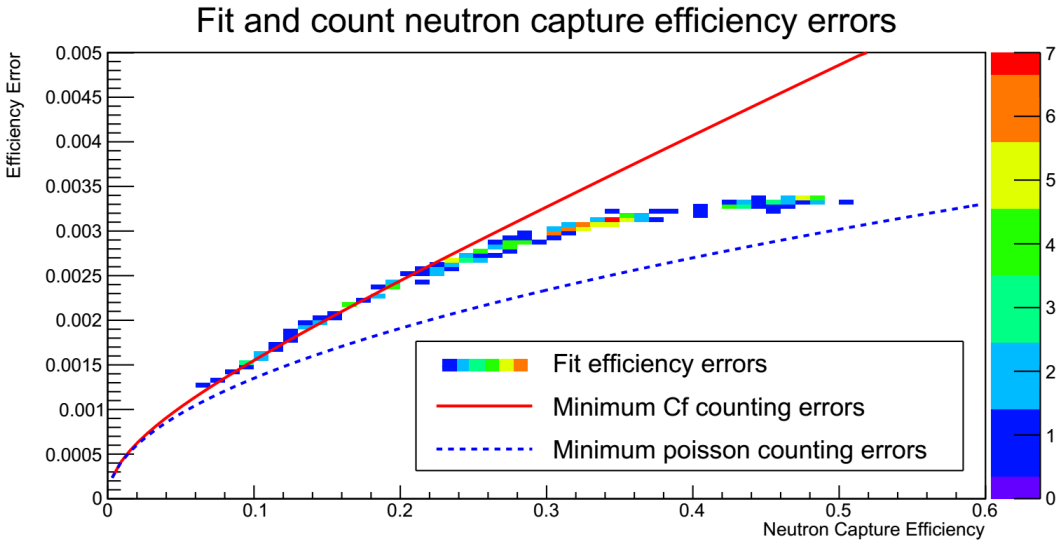

FIGURE 4.6: Error in determining neutron capture efficiency from all 192 calibration points as a function of the capture efficiency found, using the fixed fission rate determined over the whole detector by the multiplicity fit. Errors are calculated by combing the variance of efficiency found with a specified fission rate and the error in the fission rate scaled by the correlation found when fitting with no fission rate constraint (Figure 4.7). The errors from the multiplicity fit are similar to counting errors for low efficiencies and improve at higher ones.

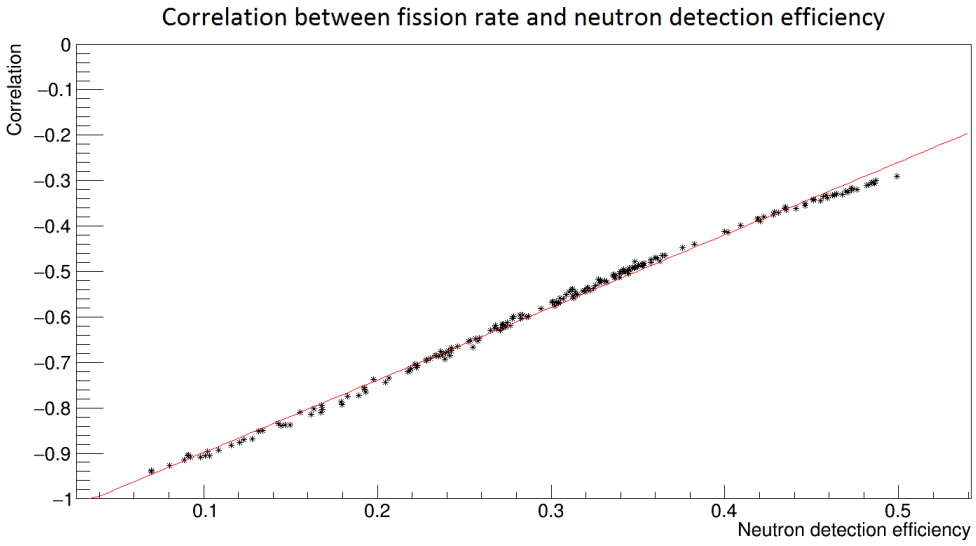

FIGURE 4.7: Correlations of neutron capture efficiency and fission rate from a chi-squared fit with no constraint on the fission rate. The lower magnitude of the correlation in the high efficiency regions of the detector allows the fission rate and neutron capture efficiency to be determined simultaneously. When fit with a straight line, this gives $\rho_{\epsilon,n_f} = -1.06 + 1.60\epsilon$, or $\rho_{\epsilon,n_f} = 1.27(\frac{\arctan(4.62*(\epsilon-0.27))}{\pi} - 0.5)$

4.4 Results

4.4.1 Neutron Capture Time

During the calibration, times between the first neutron and subsequent neutrons detected in the same crate were recorded for verification of the chosen time window, and as a test of the assumed simultaneity of neutrons from spallation events.

Although the probability density function of neutron capture delays cannot be seen clearly below 200 μs due to the Single Board Computer (SBC) polling cycle effects, the total number of neutrons captured earlier can be seen and compared to the integral of the extrapolated timing distribution from the exponential decay found after 200 μs (Figure 4.8). Exponential time distributions were fit in each calibration location with a log likelihood fit from 200 μs to 1500 μs, and individually compared to the counts in the first two polling cycles for each calibration location. If the counts in the first two polling cycles are denoted c_0 and c_1 and the neutron capture rate after delay t is denoted $f(t)$ (fit in Figure 4.8), then the probability P_{short} that a neutron will be captured quickly and separate from

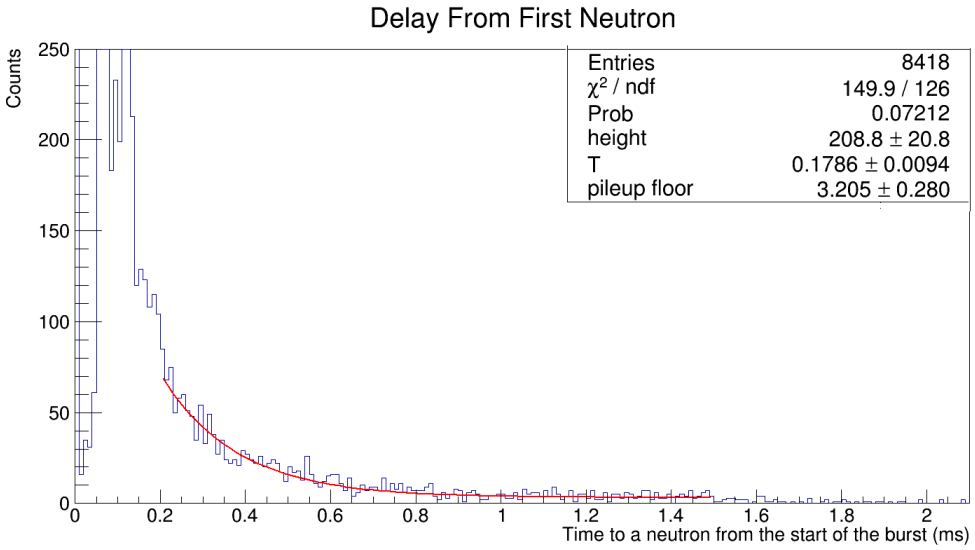

FIGURE 4.8: Times to a neutron from the first neutron in a burst, whenever the subsequent neutron is processed in the same crate as the first. Data from 11 minutes in tube CT-33-10 at z=0. The fit for the decay time starts at 0.2 ms because polling effects disrupt the distribution for shorter times.

the function $f(t)$ can be calculated as

$$P_{short} = \frac{c_0 + c_1 - \int_0^{80\mu s} f(t)\,dt}{n} \tag{4.16}$$

where n is the total number of detected secondary neutrons in the same crate as the primary neutron. A consistent excess was found, with $P_{short} = (36 \pm 4)\%$ (Figure 4.9).

The time distribution of the excess counts cannot be seen directly, but some information can be gained by looking at the ratio of neutrons that arrived on the same card in the same polling cycle (c_0) to the number detected after the next polling cycle (c_1). To be captured in the same polling cycle in the same card, a neutron must arrive in 6 μs or less. The next 73 μs are assumed to result in approximately all of the neutrons captured in the fast method since they have no noticeable spill over into the exponential fit. If the distribution of the excess neutron times is also assumed to be exponential with decay time T_f, then $T_f \approx \frac{6\mu s}{\ln\left(1+\frac{c_0}{c_1}\right)}$. This value is calculated for each point and found to be $(22.5 \pm 2.1)\,\mu$s (Figure 4.10), much shorter than the long decay times T found with the log likelihood exponential fits of $(220 \pm 38)\,\mu$s (Figure 4.11).

With the capture times measured above, we can get some idea of the distance the

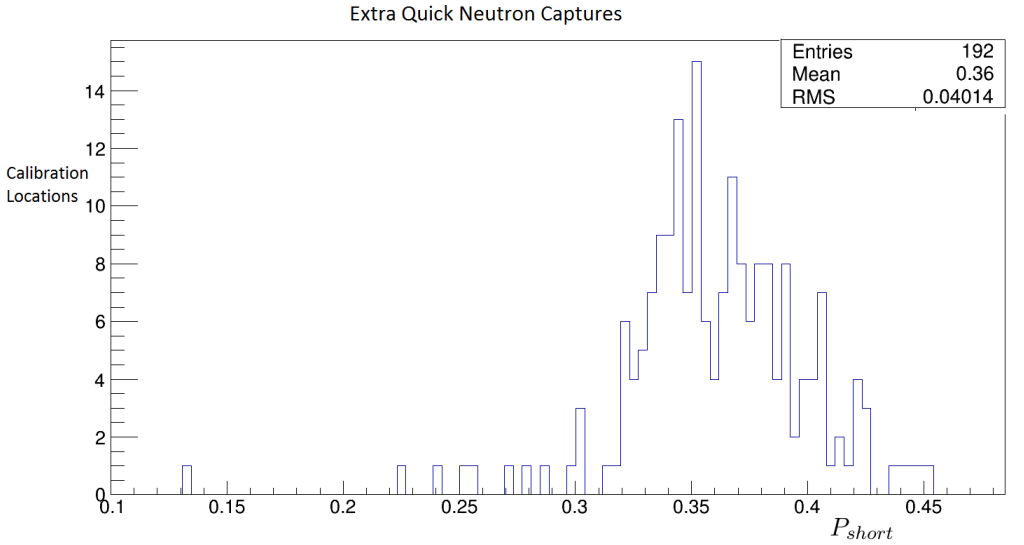

FIGURE 4.9: Histogram with all 192 calibration points of the total number of neutrons with delays < 80μs minus the integral of the exponential function from 0 to 80μs divided by the number of secondary neutrons detected. This shows that a significant fraction of neutrons arrive early compared to the exponential attenuation of neutrons seen in Figure 4.8

neutron traveled after thermalization. Thermal neutrons follow a Maxwell Boltzmann distribution with a mean velocity at 293°K of 2500 $\mathrm{m/s}$. The neutrons are assumed to thermalize almost instantly compared to their capture times. This gives neutron travel distances of 5.6 cm and 55 cm for the short and long capture times.

The shorter distance of 5.6 cm is similar to the distances between counters within one bore. 4 counters with a 5 cm diameter are grouped together separated only by their thin polyethylene sheaths.

The longer neutron travel distance of 55 cm is similar to the distances between bores of 48.7 cm horizontally or 35.5 cm on a diagonal. This could correspond either to neutrons thermalized on the polyethylene in one bore traveling to another, or to neutrons thermalized in lead or water traveling to a bore. This is consistent with the drop in P_{short} seen at low detection efficiencies (Figure 4.12) as the low efficiency regions near the surfaces of the detector have lots of nearby water to thermalize neutrons.

Neutron diffusion distances calculated from capture times cannot be expected in a distribution of neutron detection distance, since neutrons can travel large distances in much shorter times before they are thermalized.

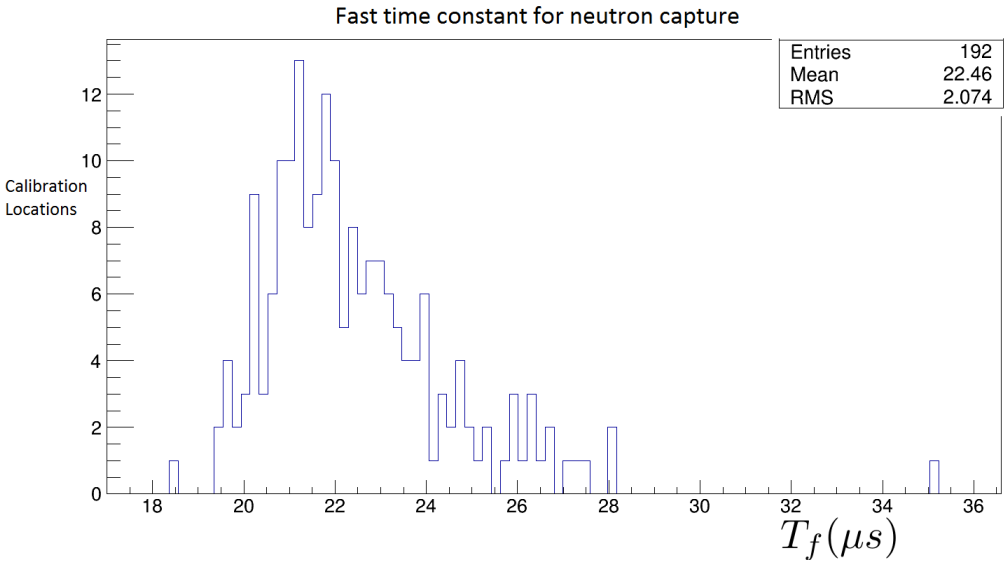

FIGURE 4.10: Neutron capture times from the short (<80μs) region for all 192 calibration locations.

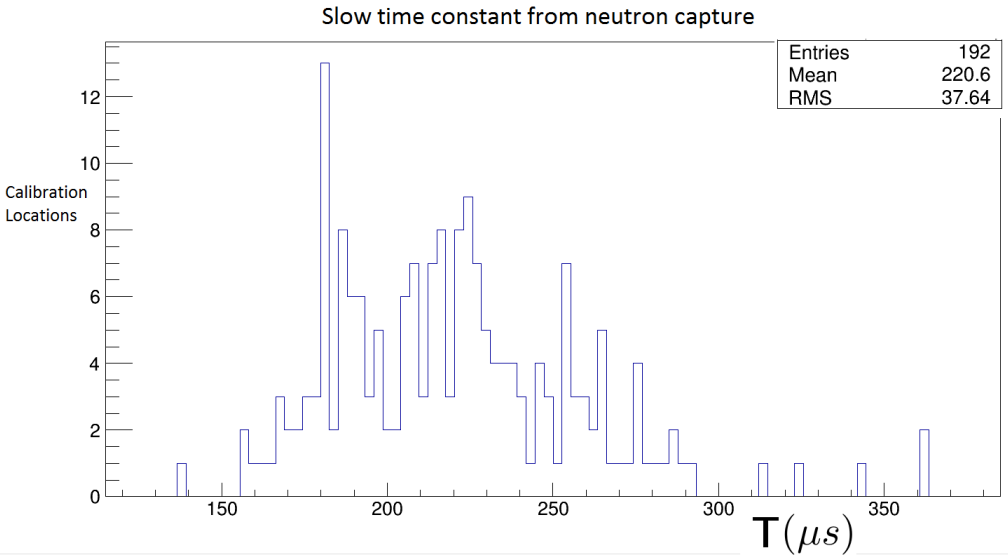

FIGURE 4.11: Neutron capture times from the long (200 to 1500 μs) region for all 192 calibration locations.

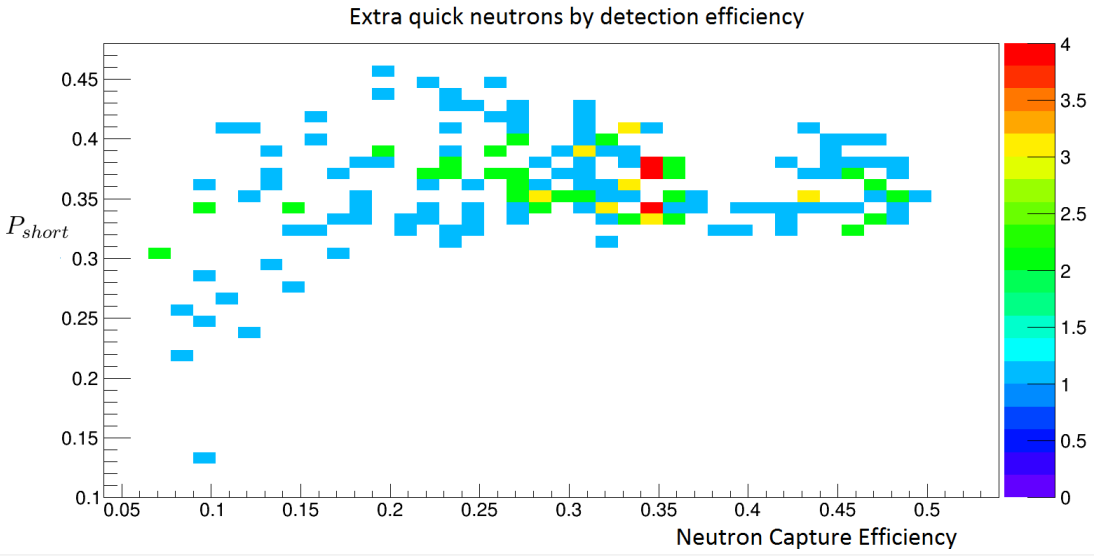

FIGURE 4.12: Distribution of the value of P_{short} as a function of efficiency. Low efficiency regions are closer to water boxes on the outside of the detector, possibly giving them more thermalization locations away from the counters.

4.4.2 Neutron Travel Distance

The distribution of distances from the ^{252}Cf source to the bores where neutrons are detected was plotted from each individual calibration point. This data is clearly inconsistent with any isotropic neutron flux distribution, since neutron detection in tubes at similar distances from the source have significantly different neutron capture rates (Figure 4.13).

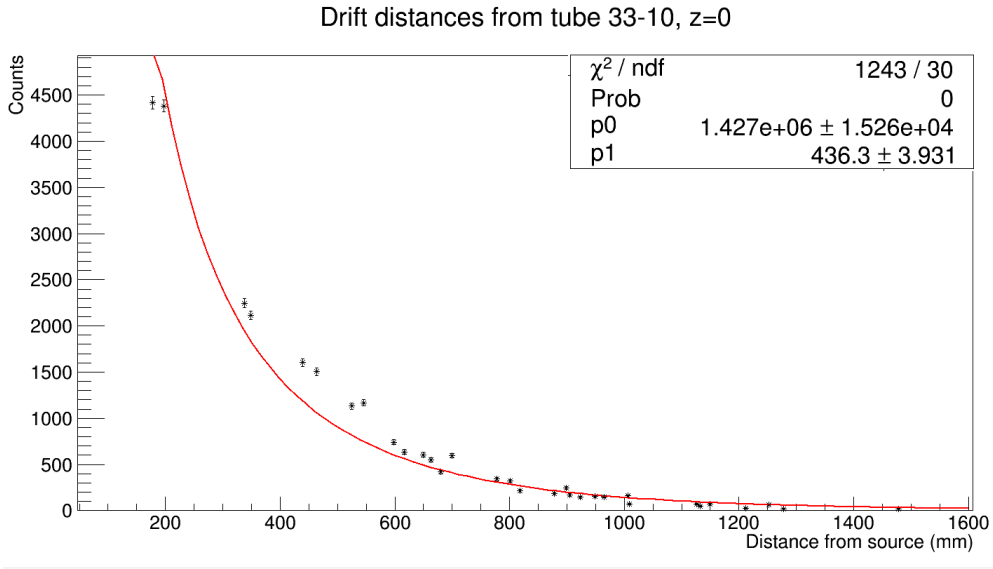

FIGURE 4.13: Neutron travel distance from the ^{252}Cf source to the neutron counters. Data is fit with $\frac{ae^{-r/b}}{r}$, but will not fit well due to thermal neutron diffusion as well as effects of the geometry.

When extracting the attenuation distance R from the fit to $(rate) \propto \frac{e^{-r/R}}{r}$ an average attenuation distance of 425 mm was found (Figure 4.14). This distance is only measured in the xy plane. Assuming similar neutron transport in the z direction, the this suggests a three-dimensional neutron travel coefficient of $425(\sqrt{\frac{3}{2}})\,\mathrm{mm} = 521\,\mathrm{mm}$.

The attenuation distance is plotted over the x, y, and z axis in Figure 4.15. The neutrons appear to travel much further near the front and back of the detector where they have close access to an air pocket.

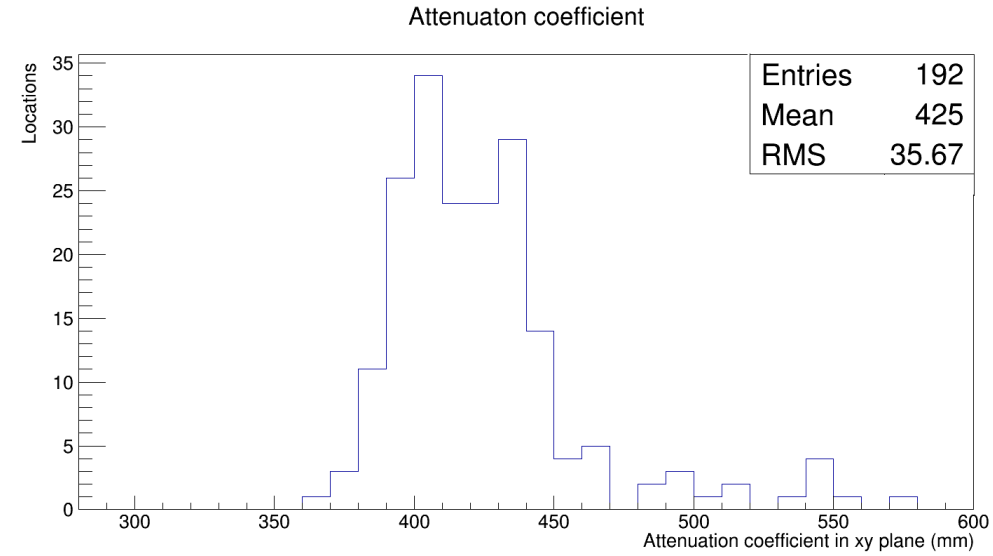

FIGURE 4.14: Neutron attenuation coefficients R in the detector, as fit by $(rate) \propto \frac{e^{-r/R}}{r}$

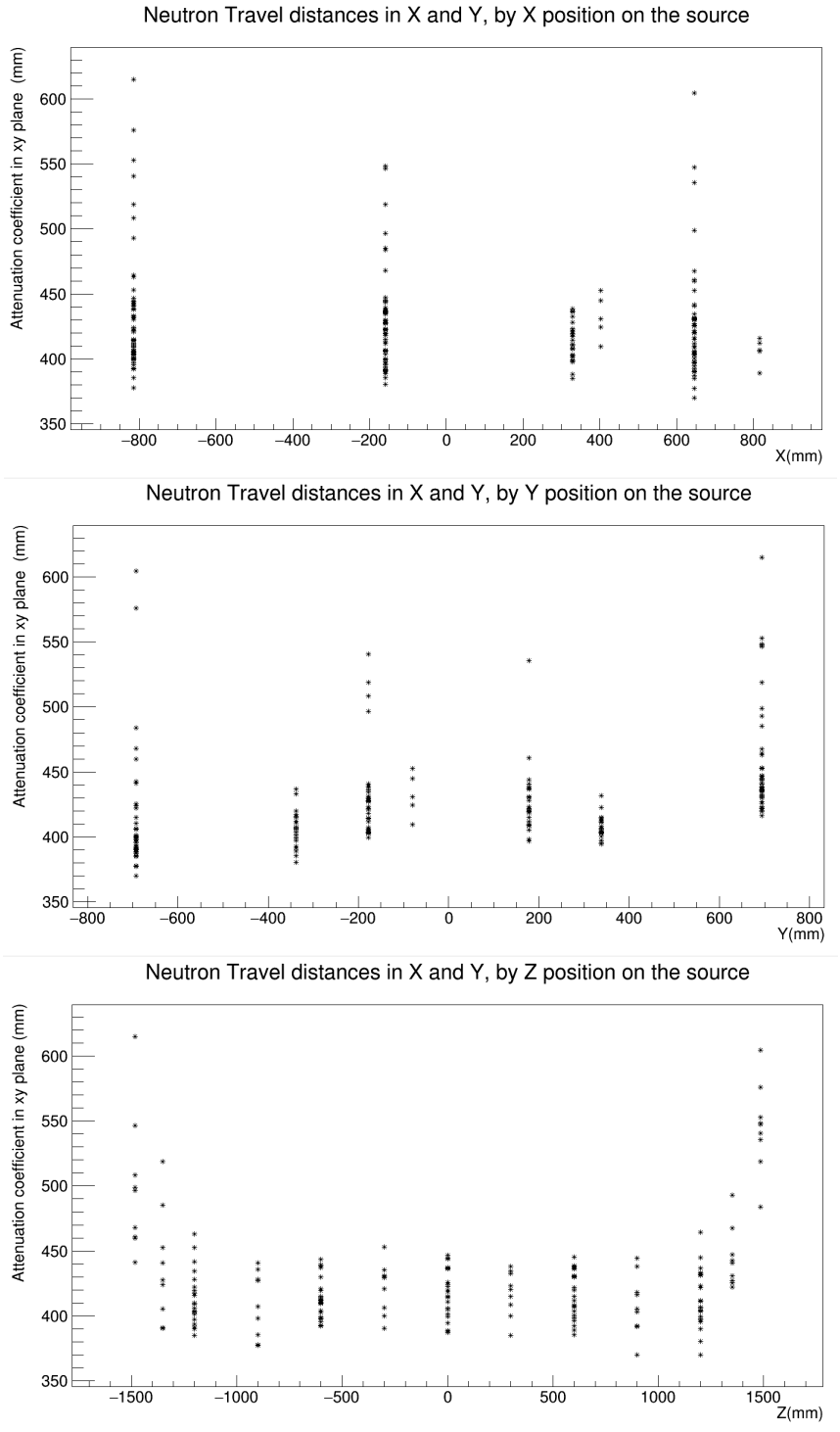

FIGURE 4.15: Neutron attenuation coefficients in the detector as a function of position. The neutron source is allowed to get closest to the edge of the lead in the Z direction, which appears to allow the neutrons to travel much further. There is a large air gap between the edge of the detector and the water on the front, back, and top, which could allow neutrons reflected from the water boxes to travel much further.

4.4.3 Source Strength

To verify the accuracy of the efficiency measurement, the SF rates and composition of the neutron source found by the same methods must be shown to be consistent. With neutrons from ^{248}Cm determined by the time and original strength of neutrons from ^{252}Cf, the neutron production rate Q can be written as

$$Q = R(C + (1 - C)e^{-\lambda_{252}t}) + Se^{-\lambda_{250}t} \tag{4.17}$$

This rate can be fit to measurements taken at various dates.

Fission rate discrepancy

Significant discrepancies were found between neutron rates taken in close intervals to each other when large amounts of data were taken. These were eventually found to relate to the layers of the detector: The top line of calibration tubes showed a significantly higher rate than the bottom tubes when counting fissions using a 1.5 ms coincidence window.

Treating the top 8 calibration tubes and the bottom 32 tubes separately, a ratio of 1.0229 ± 0.0024 was seen between the fitted fission rates in the top of the detector and in the rest of the detector (Table 4.5). Fission rates were adjusted for the time they were taken using the ^{252}Cf half life, and calibration runs were compared to other runs closer in time than one week.

Date	Ratio	Error
April 20-26 2016	1.0212	0.0035
March 9-11 2016	1.0204	0.0053
June 9 2016	1.0262	0.0070
July 15 2016	1.0278	0.0058

TABLE 4.5: Comparison of top and lower fission rates. Best fit ratio is 1.0229 ± 0.0024. The ratios are consistent with this value with a chi-squared of 1.62/3, and inconsistent with 1 with a chi-squared of 89.54/4.

One possible explanation of this is the presence of the iron rings in the bottom 5 rows of the detector. Iron has an inelastic cross section for fast neutrons around 1 barn, making the capture of neutrons before thermalization possible. The total cross section for neutrons

in lead varies from 5 to 10 barns in the ^{252}Cf neutron's energy spectrum of about 1 MeV to 10 MeV, resulting in a mean free path of roughly 8 cm [31]. This distance is similar to the thickness of the lead rings of 4.7 cm, and the height of the ears on the lead blocks of 17.8 cm. This suggests that neutrons arriving at iron rings from the calibration tubes may still retain the angular correlations they had during fission.

Angular correlations have been found in ^{252}Cf fissions due to the Lorentz boost given to neutrons emitted from the fission products, resulting in a larger number of neutrons being emitted along the fission axis [47]. Calibration tubes are placed directly against the outer ring of the lead blocks, about 5 cm from the outside of the iron rings. As the rings fill only half of the depth of the lead block they occupy, there are gaps of 5.7 cm along the inside cylinder of the bore with no iron rings in place. This results in a fairly large solid angle (shown approximately in Figure 4.16) which could have a larger efficiency than other angles of the fission axis.

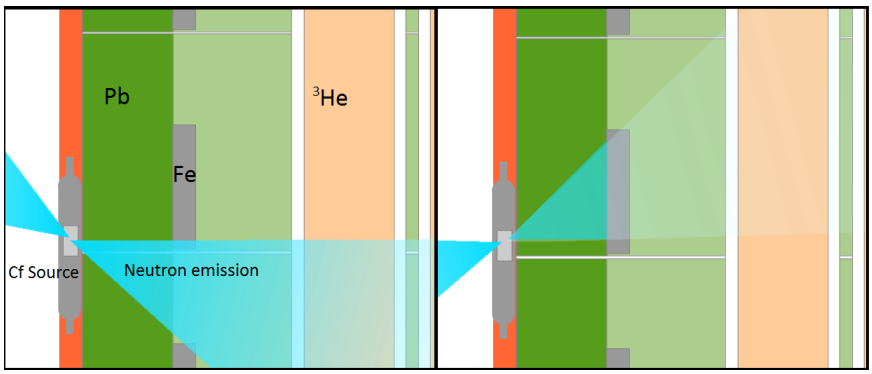

FIGURE 4.16: Possible distortions to the multiplicity fit from the iron rings. On the left is shown a high capture efficiency angle where neutrons miss the iron rings, with a low capture efficiency angle shown on the right.

Fitting a multiplicity distribution with more than one efficiency can result in a worse fit and invalid parameters. This was examined in the simulation with all simultaneous neutrons having the same energy, and with all neutrons starting in the same direction from any given fission.

To mimic correlation in neutron energy in fissions, 100,000 fissions were simulated at 7.435 MeV, and 100,000 at 0.435 MeV, all in the center of tube 11-2.

To mimic correlation in angle, 200,000 neutrons were simulated with energies from the ^{252}Cf distribution with the same random angle for all neutrons in a given fission.

Simulation	Fission rate relative deviation	Significance
Jet, Top	-0.0161	4.8
Jet, Bottom	-0.0105	3.1
Mixed Energy, Bottom	-0.0076	2.3

TABLE 4.6: Deviations in fission rate with neutron detection efficiency correlations

Because these scenarios involve much greater correlations than the fissions could realistically have, the low deviations in Table 4.6 rule out these explanations of the difference in fission rate between the top of the detector and the rest of the tubes.

The measured fission rates in the top and bottom of the detector were compared to the original source strength separately (Table 4.7, Figures 4.17 and 4.18).

Fission rates

Calibration	Year	Top fission rate	Other fission rate
Manufacturer	2011.51	57.46 ± 5.746	57.46 ± 5.746
Open Calibration	2016.1973	22.50 ± 0.105	22.05 ± 0.053
Closed Calibration	2016.3205	21.93 ± 0.0690	21.47 ± 0.0278
Extra Runs	2016.5479	21.12 ± 0.105	20.54 ± 0.066

TABLE 4.7: Equivalent ^{252}Cf fission rate measurements. Years are 365 day periods since January 1 2000 + 2000.

With the assumption that the source was created in 1985 based on the ^{250}Cf concentration compared to the normal initial concentrations [45], the activity of the isotopes was fit to the 4 measurements made of the source strength. Large errors exist far from the calibration time when the source strength is mostly constrained by the manufacturers measurement, but errors are small for most of 2016. On 2016 April 26, the source strength was equivalent to 21.93 ± 0.05 ^{252}Cf fissions per second according to the top tubes, and 21.48 ± 0.02 fissions per second according to the other tubes.

$$R_{top} = 45548 \pm 5558, S_{top} = 46.078 \pm 8.437, \rho_{top} = -0.999503 \tag{4.18}$$

$$R_{bottom} = 53934 \pm 3859, S_{bottom} = 30.821 \pm 5.875, \rho_{bottom} = -0.999787 \tag{4.19}$$

$$\begin{aligned}(\Delta Q)^2 =&(\Delta R(C + (1-C)e^{-\lambda_{252}t}))^2 \\ &+ (\Delta R(C + (1-C)e^{-\lambda_{252}t}))(\Delta S e^{-\lambda_{250}t})2\rho \\ &+ (\Delta S e^{-\lambda_{250}t})^2\end{aligned} \tag{4.20}$$

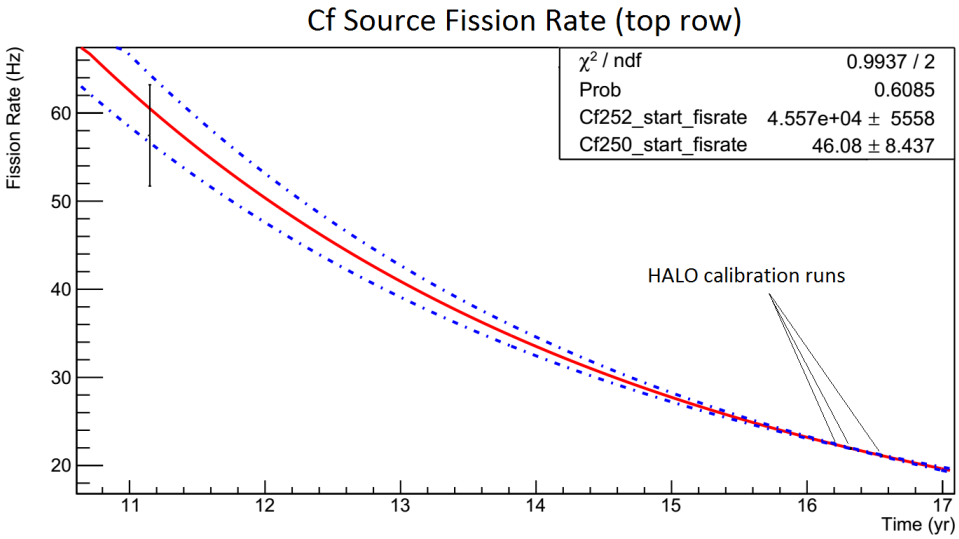

FIGURE 4.17: Top fission rate from Table 4.7

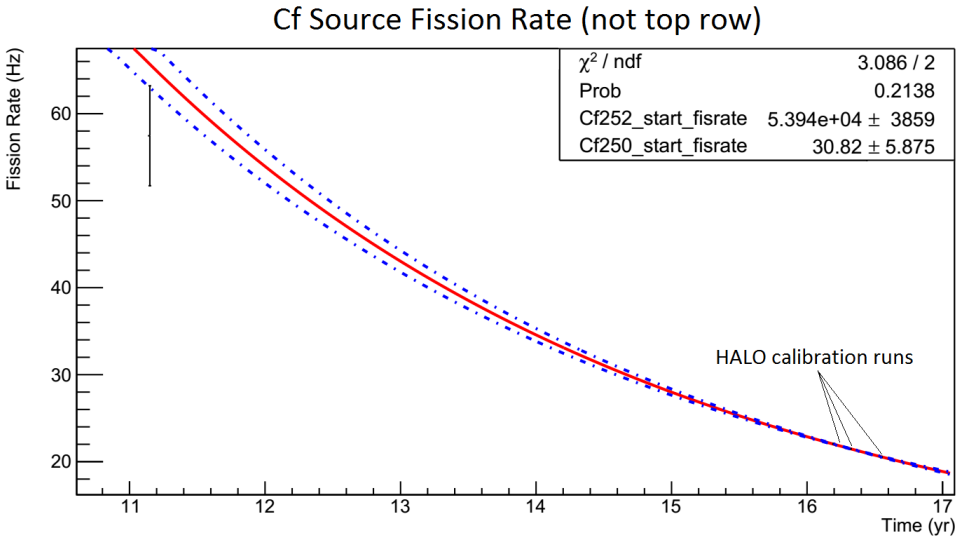

FIGURE 4.18: Bottom fission rate from Table 4.7

From these two distributions of isotopes, the fraction of neutrons created from each source around the time of the efficiency calibration can be found (Table 4.8).

Neutron Fraction	Not Top	Top
^{252}Cf	0.6852 ± 0.0491	0.5661 ± 0.0691
^{250}Cf	0.2732 ± 0.0521	0.3996 ± 0.0732
^{248}Cm	0.0416 ± 0.0030	0.0343 ± 0.0042

TABLE 4.8: Source composition from the top rows tubes and from the other tubes based on the decay rate. Starting time is 1985, and values are shown from 2016.32. Agreement is 1.4 sigma. The 'Not Top' values were used to calculate the isotope fractions to use in the multiplicity fit.

Resolving the fission rate discrepancy

Another explanation could be the splitting of individual fissions into multiple fissions when multiplicity is tagged. Neutrons are typically captured much faster than the 1.5ms time window, but if neutrons thermalized near the top of the detector tended to travel about 3 meters afterwards, they would be placed in a separate fission, increasing the measured fission rate.

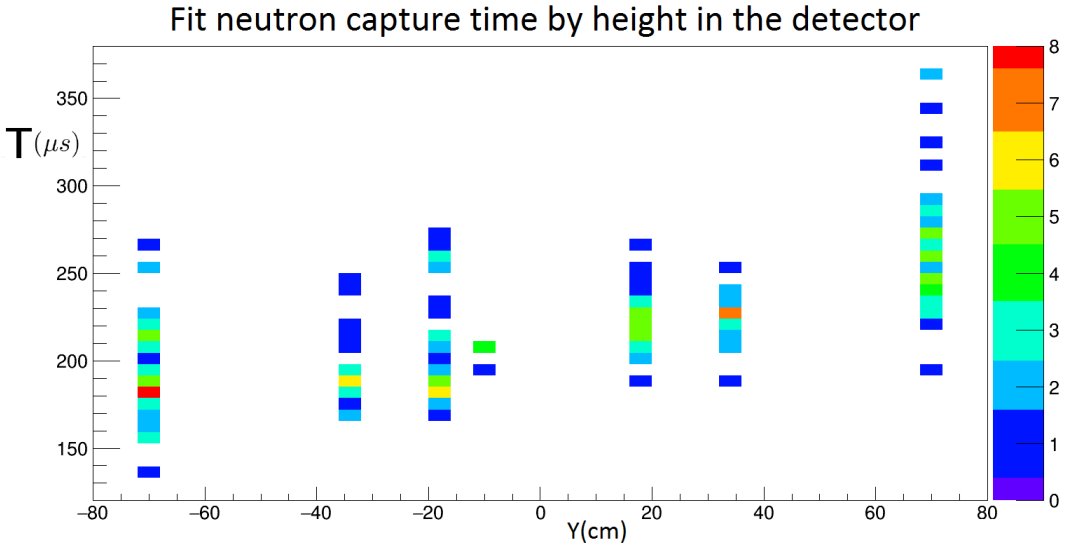

FIGURE 4.19: Time constant for the attenuation of neutrons found between 200 and 1500 μs after the first neutron in a fission was captured, taken with a 1.5 ms time window. Average time constant for the top tubes is 265 μs, where as the average time constant over all is 221 μs.

The fit neutron times in the long time window (§4.4.1) were examined as a function of height in the detector (Figure 4.19). This indicated longer capture times when the source was in the top tubes of the detector.

The average long characteristic time is 265 μs in the top tubes and 221 μs for all tubes. This only gives a chance of 0.35% and 0.11% for neutrons to be later than 1.5 ms. This seems small compared to the 2% discrepancy in neutron rate, but the large neutron multiplicity may enhance the effect enough. Changing the window to 2 ms reduces these probabilities to 0.05% and 0.01%. However, the spectrum could be non-exponential for long times and have a larger portion of late neutrons.

The multiplicity fit was re-run on the calibration data with a time window of 2 ms, up from the previous 1.5 ms time window. The fission rate found by excluding the top tubes was used for all tubes. This resulted in a chi-squared over ndf of 1183 over 1177 ($\mathrm{p} = 44.7\%$). This is a large improvement over the previous fits using only one fission rate for the whole detector and a 1.5 ms time window, which resulted in p≈0.05. The more significant discrepancies from the extra runs in Table 4.5 also disappeared with a 2 ms capture window.

Neutron capture efficiency in the top tubes increased by an average factor of 1.0196, very close to the expected change of 1.0203 from the correlation coefficients and change in n_f for the top tubes. ϵ in the the other tubes changed by a factor of 1.002 ± 0.002, indicating there were not many late neutrons in the bulk of the detector after 1.5 ms.

This fix proves that Figure 4.18 and the last column of Table 4.7 contain the correct rates to compare with future measurements.

4.4.4 Detection Efficiency

The 192 points, simulated with a 2 ms time window and a fission rate specified by the fit fission rate over time found in Figure 4.18, fit their detected multiplicity functions well, with a chi-squared of 1182.8/1177 $(\mathrm{p} = 44.7\%)$. The minimum and maximum likelihoods for individual points were 0.21% and 98.86%, with likelihoods of a lower minimum and

a higher maximum from U(0,1) likelihoods of 33.7% and 88.9% respectively. Sample covariance matrices and multiplicity fits can be seen in Table 4.9 and Figure 4.4.

n_f	ϵ	$\frac{\epsilon'}{\epsilon}$
19499.1	-0.155631	0.0012471
-0.155631	1.26873×10^{-5}	-1.29788×10^{-7}
0.0012471	-1.29788×10^{-7}	3.20291×10^{-7}

n_f	ϵ	$\frac{\epsilon'}{\epsilon}$
59966.4	-0.640206	0.00865542
-0.640206	1.27398×10^{-5}	-1.82059×10^{-7}
0.00865542	-1.82059×10^{-7}	8.97762×10^{-7}

TABLE 4.9: Covariance matrix for CT-33-10 z=0, $\epsilon = 0.49$ (top), and 61-11 z=120cm, $\epsilon = 0.21$ (bottom), corresponding to the fits in Figure 4.4

The efficiency very clearly fell off near the walls of the detector, but plateaued within about 50 cm of the detector center (Figures 4.20 and 4.21), suggesting a similar but much larger structure would detect neutrons with an efficiency just under the central values measured of (48.77 ± 0.034)% in the middle of CT-33-10 and (50.05 ± 0.33)% in the middle of tube 42-1. Tube 42-1 had the highest efficiency of all tubes, potentially due to its proximity to the bores with no iron ring in the the top two rows.

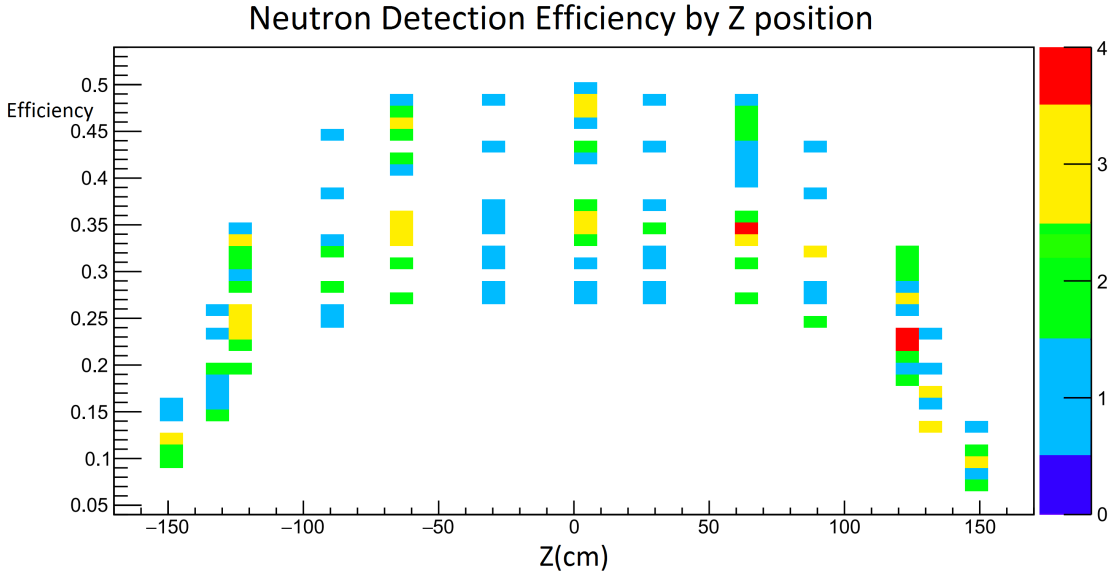

FIGURE 4.20: Neutron detection efficiency as a function of z: the depth into the detector.

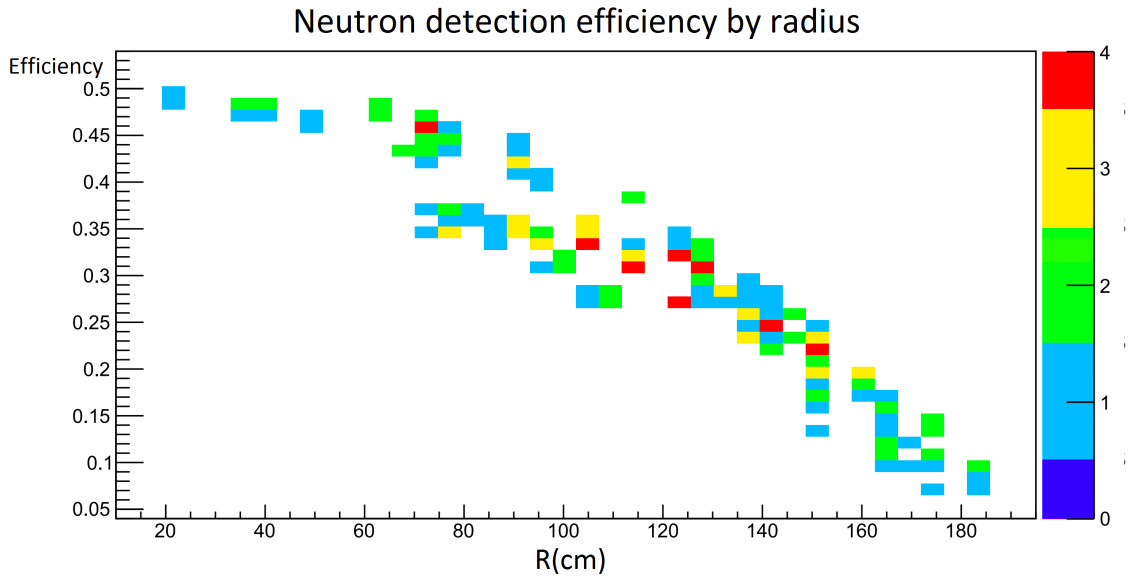

FIGURE 4.21: Neutron detection efficiency as a function of distance from the center of the detector. As the detector is short, the top and bottom of the detector have slightly lower efficiency than locations at similar radii, as seen around 80 to 100 cm.

The parameters from the efficiency fit can also be used to see the neutron travel distance in the detector. ${L_r}^{-1}$ can be thought of as the average number of channels used for detection neutrons at a particular point. This is shown in Figure 4.22 as the fraction of the detector used by the source.

Open Calibration

The calibration points that were taken before the front face of the detector was closed were compared to the closed calibration efficiencies. Although 125 data points were taken with the detector open, only 75 of those points were in the same location as a closed calibration point, since 16 of the tubes are inaccessible with the front face closed.

Large efficiency increases from closing the detector can be seen at the surface of the lead, but these quickly die off deeper into the detector (Figure 4.23) to very small efficiency differences.

The forward location in the open calibration of $z = 120\,\mathrm{cm}$ shows an expected increase by a factor of 1.021 ± 0.005. The $z = 0$ slice is consistent with no change in efficiency, but the $z = -120\,\mathrm{cm}$ slice also showed an increase by a factor of 1.019 ± 0.005.

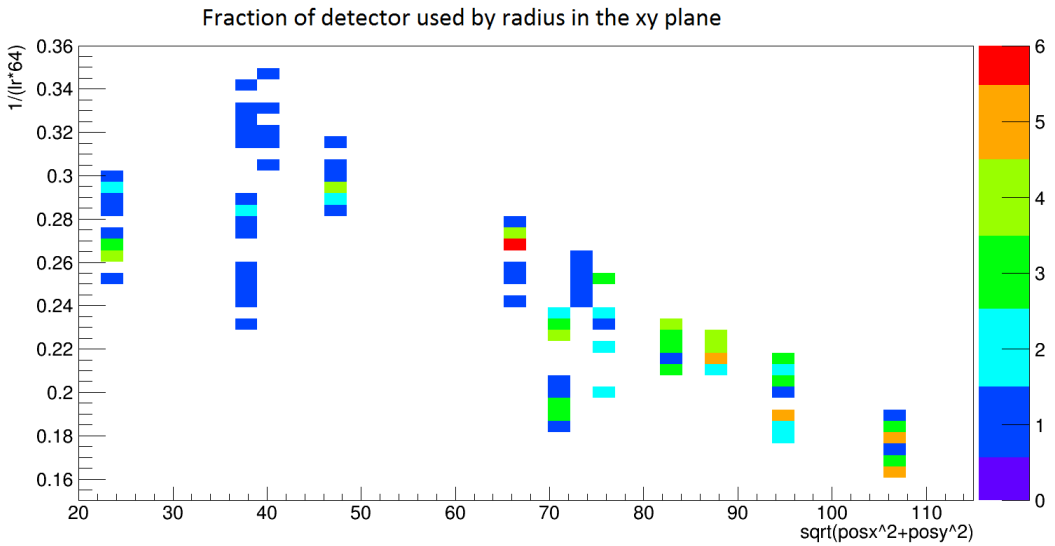

FIGURE 4.22: Fraction of detector used by distance from (X,Y)=(0,0), for all 192 calibration points. Fraction of detector used is found with $\frac{1}{64L_r}$, so uniform neutron flux over the whole detector would produce a fraction of 1.

The process of installing the front shielding on the detector caused many small vibrations in the detector noticeable by the data acquisition system and by people, but it seems very unlikely that these had any noticeable effects of the arrangement of the back of the detector.

A possible cause of a significantly higher efficiency in the back of the detector could be a measurement error between the open and closed calibrations, and a high efficiency gradient near the back of the detector. Because the rod positioning the calibration source was taped at measured calibration point lengths separately for the closed and open calibrations, if a tube were pinched or detached at the back in a way which caused the source to appear to hit the back of the detector at a slightly higher z value, this could shift all the results of one set of points away from the other. Measurement along the calibration rod is easy, so this would suggest that the efficiency difference at the front is underestimated by a factor of roughly 1.039.

Even with this high estimate of the efficiency increase in the front of the detector, the fraction of the lead involved suggests the overall relative efficiency change from the front shielding is still very small, on the order of 0.01.

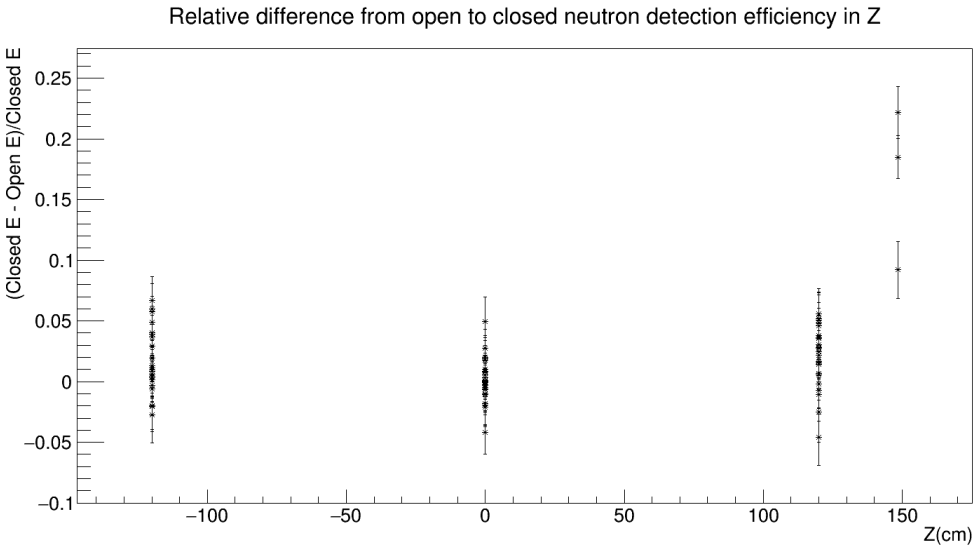

FIGURE 4.23: Relative difference in detection efficiency with the installation of the front shielding. The two highest results are from the corners of the detector in the front, and the third highest from the center front. Both the +120 cm and -120 cm positions are significantly above 0.

4.4.5 Calibration and Simulation Differences

The relative differences between the simulated and calibrated neutron detection efficiencies were recorded for each of the 192 locations. The average value of $\frac{\epsilon_{cal}-\epsilon_{sim}}{\epsilon_{sim}}$ was 0.0397, with a standard deviation of 0.0357 (Figure 4.24). If the detector and simulation had the same actual efficiency at every point, the standard deviation would be just 0.0133 from the statistics in the simulation and calibration, suggesting a systematic relative error in simulated versus real neutron detection efficiencies at any point of 0.0331, in addition to the relative increase of 0.0397.

The relative differences between the simulation and the calibration runs were also plotted over the y and z axes to see any significant local differences (Figure 4.25).

Very large differences were found in the back of the detector, with the calibrated efficiencies being much higher (Figure 4.25). This could have been caused by the accuracy with which the source location was determined. The gradient in the middle of the detector was verified to be small but a position error on the order of a centimeter could have a much larger effect at the outside of the detector. The lack of a lower calibrated efficiency at the front of the detector, however, makes this seem unlikely, as the distance between

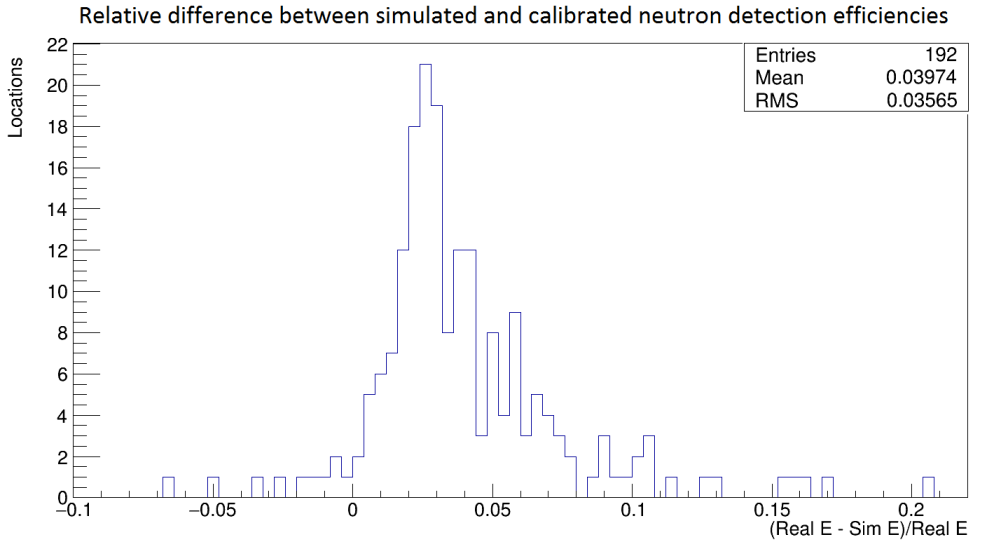

FIGURE 4.24: Relative differences between calibrated and simulated results

the furthest forward and furthest backward point is well constrained. The most plausible source of error in the z direction is the locations of the plates at the back of the tube which are attached to the columns of many lead blocks, which would have resulted in the front points on the detector being further out than the simulations they were compared to. There does not appear to be a significant drop in calibrated efficiency relative to simulated efficiency in the front of the detector (Figure 4.25), so errors in position measurement cannot explain the planes of high discrepancy near the front and back of the detector.

Efficiency differences were also plotted in Y (Figure 4.26). Some rows such as the top and bottom may appear higher due to having more tubes with 13 sample points, giving them more z=-150 locations.

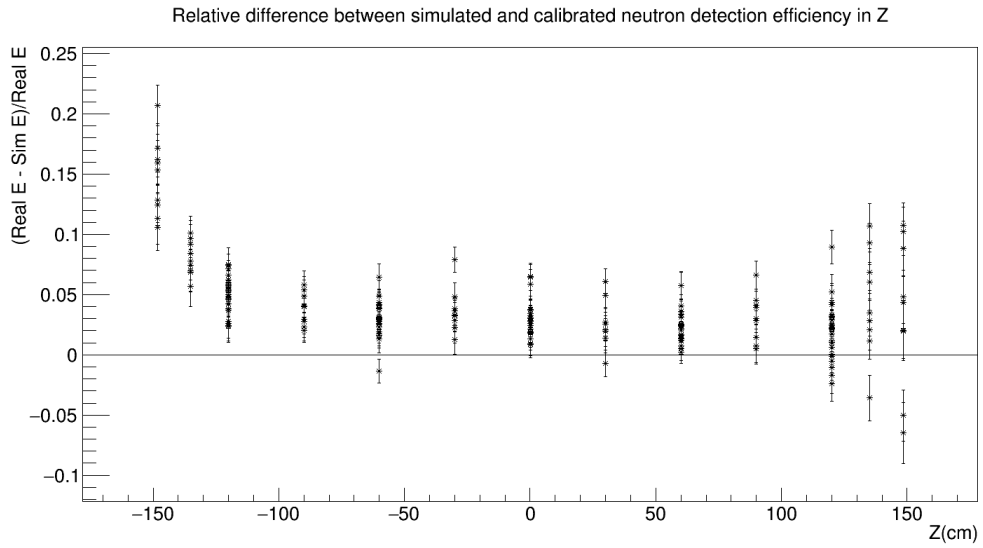

FIGURE 4.25: Relative differences between calibrated and simulated results

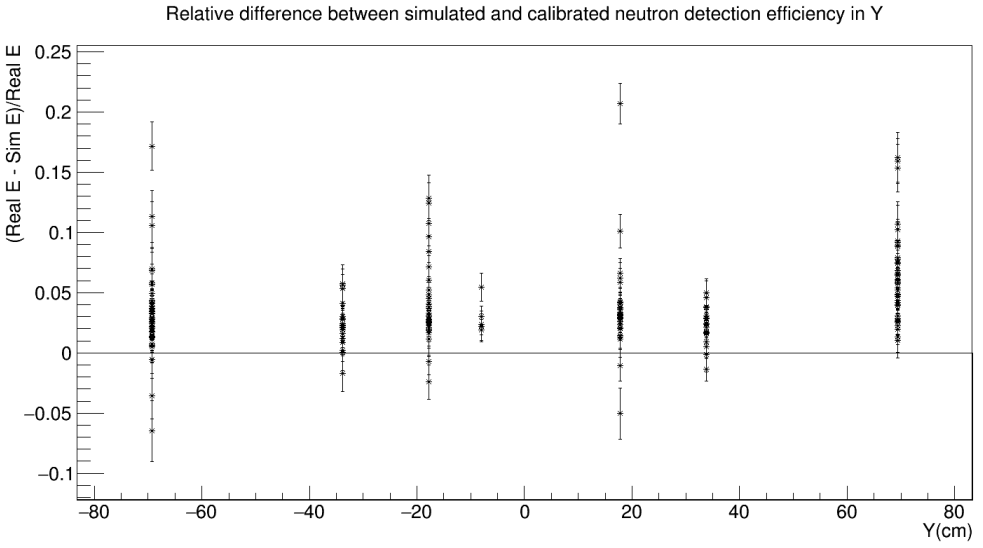

FIGURE 4.26: Relative differences between calibrated and simulated results

4.4.6 Supernova Neutrino Efficiency

Supernova induced neutrons will have a different energy spectrum than those from Cf, and will be created uniformly throughout the lead volume instead of the calibration tubes. To find the efficiency for these neutrons, a simulation was run with 100000 2-neutron events distributed randomly in the lead in version 169 of the HALO simulation, allowing the run to measure both single neutron capture efficiencies and the multiplicity distribution detected from neutrino-induced 2n events. These neutrons were given energies according to the expected distribution for supernova induced neutrons in lead [48].

54357 of the 200000 neutrons simulated were detected, giving an efficiency of $\epsilon_s = 0.271785 \pm 0.000995$. Since the simulation did not exactly reproduce the calibration results, the efficiency from the simulation must be adjusted to accurately depict the supernova neutron detection efficiency.

The simulation appeared to underestimate the efficiency. The mean and its standard deviation from Figure 4.24 quantify this, with $R = \frac{\epsilon_r - \epsilon_s}{\epsilon_r} = 0.0395 \pm 0.0026$ (Figure 4.24). The real efficiency is then related to the simulated efficiency by $\epsilon_r = \frac{\epsilon_s}{1-R}$. The error in this real efficiency is composed of the statistical error from the simulation of $\frac{\Delta\epsilon_s}{1-R} = 0.001036$, the error in the factor R of $\Delta R \frac{\epsilon_s}{(1-R)^2} = 0.000758$, and the systematic error σ_{sys} found in Figure 4.24 after removing the statistical error, applied to the 100000 points chosen in the simulation: $\frac{\sigma_{sys}}{\sqrt{100000}} \frac{\epsilon_s}{(1-R)^2} = 0.000031$.

The calibration uses a neutron region of interest from bin 280 to 1300 of the raw ADC spectrum. For the supernova trigger, the region of interest is set to bins 380 to 1300 (§5.3). This results in a small loss of efficiency. To measure this loss, 80-minute source runs 5380, 5382, 5384, 5386, and 5388 were used, taken in CT-61-11 $z = 120\,\mathrm{cm}$, CT-61-11 $z = -120\,\mathrm{cm}$, CT-33-10 $z = 0$, CT-11-2 $z = 120\,\mathrm{cm}$, and CT-11-2 $z = -120\,\mathrm{cm}$ respectively. The 120 minute run 5263 at CT-33-10, $z = 0$ was also included. The ratio of counts from bins 380 to 1300 to the counts from bins 280 to 1300 was $k = 0.9757 \pm 0.0016$. This scales the trigger efficiency $\epsilon = k\epsilon_r$, and all associated errors similarly. The scaling error of $(\Delta k)\epsilon_r = 0.000459$ is also introduced.

For the analysis of a supernova, the full neutron spectrum can be used, as the background rate of about 0.033 Hz in the full spectrum is still too low to cause problems over the tens of seconds in which supernova induced neutrons can be detected.

Finally, errors in the isotopic composition and multiplicity can effect the calibrated efficiency. Simulation runs with different multiplicities in Table 4.4 gave a multiplicity dependent efficiency result of $\epsilon(f) = \epsilon_0 - m(f - 0.48)$, where $\epsilon_0 = 0.4583 \pm 0.0006$, $m = 0.0285 \pm 0.0017$, and $f = {}^{250}\text{Cf}$ fissions per fission. Taking this as a measure of the relative change in efficiency with the relative change in multiplicity, the errors can be found from the errors in ^{250}Cf and ^{248}Cm concentrations from Table 4.8: $\frac{\epsilon}{\epsilon_0} m \frac{\Delta(^{250}\text{Cf fissions})}{\text{fission}}$ and $\frac{\epsilon}{\epsilon_0} m \frac{\Delta(^{248}\text{Cm fissions})}{\text{fission}} \frac{\bar{\nu}(^{252}\text{Cf}) - \bar{\nu}(^{242}\text{Cm})}{\bar{\nu}(^{252}\text{Cf}) - \bar{\nu}(^{250}\text{Cf})}$ respectively. These errors evaluate to 0.000917 for ^{250}Cf and 0.000149 for ^{248}Cm (Table 4.3).

Because the ^{248}Cm concentration in 1985 is assumed to be 0, the errors from the concentrations of ^{248}Cm and ^{250}Cf are perfectly anti-correlated, and would normally be subtracted. However, the start time of 1985 is not yet confirmed. For this reason the errors were treated as independent.

The errors in the ^{252}Cf multiplicity distribution are evaluated in a similar way, giving an error of $\frac{\Delta(\bar{\nu}(^{252}\text{Cf}))}{\bar{\nu}(^{252}\text{Cf}) - \bar{\nu}(^{250}\text{Cf})} \frac{\epsilon}{\epsilon_0} m = 0.000573$, with the value of $\Delta(\bar{\nu}(^{252}\text{Cf}))$ taken by assuming the errors in Table 4.2 are independent. These values are all combined in Table 4.10.

Along with the backgrounds present in HALO, the detection efficiency for neutrons determines the detection range for supernovae (§5.3.4).

Neutron Detection Efficiency (Trigger)	0.2761 ± 0.0017
Neutron Detection Efficiency (Supernova)	0.2830 ± 0.0017
Statistics: supernova simulation	0.001036
Simulation and calibration error in mean difference	0.000758
Simulation and calibration diffuse differences	0.000031
Unknown ^{250}Cf concentration	0.000917
Unknown ^{248}Cm concentration	0.000149
Error in average neutron multiplicity	0.000573

TABLE 4.10: Efficiency for detecting supernova neutrons and the associated uncertainties. Errors listed are for the detection efficiency during a supernova, not the trigger detection efficiency. Error in ^{250}Cf concentration uses the response rate from the simulations in Table 4.4. Error in average neutron multiplicity likely overestimates the error in the ^{252}Cf average multiplicity by assuming the measured multiplicity bins are independent, but underestimates the errors for the other isotopes which are assumed to have a multiplicity distribution and errors proportionate to those of ^{252}Cf

4.4.7 Dispersed Multiplicity Detection

Because neutrons in bursts from events in the lead are created at a point with a specific capture efficiency not necessarily similar to the average efficiency, the multiplicity distribution will transform differently for these events than it would at any consistent point. This difference is important when analyzing diffuse ^{238}U SF in the detector (§5.2.1) and when determining the number of 2n interactions from supernova neutrinos. This probability was found with a simulation of double neutron events throughout the lead volume.

For this study, version 180 of the simulation was used. 100000 2n events were simulated, giving an efficiency of 0.2736 ± 0.0010, with 8979 2n events and 36758 1n events. These numbers were scaled to the calibrated efficiency listed in Table 4.10 by the first efficiency derivative of the probability under uniform conditions, that is $\frac{dp_2}{d\epsilon} = 2\epsilon$, $\frac{dp_1}{d\epsilon} = 2 - 4\epsilon$, and $\frac{dp_0}{d\epsilon} = -2(1-\epsilon)$, to obtain Table 4.11. Errors on these derivatives were assumed to be proportional to the deviation of the probability from the uniform probability and efficiency errors were propagated.

Detected Multiplicity	Probability from 2n
0	0.5389 ± 0.0037
1	0.3699 ± 0.0026
2	0.0912 ± 0.0016

TABLE 4.11: Detection probabilities for a 2n neutrino interaction. Probabilities are based on simulation and adjusted for differences with calibrated efficiency.

Chapter 5

Supernova Monitoring

Supernovae are expected to produce a strong signal for a couple of seconds, followed by a slowly dissipating neutrino flux over the next several seconds, as seen in Supernova 1987A (Figure 5.1).

HALO receives background events from a variety of sources, including gamma rays, beta decay, electrical noise, alpha particles, diffuse neutrons, uranium SF, and spallation events. Events that cause bursts of counts are of particular interest for supernova monitoring. They must be reliably distinguished from a supernova signal to prevent false alarms.

5.1 Non-neutron Events

5.1.1 Low Energy Interactions

The most important low energy background comes from gamma rays interacting in and around the ^{3}He gas. Although gammas typically have energies of the MeV order, the electrons they excite though Compton scattering have a low energy deposition per unit length in the gas, so the vast majority of gamma interactions produce an ionization corresponding to an energy deposition of less than 200 keV.

The total rate of counts above the current threshold and below 156 keV is about 4.95 Hz, mostly from Compton scattering. Events in this windows are recorded because they are far enough from the neutron region of interest to monitor for consistency during a supernova.

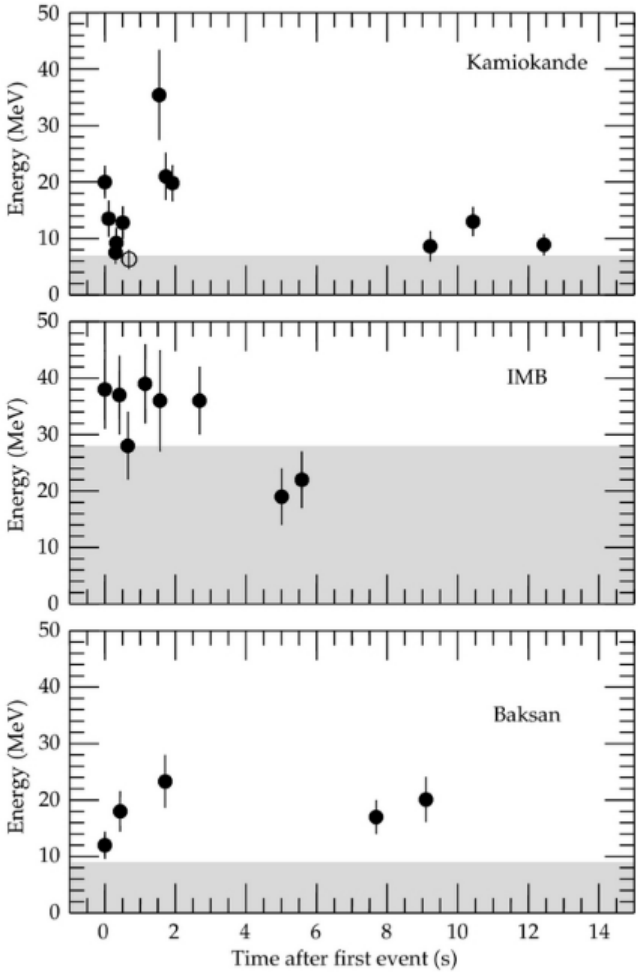

FIGURE 5.1: Neutrinos detected on earth during Supernova 1987A [49]. Energies are the measured energies of the charged lepton from charged current reactions. Shaded areas have trigger efficiencies <30%

The ^{3}He counters also have a high rate of tritium decay left over from the creation of the ^{3}He gas. The tritium beta decay end point is under 19 keV, preventing it from affecting neutron counting. The hardware energy thresholds prevent these decays from being digitized in normal runs.

5.1.2 Electrical Noise

Bursts of electrical noise occur in HALO a few times a month during normal detector operation. Some of these have been caused by people brushing against high voltage cables, seismic activity, or other detector shaking activity such as drilling screws into the

frame. These bursts consist of very large numbers of counts, but these are typically at low energies, allowing them to be distinguished from neutron capture events.

5.2 Neutron Bursts

HALO records some bursts of events with energies consistent with neutron captures. These bursts are caused by muon induced spallation events or by spontaneous fissions of ^{238}U in the detector. Bursts of two neutrons occur a few times per day, but only a few times per month is there a burst of significantly higher multiplicity. Neutron bursts can be discriminated by their time distribution in the detector, since the neutrons are all created at the same instant, and captured within the next 1.5 ms.

To designate bursts as spallations or spontaneous fissions (SF), the neutron multiplicity of the burst is used. Bursts with multiplicities of 5-12 occur at rates mostly independent of their multiplicities, whereas bursts with a multiplicity of 2-4 occur much more frequently in low multiplicities. Uranium SF is limited to lower neutron multiplicities than spallation events [50] [51], so for convenience bursts of multiplicity $\leq$4 are considered to be spontaneous fission events, and bursts of multiplicity $\geq$5 are considered to be spallation events.

5.2.1 Spontaneous Fission

By looking for coincidences in the neutron region of interest (ROI) (channel 380 to 1300) with a time window of 1.5 ms and subtracting the expected coincidence rate based on the neutron background rate, the multiplicity distribution was found for SF events.

Multiplicity	Bursts per day	Error
2	3.517	0.412
3	0.815	0.198
4	0.192	0.096

TABLE 5.1: Neutron coincidence rates in HALO, found with 20.8 days of data, from run 5154 to 5213 (May 2 to May 24 2016) using a 1.5 ms coincidence window. Expected Poisson coincidences were subtracted.

Using the HALO simulation, the detected multiplicities can be used to determine a total rate of SF in the detector, specifying a quantity of uranium in the detector.

Multiplicity	Production Probability	Error	Detection Probability	Stat Error (Sim)
0	0.048	0.005	0.571	0.004
1	0.219	0.040	0.328	0.003
2	0.425	0.084	0.088	0.002
3	0.228	0.026	0.012	0.001
4	0.042	0.011	0.001	0.0002
5	0.007	0.001	0.0002	0.00009

TABLE 5.2: Multiplicity distribution of neutrons emitted in ^{238}U SF (Average 1.99 ± 0.03, from [50]) and simulated detected multiplicity distribution using revision 142 with ^{252}Cf SF neutron energies and the shown values for the ^{238}U neutron multiplicity distribution.

With a probability per fission of seeing a given neutron multiplicity and the detection rate of each multiplicity, the total fission rate can be calculated from the multiplicities 2, 3, and 4. This results in 40.1 ± 4.1, 66.2 ± 16.4, and 198.3 ± 105.8 fissions per day respectively, ignoring the errors on the ^{238}U SF distribution.

Fitting the results from all three multiplicities for one fission rate gives a value of 42.5 ± 4.7 fission per day with a chi-squared value of 4.5/2. This measurement is sensitive to errors in the ^{238}U SF neutron multiplicity distribution, contributing a systematic error close to 20%. The fission rate corresponds to 50 mg of ^{238}U in the detector, or 0.63 ppb uranium in the lead.

5.2.2 Spallations

Bursts above a multiplicity of 4 were tagged as spallation events, provided they occurred in less than the 10 ms limit set in the burst monitor and agreed with the energy deposition distribution of neutron capture.

From January 1 2015 to July 11 2016, 45 such bursts were detected. Subtracting 5.52 of the 5-neutron SF events expected from the previously measured SF rate gives an observation of 0.071 ± 0.013 spallations per day, close to uniformly spread over multiplicities from 5 to 12 (Figure 5.2).

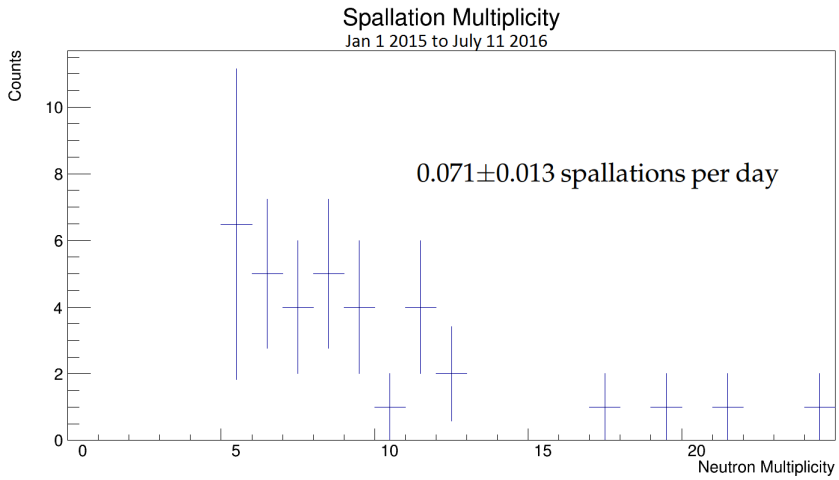

FIGURE 5.2: Spallations from Jan 1 2015 to July 11 2016. 5.52±2.6 counts were removed from the n=5 bin due to the SF rate calculated above. One count was also found at n=98.

Pyhasalmi mine comparison

To verify that this rate of neutron bursts can be explained by spallations, a comparison was made to another underground neutron detector experiment that used lead as a target. A 30 cm cube of lead was surrounded by ^{3}He counters and placed in Pyhasalmi mine in Finland, at a depth of 1185 meters water equivalent (m.w.e) [51]. The configuration was found to have an efficiency of 0.232 for ^{252}Cf neutrons produced in its center. With this arrangement only 6 bursts were detected with multiplicities of 7 or greater in 60 days.

HALO has a simulated efficiency for ^{252}Cf neutrons produced uniformly in lead of 0.269 as of revision 142. This can be scaled using the simulation and calibration difference and the burst monitor trigger threshold to 0.273 (§4.4.6). Because the Pyhasalmi detector has its neutron counters on the outside, it is reasonable to assume that its neutron capture efficiency is mostly independent of position, making the two detector's Cf neutron capture efficiencies comparable.

SNOLAB is at a depth of 6011 m.w.e. Muon flux falls off quickly with depth, but the energy spectrum also hardens with depth. These effects can be approximated by a Depth Sensitivity Relation (DSR) stating that muon-induced events are suppressed by a factor of 10 for every 1500 m.w.e. [52]

Using the efficiency ratio of $\frac{0.273}{0.232}$ between HALO and the Pyhasalmi detector to scale

the spallation threshold of 7 at Pyhasalmi gives a threshold 8.24 neutrons at HALO to make a comparison. All bursts of multiplicities 9 and higher were included, plus $0.55*$(multiplicity 8 bursts) for a total of 18.78 events from January 1 2015 to July 11 2016. Scaling this to the depth of 1185 MWE in Pyhasalmi mine by a factor of $10^{\frac{6010m.w.e-1185m.w.e}{1500m.w.e}}$ gives $257 \pm 59 \frac{spallations}{tonnePb*year}$. This has a discrepancy of 1.8 σ from the Pyhasalmi measurement of $119 \pm 49 \frac{spallations}{tonnePb*year}$. This is a reasonable agreement especially considering the limitations of the DSR.

At a shallower depth, the Pyhasalmi detector also observed a peak in neutron multiplicity around 23-24 neutrons detected. If enough statistics were accumulated to see this feature in HALO, it would be blurred due to the variation of capture efficiency throughout the volume of lead.

Spallation size

The sample RMS of the 2 dimensional positions around the average 2D position of all the counts in the spallation events were recorded and found to be smaller than the position RMS of random neutron coincidences in the detector.

Event	Position RMS (mm)	Sample standard deviation
Random 4-neutron coincidence	781	212
Spallation	530	158

TABLE 5.3: Spallation and neutron coincidence spread and their deviations. The deviation of random coincidences should become smaller with larger multiplicities, but spallation may not necessarily be consistent at high multiplicities due to different starting points in the detector accessing more localized areas.

The spallation and coincidence spreads are very different in aggregate but are not clearly distinguishable for individual events [53]. Supernovae could also have a smaller spread than neutron coincidences since the neutron production in lead will lead to a higher neutron flux near the center of the detector, and because efficiencies are higher near the center of the detector. For these reasons HALO will exclusively use the timing of the neutron counts rather than their position to tag spallation events.

5.3 Supernova Trigger

When detecting neutrons at a high rate, such as during calibration runs with the ^{252}Cf source, all neutrons can be found between bins 280 and 1300, where the 764 keV neutron capture peak is found at bin 1223. To suppress the tail of the gamma background, a range of bins 380 to 1300 is used for neutrons in the supernova trigger. This causes a reduction in efficiency for triggering to 0.276 from 0.283 (§4.4.6). More filters are used to tag background events to be excluded from the SNEWS alarms [54] and displayed in burst notifications [55].

5.3.1 Neutron Spectrum Filter

Because captured neutrons can lose energy due to tritons or protons escaping the counter gas, they have a unique shape consisting of a full capture peak at channel 1211.5 and a partial capture tail down to channel 280 (Figure 2.9). Knowledge of the fraction of neutrons which deposit all of their energy can be used to remove bursts that enter the neutron ROI but do not display the same distribution of deposited energies as neutrons.

To determine how neutron-like a given spectrum is, a channel C is chosen for which all counts in the neutron ROI above C are considered to be in the peak and all counts below C are in the tail. From a known neutron spectrum a likelihood $P(C)$ can be found for neutrons being above channel C. Then with N neutrons captured, the probability of having k neutrons in the peak is

$$p(k) = \frac{N!}{k!(N-k)!} P(C)^k (1 - P(C))^{N-k} \tag{5.1}$$

Then if n neutrons are detected in the peak, the likelihood is

$$L(n, N) = \sum_{k=0}^{N} p(k)(|k - P(C)N| >= |n - P(C)N|) \tag{5.2}$$

For a burst to be labeled as a supernova candidate, $L(n, N)$ must be greater than 0.001. This cutoff was chosen to have a negligible effect on supernova detection, and was seen

to be sufficient when implemented. The values used for this check are $C = 900$ and $P(900) = 0.89$.

5.3.2 Backgrounds Filter

Burst data is saved from 5 seconds before the start of the burst up to the count before the first count in the neutron ROI that does not meet the burst condition. In this time window, backgrounds can be observed to exclude bursts that are not entirely composed of neutrons.

Alpha decays in the walls of the ^{3}He counters can have energies of a few MeV which easily overflow the domain of the ADCs. This energy is attenuated by the counter walls for deeper alpha decays, resulting in a roughly uniform distribution of energy depositions.

Compton electrons from gamma rays make up the bulk of the background rate in the HALO detector. Because Compton electrons deposit energy on the order of a few keV per cm in the counter gas which has a diameter of only 5 cm, these counts are concentrated in the low energy region.

To prevent small deviations in the neutron distribution, due to unforeseen circumstances, registering as an increase in background, some space is left between the neutron distribution and the regions used to measure gamma and alpha counts. Counts above channel 1400 are labeled as "alphas", and counts below channel 250 are labeled as "gammas". Alphas occur at a rate of about 319 per day, whereas gammas occur at a rate of about 4.95 Hz at the current thresholds.

Both of these backgrounds follow Poisson distributions:

$$p(k) = \frac{(RT)^k e^{-RT}}{n!} \tag{5.3}$$

Likelihood is calculated similarly to the neutron spectrum filter, unless over 100 gamma counts are detected in which case a normal distribution is used to find the likelihood instead. If gamma and alpha likelihoods both exceed 0.00001, the burst can be accepted as a supernova candidate. This low likelihood cutoff was chosen because the background

filters are mostly redundant with the neutron spectrum filter (§5.3.1). If the gamma count rate is below average, the gamma likelihood is passed automatically so as to allow for operation with parts of the detector compromised.

5.3.3 Time Filter

Spallation events occur frequently in HALO, and must be discriminated against. Spallations create a short burst of neutrons which are usually all captured within the first millisecond (Figure 5.3). This is much shorter than the expected supernova signal which would occur over a number of seconds.

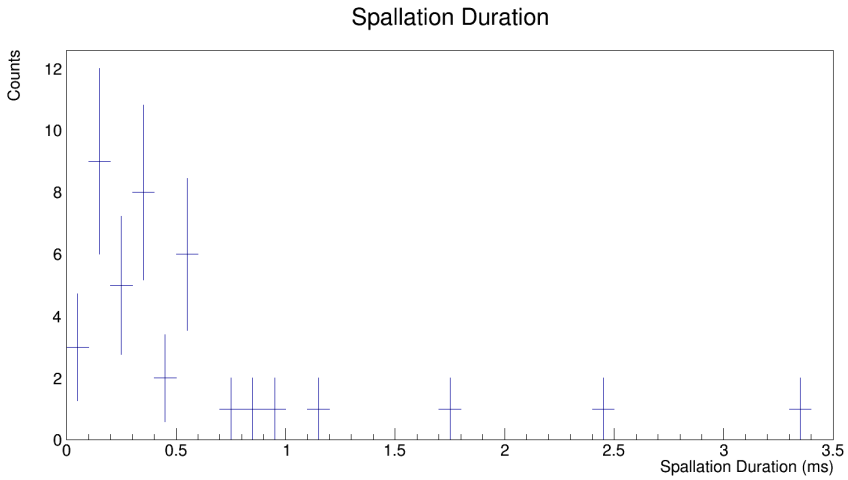

FIGURE 5.3: Spallations from Jan 1 2015 to July 11 2016. Durations are consistently short compared to all possible supernova signals.

The duration of spallation events is fairly close to those predicted from the fission time in the detector. Assuming that neutron capture follows an exponential distribution with time constant $T = 220\,\mu$s (Figure 4.11) with probability $p_{long} = 0.64$, (Figure 4.9) then the median total time m between the first and last neutron in a burst of multiplicity n can be calculated to be

$$m = -T \ln\left(1 - \frac{1}{2}^{\frac{1}{p_{long}{}^{n}}}\right) \tag{5.4}$$

The mean value of m for the spallation events was 464 μs. The median duration of the spallation events was only 330 μs. Out of the 42 spallations 27 had durations shorter than the predicted median of 464 μs, constituting a deviation of 1.85 σ.

To discriminate against short bursts of neutrons coincident with background neutrons, the time after count i before count $i+1$, dt_i is used. A reduced duration D_r shorter than the duration $D = \sum_{i=1}^{N-1} dt_i$ is defined as

$$D_r = D\left(1 - \sqrt{\frac{\sum_{i=1}^{N-1} {dt_i}^2}{D^2}}\right) \tag{5.5}$$

This is similar to removing the longest time difference from the burst duration. For a burst to be labeled as a supernova candidate, it must have $D_r > 10\,\mathrm{ms}$.

5.3.4 Supernova Detection

The closed detector with the Cf source stored nearby counts 1294±8 neutrons per day (Table 5.4). The SF rates (Table 5.1) combine with these background neutrons to create the bulk of the background rate for the SNEWS alarms.

Neutron source	Neutrons per day
Ambient Poisson Neutron Background	1202.6 ± 43.5
Cf Source in Storage Barrel	79.9 ± 42.7
Spontaneous Fission	10.2 ± 1.1
Spallation Events	1.2 ± 0.2
Total	1293.9 ± 7.9

TABLE 5.4: Neutron background sources and rates. Spallation and SF neutron rates are taken from their multiplicity distributions (Figure 5.2 and Table 5.1). The Cf source neutron detection rate was measured in run 5377 where the source was moved around the corner for 16 hours and 32 minutes.

From the Poisson neutron background, the rate of random coincidences can be calculated as follows. Every detected neutron will be the first neutron in a burst of multiplicity M only if $M-1$ neutrons are captured within the coincidence window $W = 2\,\mathrm{s}$ starting at this neutron. This means for a neutron background rate of R, the M-neutron coincidence rate R_M is

$$R_M = R \times \frac{(RW)^{M-1} e^{-RW}}{(M-1)!} \tag{5.6}$$

Any ordinary coincidence of K separate coincident neutron events can become a neutron burst of higher multiplicity M if one of the events in the coincidence is not a single neutron but instead a burst of $N = 1 + M - K$ neutrons. Because the probability that a neutron event is a burst of neutrons is low, the rate of coincidences of multiplicity M from bursts with multiplicity N is

$$R_{(M,N)} = R_{1+M-N} P_N (1 + M - N) \tag{5.7}$$

Where P_N is the probability that a randomly chosen instantaneous neutron event has multiplicity N. This allows for the calculation of alarm rates from Poisson and SF neutrons.

Spallations contribute similarly to 4n SF events when the threshold is at 4 neutrons, requiring two additional neutrons to register an alarm. This contributes 0.034 alarms per year to SNEWS. These alarms plus the non-short alarm rate from all bursts of 4 or more neutrons (Table 5.5) resulting in a total of 4.30 alarms per year expected from all sources of neutrons.

M	1n/day	2n/day	3n/day	4n/day	Total/yr	Non-short/yr
1	1294	0	0	0	472288	472288
2	37.61	3.547	0	0	15023	13729
3	0.5633	0.2062	0.8148	0	578	206
4	0.005624	0.004632	0.04737	0.1917	91.0	3.74
5	4.2×10^{-5}	6.2×10^{-5}	0.00106	0.01115	4.495	0.426
6	2.5×10^{-7}	5.8×10^{-7}	1.4×10^{-5}	2.5×10^{-4}	0.0969	0.0969
7	1.3×10^{-9}	4.2×10^{-9}	1.3×10^{-7}	3.3×10^{-6}	0.00127	0.00127
8	5.4×10^{-12}	2.4×10^{-11}	9.5×10^{-10}	3.1×10^{-8}	1.2×10^{-5}	1.2×10^{-5}

TABLE 5.5: Rates of detecting bursts of certain neutron multiplicities M from the background rates of occurrences of 1 to 4 simultaneous neutrons. Non-short bursts refer to all bursts of the given neutron multiplicity consisting of three events at distinct times. This is the rate that will make up the SNEWS background. With a threshold of 4 neutrons, these values as well as 0.071 spallations per day give a SNEWS alarm rate of 4.30/yr, below the specified acceptable rate of 6/yr. [7]

The neutrino energy spectrum from a supernova can be parameterized as a pinched Fermi-Dirac distribution with an average temperature T and pinching parameter η_α

$$\Phi(E_\nu) \propto \frac{{E_\nu}^2}{\exp(E_\nu/T - \eta_\alpha) + 1} \tag{5.8}$$

Where E_ν is the neutrino energy [36].

Assuming the average neutrino energy is $18\,MeV$ and $\eta_\alpha = 2$, at a range of 10 kpc a supernova neutrino pulse is expected to produce 0.69 neutrons per tonne of lead [36], with half of these neutrons produced in the first two seconds. With a threshold of T neutrons in two seconds, the approximate edge of the neutron detection range of HALO is at

$$R = \sqrt{\frac{\epsilon}{2}\frac{0.69M}{T\,\text{tonnes}}100\,\text{kpc}^2} \tag{5.9}$$

With $T = 4$ and $M = 79\,\text{tonnes}$, HALO has a detection range of 13.7 kpc. More accurately, the detection probability for supernova can be seen as a function of distance in Figure 5.4.

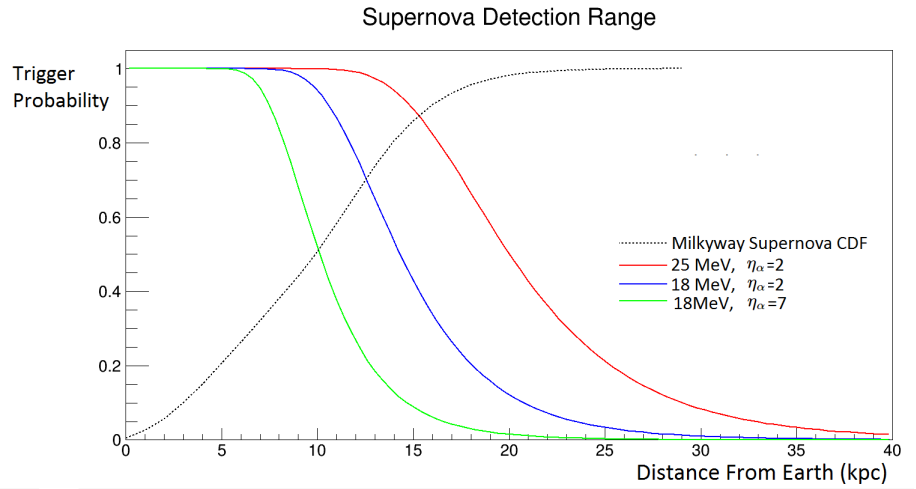

FIGURE 5.4: Probability of detecting at least 4 neutrons in the 2 second trigger window as a function of the distance to the supernova. Only the statistical errors in neutron production are represented. Values used are 0.345/0.69/1.35 neutrons per tonne at 10 kpc, $\epsilon = 27.61\%$, with 50% of the neutrons appearing in the trigger window. Supernova distance cumulative distribution function (CDF) from [56]. Trigger probabilities for a supernova by HALO weighted by the probability density of supernova ranges are 0.526, 0.770, and 0.942 for the three supernova models shown.

Chapter 6

Conclusions

HALO was calibrated using a Cf neutron source. Using a multiplicity fit, the calibration's 192 locations was analyzed for their neutron capture efficiency throughout HALO. This data also allowed the determination of the composition of the neutron source, and a characterization of neutron capture times throughout the detector.

The simulation's precision in predicting neutron capture efficiencies was verified to within a relative difference of less than 0.04. The simulation was then used to evaluate likely outcomes of a two neutron neutrino interaction, and to find an overall efficiency of detection supernova induced neutrons of (28.30$\pm$0.17)%. In trigger mode the efficiency is reduced to (27.61$\pm$0.17)%. Determining these efficiencies was the primary goal of the calibration and the main result of this thesis.

Neutron lifetimes in the detector were also measured with the Cf source. A majority of neutrons were captured with an exponential time constant of 221 μs, while a smaller population was absorbed on the order of 10 times faster.

To achieve this precision, updates had to be made to the HALO Monte Carlo simulation to ensure its accuracy. It was noted that improvements could be made to the simulated thicknesses and compositions of the paint used to cover the lead blocks in the HALO Monte Carlo. The typical thickness and density of a dry layer of paint was measured and implemented in the simulation. The composition of the paint was inferred from common dyes found in paints and from previous ICPMS data. This new composition was implemented in the simulation. The change in paint composition slightly increased the efficiency of the detector, likely due it its lower ability to thermalize neutrons. This allows

the thermalization process to be focused closer to the neutron detectors, preventing other materials from capturing the neutrons.

Minor changes were made to the simulation to improve the accuracy of the geometry. Theses changes were checked for neutron detection efficiency changes caused by the updates in the geometries. With the exception of the removal of the graphite reflector, the changes were small and consistent with the expected effects of the modifications made.

HALO has a background neutron detection rate of 1298 ± 8 neutrons per day, most of which come from ambient Poisson sources. Bursts of neutrons from spallations and SF in the detector occur only a few times per day.

The HALO detector is well suited to run with a supernova trigger threshold of 4 neutrons in 2 seconds. With a time filter to remove neutron bursts from spontaneous fission and muon spallations and checks on the distribution of deposited energies to remove non-neutron bursts, the rate of false positives has been confined to 4.3 alarms per year. This rate is acceptable for SNEWS. The 4-neutron threshold gives the detector a characteristic range for supernova detection of 13.7 kpc, covering most of the Milky Way.

Appendix A

Multiplicity Fit Macro

```
#include "TFile.h"
#include "TTree.h"
#include "TTimeStamp.h"
#include <iostream>
#include <string>
#include <stdexcept>
using namespace std;

//structure to return info to aggregating macro
struct multfit {
  //TF1* thefit;
  //int extrain;
  Double_t when;
  int n;
  Double_t lr;
  //TF1* thefit;
  Double_t E;
  Double_t dE;
  Double_t norm; //norm //shortP
  Double_t dnorm; //dnorm //shortT
  Double_t RelE;
  Double_t dRelE;
  Double_t chisq;
  Double_t ndf;
  Double_t fitp; //p
};

//mult: reads a data file, identifies neutrons and groups them into
    coincident bursts of neutrons, and returns an efficiency and
    fission rate along with fit stats based on the multiplicity of the
    halo Cf source.
//runNum = number assigned to the desired run by ORCA (run file name
    is Run<runNum>.root)
//runsec = duration of run in seconds
multfit mult(int runNum, Double_t runsec)
{
```

```
//constants to be tuned to the detector performance
//mod
Double_t bgrate = 0.0329; //neutron rate for a run with no source in
    the detector or nearby, in Hz. Uses channels 280-1300. Open
    0.1025, closed 0.0329
Double_t wtime = 0.002; //window for coincicence in seconds. window
    time in fit should be the same.
Double_t dtime = 0.000073; //dead time for channel in seconds

Double_t nowtime = 0; //time the run started, to be assigned from
    data
Double_t normtime = 1457542800; //march 9 2016 1700 UTC
Double_t cfhl = 2.645*365*86400; // halflife of cf252 in seconds

//make runnumber string
string runNumber;
stringstream convert;
convert << runNum;
runNumber = convert.str();

//output plots
TH1F* multH = new TH1F("mults","Neutron Multiplicity",51,-1,50);
    //plot of multiplicity distribution form data
TH1F* delayH = new TH1F("delay","Delay From First
    Neutron",1000,0,10); //plot of delay time for neutron capture in
    each fission

//Parameters for finding E'/E = 1-LrLt
Double_t chanP[180]; //Likelyhood of neutron landing in channel this
    run. There are extra array spots; this is filled with
    chanP[channel + 10*card]=P and there are 8 cards per channel
for(int i = 0; i<180; i++)
{
  chanP[i]=0;
}
int chanfirsts =0;
int latefast = 0;
int lateall = 0;
int quicksamecycle=0;
int quicksamecard=0;
Double_t Lr = 0;
Double_t Lrerr =0;
Double_t Lt = 0;
Double_t ferr =0;

int numN = 0; //number of neutrons detected

//find the run file
gROOT->ProcessLine("gErrorIgnoreLevel=kError"); //Not necessary, but
    it gets rid of the "No dictionary for class XXXX found" warnings.
string InputLocation("Run");
InputLocation += runNumber;
InputLocation += ".root";
```

```
TFile InFile(InputLocation.c_str(), "READ");
InFile.Print();
TTree *treepoint;
treepoint = (TTree*)InFile.Get("ORTree");
treepoint->Print();
int nentries = treepoint->GetEntries();
cout<<"Entries: "<<nentries<<endl;
TTimeStamp *TimeStamp = new TTimeStamp;

//parameters for reading mutliuplicity data out of the data file
Double_t etime; //time of the current neutron count
Double_t ltime = 0; //time of the previous neutron count in a burst
Double_t ftime = 0; //time of the first neutron count in a burst
Double_t starttime = 0; //time at the start of the run
Double_t endtime = 0; //time at the end of the run
int mult = 0;//current neutronm multiplicity

//setup to read the data file
int fcard = 0; //card of the previous neutron count in a burst
int adc; //analog-digital-converter value (proportional to energy)
   of the current count
int card; //shaper card of the current count
int chan; //channel of the current count
TBranch* tbranch = 0;
TBranch* abranch = 0;
TBranch* cbranch = 0;
TBranch* chbranch = 0;
treepoint->SetBranchAddress("TimeStamp", &TimeStamp, &tbranch);
treepoint->SetBranchAddress("card", &card, &cbranch);
treepoint->SetBranchAddress("channel", &chan, &chbranch);
treepoint->SetBranchAddress("adc", &adc, &abranch);

//*************************************************************
// loop over all the counts in the data file
//*************************************************************
for (int i=0; i<nentries; i++)
{
  treepoint->GetEntry(i); //no effect
  tbranch->GetEntry(i);
  abranch->GetEntry(i);
  cbranch->GetEntry(i);
  chbranch->GetEntry(i);
  etime = TimeStamp->GetSec() + 0.000000001*TimeStamp->GetNanoSec();

  //assign run start and end times (clean up unused time)
  if(i==1) {nowtime = etime;}
  if(i==1)
  {
    cout.precision(30);
    cout<<"timeis "<<etime<<endl;
    cout.precision(6);
    starttime=etime;
  }
```

```
if(i==(nentries-1))
{
  cout.precision(30);
  cout<<"timeis "<<etime<<endl;
  cout.precision(6);
  endtime = etime;
}

if((adc>280 && adc<1300) && chan>(-1) && card<16) //filter for
    neutron ROI and remove test stand (cards 16 adn 17).
{
  numN++;
  //burst condition
  if(etime-ltime < wtime)
  {
    mult++;
    if(1-(abs(fcard - card) % 2))
       delayH->Fill((etime-ftime)*1000); //only fill time plot if
       events come from the same crate so crate NTP does not
       convolute data
    if(mult==2) //record numbers for the calculation of the nuber
       of neutrons that were missed due to dead time
    {
      if((1-(abs(fcard - card) % 2)) )
      {
        lateall++;
        if(fcard == card && etime-ftime<dtime)
        {
          quicksamecard++;
          if(etime-ftime<0.000007) quicksamecycle++;
        }
        if(etime-ltime < dtime)
        {
          latefast++;
        }
      }
    }
  }
  else // new count is not in burst, so the current burst is
      complete and can be written to the plots
  {
    multH->Fill(mult);
    mult = 1;
    ftime = etime;
    fcard = card;
    //fill chamP
    chanP[chan + 10*card] = chanP[chan + 10*card] + 1;
    chanfirsts++;
  }

  ltime = etime;
  fcard = card;
```

```
  }
}
//*************************************************************
// end of data loop
//*************************************************************


//Calculate Lr, the likelyhood of any two neutrons detected this run
   shareing the same counter and its error Lrerr
Lrerr=0;
for(int i = 0; i<180; i++)
{
  Lrerr = Lrerr + pow(chanP[i],3)/pow(chanfirsts,4);
  //cout<<"i Lr is "<<Lr<<" +- "<<Lrerr<<" i is"<<i<<endl;
}
Lrerr = sqrt(Lrerr);
Lr = 0;
for(int i = 0; i<180; i++)
{
  chanP[i] = chanP[i]/(1.0*chanfirsts);
  Lr = Lr + chanP[i]*chanP[i];
}
cout<<"Lr is "<<Lr<<" +- "<<Lrerr<<endl;

//Calculate Lt, the likelihood of a secondary neutron arriving in
   less than the dead time of the first. ferr is the error of the
   function 1-LtLr = E'/E
if(latefast == 0) //prevents crash on small data files
{
  latefast = 1;
  lateall++;
}
Lt = latefast/(latefast+(1-Lr)*(lateall-latefast));
ferr = pow(Lt/(latefast),
   2.0)*sqrt(Lr*Lr*(1-Lr)*(1-Lr)*latefast*lateall*(lateall -
   latefast)+pow(latefast*lateall*Lrerr, 2.0));
cout<<"Lt is "<<Lt<<endl;
cout<<"E'/E is "<<(1-Lr*Lt)<<" +- "<<ferr<<endl;

// place E'/E in an unused bit to include it in the fit
multH->SetBinContent(1, 1-Lr*Lt);
multH->SetBinError(1, ferr);

multH->SetBinContent(2, 0);
multH->SetBinError(2, 0);

InFile.Close();

//multiplicity fit call
TCanvas* Can1 = new TCanvas("multcan","Mult Fit",800,500);
TF1 *f1 = new TF1("CaliT",mCalTime,-1,20,5);
f1->SetParameter(0,14500); //number of fissions
f1->SetParameter(1,0.4);
```

```
f1->FixParameter(2,runsec); //time, fixed by data file
f1->SetParameter(3,1-Lr*Lt);
f1->FixParameter(4,wtime);
f1->SetParNames("norm","e", "time", "E'/E", "window");
gStyle->SetOptFit(1111);
TFitResultPtr fitres = multH->Fit("CaliT", "S", "", -1, 17); //fit
   all bins that have data
multH->GetXaxis()->SetTitle("Neutron multiplicity");
multH->GetYaxis()->SetTitle("Counts");
Can1->SetLogy();
multH->Draw();

//draw the ledgend of multiplicity fit
TLegend *leg = new TLegend(0.65,0.15,0.98,0.4);
leg->AddEntry(multH,"Multiplicity data","l");
leg->AddEntry(f1,"Sumed fit function","l");
leg->Draw();

//draw capture time plot
TCanvas* Can2 = new TCanvas("delaycan","Delay",800,500);
delayH->GetXaxis()->SetTitle("Time to a neutron from the start of
   the burst (ms)");
delayH->GetYaxis()->SetTitle("Counts");
delayH->Draw();

//fit capture times. This is not an accurate fit function but the
   best fit decay constant is usefull
TF1* f2 = new TF1("atten","[0]*exp(-x/[1]) + [2]",200, 1500);
f2->SetParameter(0,100);
f2->SetParameter(1,0.15);
f2->SetParameter(2,2);
f2->SetParNames("height","T", "pileup floor");
delayH->Fit("atten","L","",0.2,1.5);
Double_t Tdecay = f2->GetParameter(1);

//calculate the excess counts at short times compared to the
   exponential fit
int biin = 8;
Double_t Ltcontrol = f2->Integral(0,biin);
Double_t natshort = f2->GetParameter(2)*biin +
   100*Tdecay*f2->GetParameter(0)*(1-exp(-biin/(100*Tdecay)));
Double_t Pshort = (delayH->Integral(0,biin) -
   natshort)/(1.0*delayH->Integral(0,300));
Double_t Tshort = 6.0/(log(1+(quicksamecycle/(quicksamecard*1.0))));
cout<<"short time is "<<Tshort<<"us"<<", Long time is
   "<<Tdecay*1000<<"us"<<endl;
cout<<"shortp is "<<Pshort<<endl<<endl;

//display some parameters about the fit results
Double_t timepar = f1->GetParameter(2);
Double_t fitneutrons = 0;
Double_t fitfissions = 0;
```

```
  Double_t probsee = 0; //probability of detecting a neutron divided
     by caputre efficiency, E'<probsee*E<E
  Double_t pblock = 1-(f1->GetParameter(3)); //1-E'
  for(int i=0; i<49; i++)
  {
    fitneutrons = fitneutrons + i*f1(i+0.5);
    fitfissions = fitfissions + f1(i+0.5);
    if(i>0)
    {
      probsee = probsee +
          (1.0*i)*f1(i+0.5)*(1.0-(((i-1)/(1.0*i))*pblock));
    }
  }
  probsee = probsee/(1.0*fitneutrons);
  Double_t normfit=f1->GetParameter(0);
  Double_t frac250= 0.2858;
  Double_t avmult = 3.75718*(1-frac250) +3.53*frac250;
  Double_t nrate =
      (numN-bgrate*runsec)/(timepar*(f1->GetParameter(1))*probsee);
  //cout<<"nrate "<<nrate<<" probsee "<<probsee<<endl;
  Double_t dnrate =
      (sqrt(numN+bgrate*runsec))/(timepar*(f1->GetParameter(1))*
  probsee);
  Double_t Norm = normfit/(f1->GetParameter(2));
  Double_t dNorm = (f1->GetParError(0)) /(f1->GetParameter(2));
  Double_t nNorm = nrate/avmult;
  Double_t dnNorm = dnrate/avmult;

  //load tuple with parameters
  multfit tfit;
  Double_t corr = fitres->Correlation(0,1);
  tfit.when = nowtime;
  tfit.n = numN;
  tfit.lr = Lr;
  tfit.E=f1->GetParameter(1);
  tfit.dE = f1->GetParError(1);
  tfit.norm = f1->GetParameter(0);
  tfit.dnorm = f1->GetParError(0);
  tfit.RelE = f1->GetParameter(3);
  tfit.dRelE = f1->GetParError(3);
  tfit.chisq = f1->GetChisquare();
  tfit.ndf = f1->GetNDF();
  tfit.fitp = f1->GetProb();

  cout<<"fit fission rate "<<Norm<<"+-"<<dNorm<<" Hz"<<endl;
  cout<<"count fission rate "<<nNorm<<"+-"<<dnNorm<<" Hz"<<endl;
  cout<<"duration "<<endtime - starttime<<"s,"<<timepar<<"s was
     given"<<endl;
  cout<<"correlation "<<corr<<endl;
  return tfit;
}
```

```
//*************************************************************
//Cf multiplicity fit
//requires tuning to source age and fit function:
//-windowtime muse be the same as the time window used when building
   multiplicity distibution
//-frac250 must be set to the fraction of the fissions comeing from
   Cf250*.
//*Cf250 distibtution here is just Cf252 scaled by average
   multiplicity.
//*Also for an even older source a Cm248 distribution and fraction
   should be included
//Used the space between n and n+1 as the bin of multiplicity n. Also
   uses the -1 bin to fit for E'/E
//*************************************************************
Double_t mCalTime(Double_t* x, Double_t* par)
{
  //wintdow time
  Double_t windowtime = par[4]; //coincidence window in seconds, used
     to model pileup
  Double_t p248[9];//neutron multiplicity distribution for Cm248
     fission
  Double_t p250[9]; //neutron multiplicity distribution for Cf250
     fission
  Double_t p[9]; //neutron multiplicity distribution for Cf252
     fission, and later all fissions.

  p[0]=0.00212; //probability of a fission emmiting 0 neutrons
  p[1]=0.02598;
  p[2]=0.1267;
  p[3]=0.2734;
  p[4]=0.3039;
  p[5]=0.1848;
  p[6]=0.0657;
  p[7]=0.0154;
  p[8]=0.002;

  p250[0]=0.00369;
  p250[1]=0.03973;
  p250[2]=0.16097;
  p250[3]=0.2973;
  p250[4]=0.2863;
  p250[5]=0.1528;
  p250[6]=0.0484;
  p250[7]=0.0098;
  p250[8]=0.0010;
```

```
p248[0]=0.00660;
p248[1]=0.06515;
p248[2]=0.22433;
p248[3]=0.3415;
p248[4]=0.2559;
p248[5]=0.0923;
p248[6]=0.0130;
p248[7]=0.0012;
p248[8]=0.0000;

//fission ratioes. Numbers used are neutron ratioes but correction
   is still within errors.
Double_t frac250= 0.2732; //tests at 0.2858 //(fissions of
   Cf250)/(all fissions)
Double_t frac248= 0.0416; //(fissions of Cf248)/(all fissions)


//combiine into any-fision multiplicity distribution
for(int multnum=0; multnum<9; multnum++)
{
  p[multnum]=(1-frac250-frac248)*p[multnum]+frac250*p250[multnum]+
  frac248*p248[multnum];
}


//change the multiplicity distribution for n2n reactions
//these are very energy dependent, which might have a multiplicity
   correlation, making this wrong
//n2n correction was found to be unnecessary, so it was ommitted.
//currently does nothing
Double_t n2n=0.000; //would be about 0.001
for(int i =1; i<9; i++)
{
  p[i]=p[i]+(i-1)*n2n*p[i-1];
  p[i-1]=p[i-1]-(i-1)*n2n*p[i-1];
}


//define multiplicity distribution of two fissions piled togeter
Double_t pp[17]; //multiplicity of 2 fission
Double_t check =0;
for (int i=0; i<17; i++)
{
  pp[i]=0;
  for (int j=0; j<9; j++)
  {
    if(i>=j && (i-j)<9)
    {
      pp[i]=pp[i]+p[i-j]*p[j];
    }
  }
  check = check + pp[i]*i;
}
```

```
//cout<<"pp "<<check<<endl;

//define multiplicity distribution of three fissions piled togeter
Double_t ppp[25]; //multiplicity of 3 fissions
check =0;
for (int i=0; i<25; i++)
{
  ppp[i]=0;
  for (int j=0; j<9; j++)
  {
    if(i>=j && (i-j)<17)
    {
      ppp[i]=ppp[i]+(pp[i-j]*p[j]);
    }
  }
  //check = check + ppp[i];
}
//cout<<"ppp "<<check<<endl;


Double_t X =x[0]; //multiplicity
Double_t f=0; //expected number of detections of the specified
   multiplicity
Double_t partp; //probability of a fission giving the specified
   multiplicity
Double_t part1; //just gets fed into partp
Double_t part2; //just gets fed into partp
if(X<0 && X>-1)
{
  f=par[3]; //fit the E'/E bin
}
//detect k neutrons, out of l created in the fission, with the first
   h neutrons not detected
// par0 is the number of fission in the run
// par1 is the neutron detection efficencty
// par2 is the duration of the run
// par3 is E'/E
for (int k=0; k<17; k++)
{
  partp = 0;
  if((X<k+1) && X>k)
  {
    //All single fissions that give k neutron detections
    for (int l = k; l<9; l++)
    {
      if(k==0) //no detection so no full channel
      {
        //binomial with l neutrons detecting k neutrons with
           efficiency E
        part1 = TMath::Factorial(l)/(TMath::Factorial(k)*
        TMath::Factorial(l-k)); //l choose k
        part1 = part1*TMath::Power(par[1],k);
        part1 = part1*TMath::Power((1-par[1]),l-k);
```

```
      part1 = part1*p[l];
      //1-2*p(pile) +p(pile)^2
      part1 = part1*(2*exp(-par[0]*windowtime/par[2])-1+
      (TMath::Power((1-exp(-par[0]*windowtime/par[2])),2)));
      partp = partp + part1;
    }
    else
    {
      for(int h=0; h<(l-k+1); h++)
      {
        //binomial with l-h-i neutrons detecting k-1 neutrons
           with efficiency E' as well as one neutron detected
           after h undetected at efficiency E
        part1 = TMath::Factorial(l-h-1)/(TMath::Factorial(k-1)*
        TMath::Factorial(l-h-k));
        part1 = part1*TMath::Power(par[1]*par[3],k-1)*par[1];
        part1 = part1*TMath::Power((1-par[1]),h)*TMath::Power((1-
        par[1]*par[3]),l-h-k);
        part1 = part1*p[l];
        //1-2*p(pile) +p(pile)^2
        part1 = part1*(2*exp(-par[0]*windowtime/par[2])-1+
        (TMath::Power((1-exp(-par[0]*windowtime/par[2])),2)));
        partp = partp + part1;
      }
    }
  }
  //All double fissions that give k neutron detections
  for (int l = k; l<17; l++)
  {
    if(k==0)
    {
      part2 = TMath::Factorial(l)/(TMath::Factorial(k)*
      TMath::Factorial(l-k));
      part2 = part2*TMath::Power(par[1],k);
      part2 = part2*TMath::Power((1-par[1]),l-k);
      part2 = part2*pp[l];
      //p(pile) -2p(pile)^2
      part2 = part2*(1-exp(-par[0]*windowtime/par[2])-2*(
      TMath::Power((1-exp(-par[0]*windowtime/par[2])),2)));
      partp = partp + part2;
    }
    else
    {
      for(int h=0; h<(l-k+1); h++)
      {
        part2 = TMath::Factorial(l-h-1)/(TMath::Factorial(k-1)*
        TMath::Factorial(l-h-k));
        part2 = part2*TMath::Power(par[1]*par[3],k-1)*par[1];
        part2 =
           part2*TMath::Power((1-par[1]),h)*TMath::Power((1-par[1]
        *par[3]),l-h-k);
        part2 = part2*pp[l];
        //p(pile) -2p(pile)^2
```

```
            part2 = part2*(1-exp(-par[0]*windowtime/par[2])-2*
            (TMath::Power((1-exp(-par[0]*windowtime/par[2])),2)));
            partp = partp + part2;
          }
        }
      }
      //All triple fissions that give k neutron detections
      for (int l = k; l<25; l++) //Add up couts from tripple fissions
      {
        if(k==0) //no detection so no full channel
        {
          part1 = TMath::Factorial(l)/(TMath::Factorial(k)*
          TMath::Factorial(l-k));
          part1 = part1*TMath::Power(par[1],k);
          part1 = part1*TMath::Power((1-par[1]),l-k);
          part1 = part1*ppp[l];
          //p(pile)^2
          part1 =
             part1*TMath::Power((1-exp(-par[0]*windowtime/par[2]))
          ,2);
          partp = partp + part1;
        }
        else
        {
          for(int h=0; h<(l-k+1); h++) //cbdo +1
          {
            part1 = TMath::Factorial(l-h-1)/(TMath::Factorial(k-1)*
            TMath::Factorial(l-h-k));
            part1 = part1*TMath::Power(par[1]*par[3],k-1)*par[1];
            part1 = part1*TMath::Power((1-par[1]),h)*TMath::Power((1-
            par[1]*par[3]),l-h-k);
            part1 = part1*ppp[l];
            //p(pile)^2
            part1 =
               part1*TMath::Power((1-exp(-par[0]*windowtime/par[2]))
            ,2);
            partp = partp + part1;
          }
        }
      }
      f = par[0]*partp;
    }
  }
  //add background counts to single neutron bin
  Double_t bgrate = 0.0329;
  Double_t bg = bgrate*par[2];
  if(1<X && X<2)
  {
    f=f+bg;
  }
  return f;
}
```

Bibliography

[1] A. Burrows, "Supernova explosions in the universe", Nature **403**, 727 (2000).

[2] N. Rubido and S. Bruzzone, The Chandrasekhar limit for white dwarfs, http://www.fisica.edu.uy/~sbruzzone/FlexPaper_1.4.2_flash/prueba.pdf.

[3] S. Chandrasekhar, "The highly collapsed configurations of a stellar mass", Monthly Notices of the Royal Astronomical Society **93**, 456 (1931).

[4] H.-Th. Janka, K. Langankeb, A. Marek, G. Martínez-Pinedo, B. Müller, "Theory of core-collapse supernovae", Physics Reports **442**, 38 (2007).

[5] J. Engel, G. C. McLaughli, C. Volpe, "What can be learned with a lead-based supernova-neutrino detector?", Journal of Cosmology and Astroparticle Physics, **67, 013005**, 5 (2003).

[6] W. David Arnett, John N. Bahcall, Robert P. Kirshner, and Stanford E. Woosley, "Supernova 1987a", Annual Review of Astronomy and Astrophysics **27**, 629–700 (1989).

[7] Kate Scholberg, Alec Habig, *What is snews?*, (2016) http://snews.bnl.gov/.

[8] M. Arnould, S. Goriely, and K. Takahashi, "The r-process of stellar nucleosynthesis: astrophysics and nuclear physics achievements and mysteries", Physics Reports **450**, 97–213 (2007).

[9] F. P. Technologies, *Particle center*, (2012) http://www.particlecentral.com/index.html.

[10] Mathias Th. Keil, Georg G. Raffelt, and Hans-Thomas Janka, "Monte Carlo study of supernova neutrino spectra formation", The Astrophysical Journal **590**, 971–991 (2003).

[11] Gianluigi Fogli, Eligio Lisi, Antonio Marrone, Alessandro Mirizzi, "Collective neutrino flavor transitions in supernovae and the role of trajectory averaging", Journal of Cosmology and Astroparticle Physics **2007** (2007).

[12] W. Janka H.-T. Hillebrandt, "Neutrino emission from Type II supernovae - an analysis of the spectra", Astronomy and Astrophysics **224**, 49–56 (1989).

[13] K. A. Olive et al., "Review of Particle Physics", Chin. Phys. **C38**, 090001 (2014).

[14] Collaboration of JUNO, *Juno*, (2015) http://www.staff.uni-mainz.de/wurmm/juno.html.

[15] Huaiyu Duan, George M. Fuller, J. Carlson, Yong-Zhong Qian, "Coherent development of neutrino flavor in the supernova environment", Phys.Rev.Lett. **97** (2006).

[16] B. Kayser, "Neutrino mass, mixing, and flavor change", Nuclear and Particle Physics **33**, 156 (2005).

[17] XU Jing, HUANG Ming-Yang, HU Li-Jun, GUO Xin-Heng, YOUNG Bing-Lin, "Detection of supernova neutrinos on the earth for large theta13", Commun. Theor. Phys **61** (2014).

[18] A. Friedland, "MSW effect for large mixing angles", Frontiers in Contemporary Physics **2001** (II).

[19]Gialuigi Fogli, Eligio Lisi, Antonio Marrone, Alessandro Mirizzi, arXiv.

[20]e. a. T Fischer, "Early protoneutron star deleptonization - consistent modeling of weak processes and equation of state", J. Phys.: Conf. Ser. **665**, 012069 (2016).

[21]I. Tamborra, "Supernova neutrinos: theory", arXiv, 1604.07332v1 [hep–ph] (2016).

[22]L. W.S. A. Tammann G. A., "The galactic supernova rate", The Astrophysical Journal Supplement Series **92**, 487–493 (1993).

[23]S. P. Christine Kraus, "Progress in particle and nuclear physics", The Astrophysical Journal Supplement Series **64**, 273–277 (2010).

[24]K. Zuber, "HALO, a supernova neutrino observatory", Nuclear and Particle Physics Proceedings **265-266**, 233–235 (2015).

[25]D. Kopeliovich et al., About ORCA, (2016) http://orca.physics.unc.edu/Orca_Help/About_Orca.html.

[26]T. Shantz, "Design and Construction of the Helium and Lead Observatory for Supernova Neutrinos", Laurentian University (2010).

[27]M. Bercovitch and W. F. Davidson, "Cosmic ray neutron monitoring in Canada", Physics in Canada **68 No. 1**, 16–18 (2012).

[28]M. Schumaker, "Lead block Monte Carlo implementation", HALO DocDB 325-v1 (2016).

[29]M. Schumaker, "Steel rings Monte Carlo implementation", HALO DocDB 323-v2 (2016).

[30]The SNO Collaboration, "The Sudbury Neutrino Observatory", Nuclear Instruments and Methods in Physics Research **A449**, 172–207 (2000).

[31]V. Zerkin, ENDF: Evaluated Nuclear Data File, (2016) https://www-nds.iaea.org/exfor/endf.htm.

[32]M. Schumaker, "HALO water box Monte Carlo implementation", HALO DocDB 300-v1 (2016).

[33]M. Schumaker, "Plastic lumber under-layer Monte Carlo implementation", HALO DocDB 309-v1 (2016).

[34]E. Vazquez-Jauregui, Neutron Backgrounds at SNOLAB, (2013) https://zzz.physics.umn.edu/lowrad/_media/130304_snolab.pdf.

[35]A. G.Audi and C.Thibault, Atomic mass adjustment, (2003) http://www.nndc.bnl.gov/masses/mass.mas03.

[36]D. Väänänen and C. Volpe, "The neutrino signal at HALO: learning about the primary supernova neutrino fluxes and neutrino properties", Journal of Cosmology and Astroparticle Physics, **2011**, 19 (2011).

[37]G. Folger, Geant4: A toolkit for the simulation of the passage of particles through matter, (2017) http://geant4.cern.ch/.

[38]M. Schumaker, "Monte Carlo geometry checklist", HALO DocDB 279-v12 (2016).

[39]D. Kopeliovich, Composition of paints [SubsTech], (2014) http://www.substech.com/dokuwiki/doku.php?id=composition_of_paints.

[40]H. Yoido, Phthalocyanine Green G C.I. Pigment Green 7, (2013) http://www.chemicalland21.com/specialtychem/finechem/PHTHALOCYANINE%20GREEN%20G.htm.

[41]S. Yen, "Expected neutron multiplicity and distribution in HALO from muon-induced spallation", HALO DocDB 227-v1 (2014).

[42]H. M. Boldeman J.W., "Prompt neutron emission probabilities following spontaneous and thermal neutron fission", Nucl. Sci. Eng. **91**, 114 (1985).

[43]C. Bruulsema, "Voltage calibration results", HALO DocDB 302-v1 (2016).

[44]C. Bruulsema, "HALO data acquisition timing", HALO DocDB 215-v1 (2013).

[45]N. J. Roberts and L. N. Jones, "The content of 250cf and 248cm in 252cf neutron sources and the effect on the neutron emission rate", Radiation Protection Dosimetry **126**, 83 (2007).

[46]J. P. B. Darleane C. Hoffman G. P. Ford and L. R. Veeser, "Neutron multiplicity measurements of Cf and Fm isotopes", Phys. Rev. C **21**, 637 (1980).

[47]R. Vogt and J. Randrup, "Neutron angular correlations in spontaneous and neutron-induced fission", Phys. Rev. C **90**, 064623 (2014).

[48]E. Kolbe1 and K. Langanke, "Role of ν-induced reactions on lead and iron in neutrino detectors", Phys. Rev. C **63**, 025802 (2001).

[49]S. M. G. Drexlin V. Hannen and C. Weinheimer, "Current direct neutrino mass experiments", Advances in High Energy Physics **2013**, 293986 (2013).

[50]N. E. Holden and M. S. Zucker, "A reevaluation of the average prompt neutron emission multiplicity (nubar) values from fission of uranium and transuranium nuclides", BNL-NCS-35513.

[51]Thomas E. Ward, Alexander A. Rimsky-Korsakov, Nikolai A. Kudryashev, Denis E. Beller, "Integral neutron multiplicity measurements from cosmic ray interactions in lead", American Institute of Physics **842**, 1103–1105 (2005).

[52]D.-M. Mei and A. Hime, "Muon-induced background study for underground laboratories", Phys. Rev. D **73**, 053004 (2006).

[53]C. Bruulsema, "Spallation discrimination", HALO DocDB 260-v1 (2015).

[54]C. Bruulsema, "Snews triage", HALO DocDB 280-v1 (2015).

[55]C. Bruulsema, "Supernova candidate analysis guide", HALO DocDB 281-v1 (2015).

[56]G. R. A. Mirizzi and P. Serpico, "Earth matter effects in supernova neutrinos: optimal detector locations", Journal of Cosmology and Astroparticle Physics **2006**, 8 (2006).